DOCTORAATSPROEFSCHRIFT

2012 | Faculteit Wetenschappen

Preparation and Characterization of Novel and Eco-Friendly Hybrid Organic: Inorganic Solar Cells

Proefschrift voorgelegd tot het behalen van de graad van
Doctor in de Wetenschappen, Fysica, te verdedigen door:

Venkata Visveswara Gopala Krishna THALLURI

Promotor: prof. dr. Jean Manca
Copromotor: prof. dr. Dirk Vanderzande

D/2012/2451/5

universiteit hasselt

PhD Jury

Date: 13th January 2012

Chairman	Prof. dr. Marc D'Olieslaeger	UHasselt & IMEC vzw, Belgium
Promoter	Prof. dr. Jean Manca	UHasselt & IMEC vzw, Belgium
Copromoter	Prof. dr. Dirk Vanderzande	UHasselt & IMEC vzw, Belgium
Jury members	dr. John Noel Clifford	Institute of Chemical Research of Catalonia (ICIQ), Spain
	dr. Abay Gadisa Dinku	The University of North Carolina (UNC), USA
	dr. Mikhail Parchine	K U Leuven, Belgium
	Prof. dr. Marlies Van Bael	UHasselt & IMEC vzw, Belgium
	dr. Hans Moons	UHasselt, Belgium

Table of Contents

Table of Contents

Acknowledgements

My doctoral degree has been carried out since Jan, 2008 in the research group of Organic Nanostructured Electronics and Energy conversion (ONE^2), Department of Physics, Institute for Material Research (IMO), University of Hasselt. I would like to gratefully acknowledge financial support from the Bijzonder Onderzoeks Fonds (BOF), Belgium. I would like to thank all people who supported me directly and indirectly during my doctoral studies at UHasselt in these four years.

First of all, I would like to express my deepest gratitude to my promoter Prof. dr. Jean Manca and co-promoter Prof. dr. Dirk Vanderzande for giving me the opportunity to pursue my PhD. Many fruitful discussions with them helped me to gain perpetual energy and motivation to complete my PhD in high spirit. Doing my PhD work in the ONE^2 group gave me the freedom to explore, express and realize my ideas. I also had the opportunity to study different kinds of solar cells within multi-disciplinary collaborations, namely with the Organic/Inorganic Chemistry Groups at UHasselt, IMEC (Leuven), U. Antwerp, XIOS and ICIQ-Spain.

I also would like to thank Prof. dr. Marlies Van Bael (IMO/UHasselt), dr. Laurence Lutsen (IMO/IMEC), dr. Mikhail Parchine (KU Leuven) and dr. Abay Gadisa (UNC) who attended my PhD meetings and gave me valuable feedback. This project would not have been possible without the help of dr. Abay Gadisa and dr. John Clifford Noel (ICIQ, Spain); discussions with them made me confident and helped me to achieve more interesting results. I would additionally like to thank dr. Hans Moons for taking the time to read and criticize my PhD manuscript.

Thanks to Donato, Fortunato and Jean-Christophe for doing the opto-electrical characterizations. I express my appreciation to dr. Jan D'Haen, Bart Ruttens and Tine Boonen for TEM, SEM and XRD characterization on my samples. I would also like to express my gratitude to Prof. dr. Thomas Cleij and dr. Ayse E. Boyukbayram for CV measurements. Thanks to Wouter Moons for introducing me to the screen printer and to the preparation of DSSCs at the initial stage of my work. I also thank Huguette Penxten for her help in the UV-Vis Absorption and PL measurements. I would also like to thank Bert Conings for introducing me to the spray coating technique which helped in my thesis.

Furthermore, I would like to thank Prof. dr. An Hardy, dr. Heidi Vanden Rul, Linny Baeten and Bertie Souvereyns for their help in providing me metal-oxide materials and grown layers. Thanks to dr. Wibren Oosterbaan, Veerle Vrindts, Iris Duyssens, Suleyman Kudret, Lidia Georgiana Marin, Sarah Van Mierloo, dr. Joke Vandenbergh and Jurgen Kesters. Special thanks to the IMEC-OPV group members Tom, Cheyns, Afshin and many more.

Johnny Baccus has been a great help throughout my work. His diligent work in arranging things for the experiments in the lab is highly appreciable. I am grateful to the professors group: Prof. dr. Hans-Gerd Boyen, Prof. dr. Patrick Wagner, Prof. dr. Ken Haenen, Prof. dr. Milos Nesladek, Prof. dr. Ward De Ceuninck. I also thank to Danny Polus. Heartful thanks to Christel and Hilde for their help in ordering the materials and sample preparations. Very kind thanks to the vice director of IMO Prof. dr. Marc D'Olieslaeger for the financial support in attending conferences at SFO-USA, E-MRS, BPS-Namur and many more. Thanks to Erik for his help while fixing the software related issues.

I would like to thank to all my Indian friends (Yaso, Sathya, Anitha and others), extended thanks to other ONE group members, Koen, Jeroen. S, Tim, Dierckx, Pieter, Jeroen. D, Mirco, dr. Sabine Berto, dr. Emilie Bourgeois and dr. Wim Deferme. I want to thank dr. Boumédiène BenMoussa for sparing his time during coffee breaks. Special thanks to Lea, Relinde, Lisette, Monique, Jan Mertens and Lieven De Winter. Additionally to all colleagues at UHasselt and fellow students, at IMO, it has been a profound learning experience by working together with engrossing researchers who are very strongly devoted to their research.

Finally I would like to thank Prof. dr. Emilio Palomares (ICIQ-Spain) for his collaboration during this work and I hope this will continue in future.

I convey my wholehearted thanks to my beloved and beautiful family. Without their support I would not have accomplished this milestone in my scientific journey. If my Father would be alive, he would be very happy to see me as a doctoral scholar.

Thanks to my believing almighties Achuthya Swami and Shiridi Sai Baba. With their blessings all the things went well throughout my research life at UHasselt.

Above all, I finally and most importantly, thank my wife Saipriya and my son Mihir. Your patience and dedication has been terrific, even though during your pregnancy time and also for more things than space allows, but

mostly for love and support. It is even my pleasure to express gratitude to Ganesh Koushik (bother-in-law) who helped in lot of things during stressful situations.

Thank you!

Dank je wel!

Merci beaucoup!

Gracias!

ధన్యవాదాలు!

शुक्रीया!

Gopala Krishna T.V.V

This work is dedicated to my father

List of Acronyms and Abbreviations

A	AM	Air mass
B	BHJ	Bulk heterojunction
	t_{β}	Bimolecular life-time
	β	Bimolecular recombination coefficient
	C_{60}	Buckminsterfullerene
C	C	Capacitance
	n	Charge carrier concentration
	CB	i) Conduction band; ii) Chlorobenzene
	CELIV	Charge extraction by linearly increasing voltage
	CuPc	Copper phthalocyanine
	CV	Cyclic voltammetry
D	DSSC	Dye-sensitized solar cell
E	EDX	Energy-dispersive X-ray
	EQE	External quantum efficiency
	η	Power conversion efficiency
F	FET	Field effect transistor
	FF	Fill factor
	FTIR	Fourier transform infrared spectroscopy
	FTPS	Fourier transform photocurrent spectroscopy
	FTO	Flourine doped tin oxide
H	HOMO	Highest occupied molecular orbital
	HSC	Hybrid solar cell
I	I	Iodide
	IR	Infrared
	IS	Impedance spectroscopy
	IV	Current voltage
	I_3	Triiodide
	I_{sc}	Short circuit current
	ITO	Indium-tin-oxide
J	J_{sc}	Short circuit current density

L	LUMO	Lowest unoccupied molecular orbital
	τ	Life time of the charge carrier
M	M_W	Molecular weight
	μ	Mobility of charge carriers
	MLCT	Metal-to-ligand charge transfer
N	NIR	Near infrared
	N_e	Number of photogenerated electrons
	N_p	Number of incident monochromatic photons
	nm	Nanometer
	N_2	Nitrogen
O	OD	Optical density
	O_2	Oxygen
P	P_{light}	Incident light power
	P_{max}	Maximum power
	P3HT	Poly(3-hexylthiophene)
	PCBM	(6,6)-phenyl C_{61}-butyric acid methyl ester
	PEDOT:PSS	poly(3,4-ethylenedioxythiophene):poly(styrene sulphonic acid)
	P3PmT	poly[3-(potassium-m-alkanoate)thiophene-2,5-diyl]
	PITN	poly(isothianaphthene)
R	ε_r	Relative dielectric permittivity
S	SAED	Selected area electron diffraction
	SCLC	Space charge limited current
	SEM	Scanning electron microscope
	ss-DSSC	Solid-state dye sensitized solar cell
T	TAS	Transient absorption spectrocopy
	TEM	Transmission electron microscopy
	TPC	Transient photocurrent
	TPV	Transient photovoltage
	TiO_2	Titanium dioxide
U	UV	Ultraviolet
	U_{max}	Maximum voltage
	U_{offset}	Built-in-field.
V	V_{oc}	Open circuit voltage
	v	Constant velocity

	V	Wave number
	V_{bi}	Built-in-voltage
	Vis	Visible
X	XRD	X-ray diffraction
Z	ZnO	Zinc oxide

Summary

Emerging alternative photovoltaic (PV) technologies like Grätzel and polymer based solar cells offer an alluring way for simple and low cost PV production. In the photovoltaics research and development area, the main goal is to fabricate a low cost photovoltaic device with a sufficient stability and high efficiency. The organic:inorganic hybrid solar cells (HSCs) containing inorganic nanoparticles such as TiO_2/ZnO and semiconducting polymers such as P3HT are still behind emerging alternative photovoltaics. In spite of that, hybrid solar cells have the potential to grow towards better performance. They offer several benefits compared to polymer based solar cells such as low-cost, thin and easy to produce. Furthermore TiO_2/ZnO, are abundant materials.

The goal of this dissertation was the preparation and characterization of hybrid polymer:metal oxide solar cells. An important aspect of this work was the realization of an efficient 3-dimensional interpenetration nano-network of polymers as hole conductors/photo-active layer and metal oxides as electron acceptors/conductors. Initially, in this research the mesoporous TiO_2 nanostructured oxide layer electrodes were prepared and sensitized with different dyes. Poly-3(hexylthiophene) (P3HT) was deposited above metal oxide electrodes as a photoactive and hole transporting material and a structured way of complete device fabrication was developed. IV-characterizations and various opto-electrical measurements were performed for better understanding the physical properties of these nanostructured devices.

As an alternative approach, copper phthalocyanine (CuPc) as a hole conductor/photo active layer was vacuum sublimated above TiO_2 electrodes with and without dye sensitization. In these types of structured devices the IV-characterizations along with charge transport and charge separation properties were investigated by using a variety of opto-electrical characterization techniques.

Towards the development and preparation of eco-friendly hybrid solar cells, the dye and P3HT were replaced by water soluble conjugated polymer. The water soluble polymer was used as a hole transporting and photo-active layer. The opto-electric and morphological properties were systematically studied for some of the water soluble conjugated polymers. The best-performing polymer was processed by an alternative new processing

method and introduced above different TiO_2 electrodes. Complete solar cells were built in this way and IV-characteristics were investigated.

Towards the end of this work, conclusions are summarized and as an outlook the poly(isothianaphthene) (PITN) oligomer precursor solution polymerization into the metal oxide layers was studied. This stands as a principle for future development of solar cells by using this novel photo-active and hole transporting material for the complete filling of mesoporous nano-oxide layers with polymers.

Nederlands Samenvatting

Opkomende alternatief fotovoltaïsche (PV) technologieën zoals Grätzel en polymeer gebaseerde zonnecellen bieden een aantrekkelijke manier voor eenvoudige en goedkope PV-productie. In de onderzoek en ontwikkeling van fotovoltaïsche zonne-energie is het belangrijkste doel een zonnecelprototype te fabriceren met een voldoende stabiliteit en een hoog rendement tegen een zo laag mogelijke kost. De organische:anorganische hybride zonnecellen (HSC's) met anorganische nanodeeltjes zoals TiO_2/ZnO en halfgeleidende polymeren zoals P3HT staan nog steeds achter qua ontwikkeling in de opkomst van alternatief zonne-energie. Ondanks het voornoemde hebben hybride zonnecellen het potentieel om te groeien naar een betere prestatie. Ze bieden een aantal voordelen ten opzichte van polymeer gebaseerde zonnecellen, zoals een lage kost en ze zijn dun en eenvoudig te produceren. Verder is het zo dat TiO_2/ZnO in overvloed aanwezige materialen zijn.

Het doel van dit proefschrift was de voorbereiding en karakterisering van hybride polymeer: metaal-oxide zonnecellen. Een belangrijk aspect van dit werk was de realisatie van het efficiënte 3-dimensionale bi-continu nano-netwerk van polymeer als gatengeleider/foto-actieve laag en metaaloxide als elektronengeleider/acceptor. In eerste instantie werden de mesoporeuze TiO_2 nano-gestructureerde oxidelagen/elektroden voorbereid en gesensibiliseerd met verschillende kleurstoffen. Poly-3(hexylthiophene) (P3HT) werd gecoat boven metaaloxide elektroden als een foto-actief materiaal en gatengeleider en een gestructureerde manier van volledige zonnecelfabricage werd ontwikkeld. IV-karakteriseringen en verschillende opto-elektrische metingen werden uitgevoerd voor een beter begrip van de fysische eigenschappen van deze nano-gestructureerde zonnecellen.

Als een alternatieve benadering werd koper-ftalocyanine (CuPc) als een gatengeleider/foto-actieve laag vacuüm gesublimeerd boven TiO_2 elektroden met en zonder kleurstofsensibilisering. In dit soort gestructureerde zonnecellen werden de IV-karakteriseringen samen met ladingstransport- en ladingsscheiding-eigenschappen onderzocht door middel van verschillende opto-elektrische karakteriseringstechnieken.

Tijdens de ontwikkeling en voorbereiding van de eco-vriendelijke hybride zonnecellen werden de kleurstof en P3HT vervangen door een water oplosbaar geconjugeerd polymeer. Het water oplosbare polymeer werd gebruikt als een gatengeleider en foto-actieve laag. De opto-elektrische en morfologische eigenschappen werden systematisch onderzocht voor een

aantal van de in water oplosbare geconjugeerde polymeren. De best presterende polymeer werd verwerkt door een nieuwe alternatieve verwerkingsmethode en geïntroduceerd boven verschillende TiO_2 elektroden. Complete zonnecellen werden gebouwd op deze manier en de IV-kenmerken werden onderzocht.

Tegen het einde van dit werk werden de conclusies samengevat en als een visie voor toekomstige ontwikkeling de poly(isothianaphthene) (PITN) oligomeer precursor-oplossing polymerisatie in het metaaloxide lagen wordt bestudeerd. Dit staat als een principe voor de toekomstige ontwikkeling van zonnecellen door het gebruik van deze nieuwe foto-actieve en gatengeleidende materialen voor de volledige vulling van mesoporeuze nano-oxide lagen met polymeren.

Chapter 1: Introduction

1.1 Need for solar energy

The quest for energy around the globe is growing in leaps and bounds. This scenario is catalyzed by the global population increase and per-capita energy imbalance. The energy production needs to meet the projected population growth which is shown in the **Figure 1.1**. While innovation and technology dramatically transformed other industrial sectors, the energy production over the last few decades still heavily relies on fossil fuels. Adverse effects of fossil fuels are threatening the future environment and the energy production. Recent predictions show that the decline in global oil production rate is expected to start within the coming 10-20 years [2, 3]. Scientific evidence also proves that the reduction of carbon dioxide (CO_2) gas, methane and other greenhouse gases is the best way to contribute to a sustainable environment. The need for a low carbon emission, the increasing fuel costs and global warming are challenging mankind to strive for a radical transformation towards energy production. There is a need to look forward for energy resources which neither run out nor have significant harmful effects on our environment.

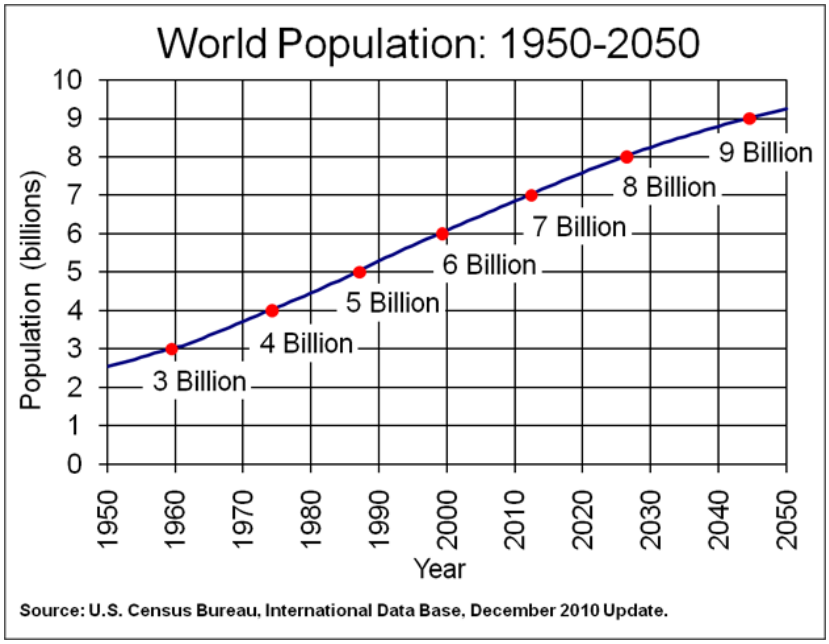

Figure 1.1: World population index from 1950 to 2050.[1]

Today, reducing greenhouse gas emissions alleviates the rampant global warming, a serious target for many countries. Multilateral agreements among many countries across the globe are being prepared to combat climate changes. These developments trigger an increase in renewable energy production. In other words, the necessity to curtail the share of traditional energy production should be replaced by superior green energy production techniques for balancing the forecasted energy demand. This will ensure energy security for future generations. An estimated rise in the global energy demand is depicted in the **Figure 1.2**.

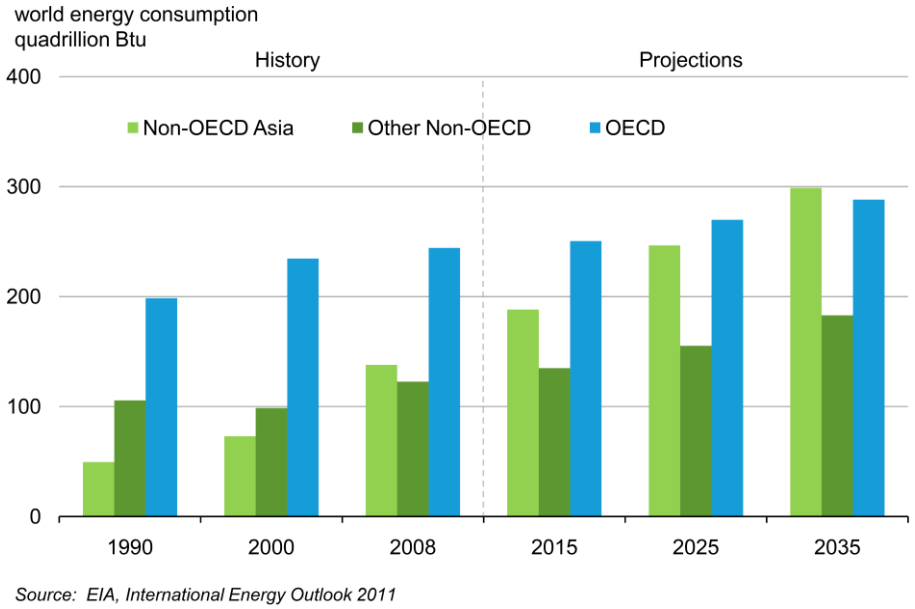

Figure 1.2: Global energy demand forecast (Economic Co-operation and Development – OECD and British thermal unit-Btu).[4]

Renewable-energy supplies 19 %[5] of the total global energy consumption and this includes alternative sources like traditional biomass, hydropower, wind, solar, geothermal and biofuels (see **Figure 1.3**). Not only the abundance of these renewable energies deserves great attention, but also the cost effectiveness compared to the fossil fuels needs much focus. This

cost disparity is reflected in the U.S electricity production[6] to some extent and is shown in **Figure 1.4**. Nearly 45 % of electricity is generated from coal, which is currently the lowest cost fuel but causes more pollution than other non-renewable sources. Therefore, any environmental friendly energy source must not only have the capacity to meet the growing global energy demands, but also has to meet the economic demands of the free market. Several renewable energies like wind energy, hydro thermal energy, etc. are already introduced into the market but are still in development.[7] The direct use of solar energy as a renewable energy source is believed to yield prominent results in the global energy supply. The sun is an inexhaustible source of energy and the earth receives in an average of 1395 J/m^2 from the sun.[8]

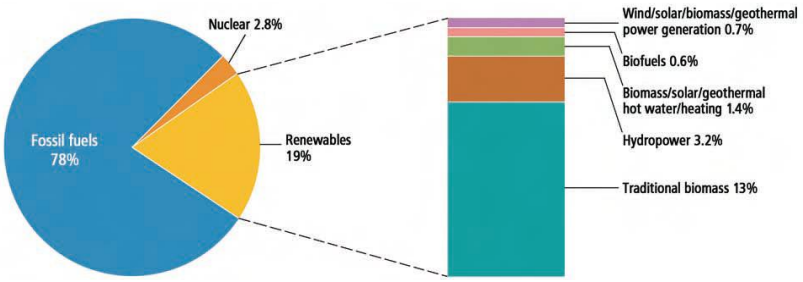

Figure 1.3: Renewable energy share of global energy consumption.[5]

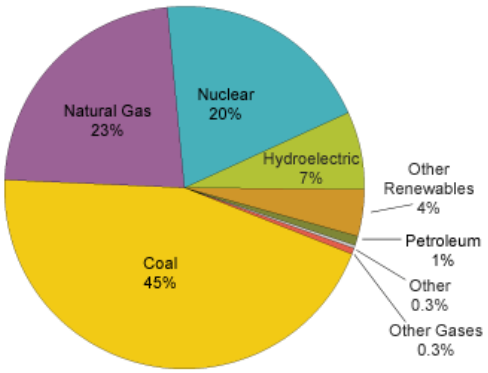

Figure 1.4: U.S electric power generation by fuel.[6]

Solar energy has a wide variety of applications. One of the prominent applications is the conversion of light into electricity as shown in **Figure 1.3** and is known as the 'photovoltaic effect', further explained in paragraph 1.2. Solar energy is the largest source for non-carbonaceous energy and can be used to produce electricity and fuel. The sun generates a wide electro-magnetic spectrum from gamma rays to radio waves. The major part is contributing between 300 nm - 800 nm with the highest absorption peak around 520 nm as shown in **Figure 1.5**. The solar spectrum reaching the earth surface mainly covers ultraviolet, visible and infrared regions, and the overall percentage contribution is depicted in **Figure 1.6**.

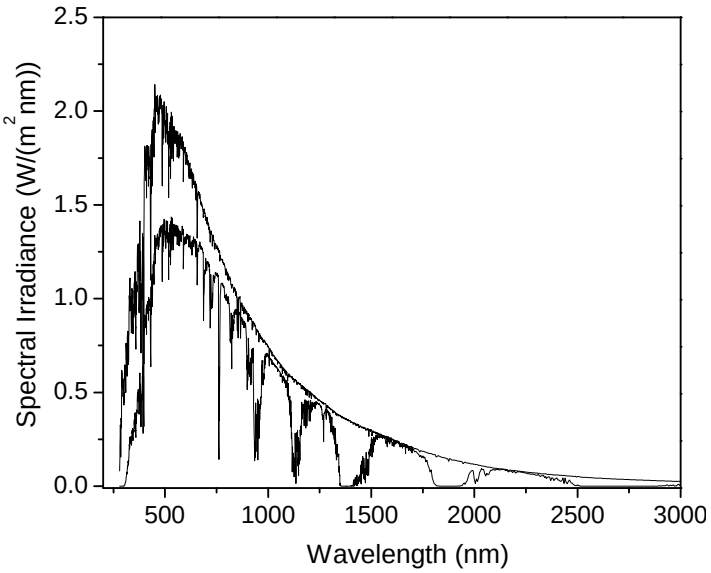

Figure 1.5: The solar spectrum of AM 1.0 (upper curve) and AM 1.5 (lower curve).

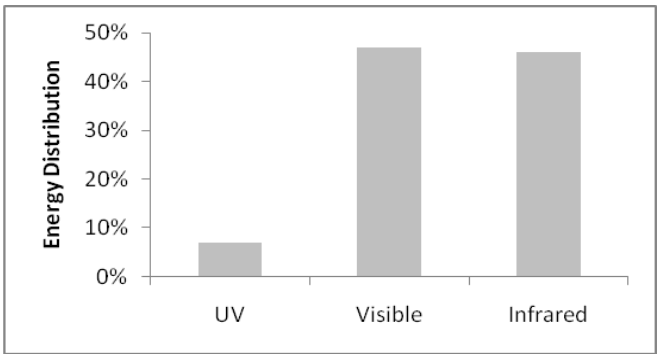

Figure 1.6: Energy distribution percentage in ultraviolet, visible and infrared wavelength regions.[8]

The attenuation of solar radiation is due to the scattering and absorption by air molecules, dust particles or aerosols in the atmosphere. The UV region is mainly absorbed by Ozone. Especially Water, Oxygen and CO_2 absorption contributes to the gaps in the spectral distribution of solar radiation as seen in **Figure 1.5** (lower curve). On a clear sunny day, nearly 70 % of the extraterrestrial vertical solar radiation reaches the earth surface.[9]

In solar cell research Air mass (AM)[10] is used often in simulations of the solar spectrum. This is a measure for the path of solar radiation that travels through the atmosphere. The solar radiation outside the atmosphere is called extraterrestrial or AM0 radiation. A terrestrial solar radiation standard has been defined as standard AM1.5 radiation. This serves as the standard spectral distribution. It corresponds to an angle of 48 degrees between the sun's position and the zenith of the earth. In **Figure 1.7** the AM 1.5 and its angle is shown.[9] The AM value is defined as equation 1.1:

$$\mathrm{AM(number)} = \frac{1}{\cos\theta} \qquad (1.1)$$

where Θ is the angle measured with reference to zenith line.

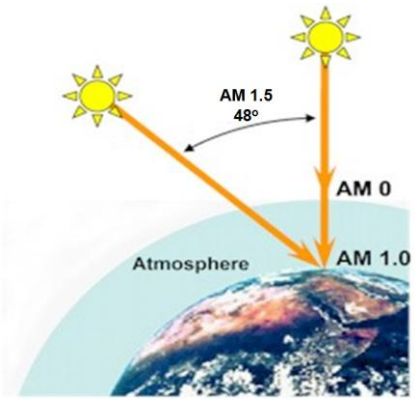

Figure 1.7: The path length of the solar radiation through the Earth's atmosphere in units of Air Mass (AM) increases with the angle from the zenith. The Standard spectrum AM 1.5 is 48° from the zenith.

1.2 Photovoltaic energy conversion

A photovoltaic device is able to convert light into electricity. 'Photovoltaic' is derived from the Greek word "Phos" referring to light, and the last name of Alessandro Volta, one of the pioneers in the study of electricity. In the photovoltaic effect, upon sunlight (composed of photons) absorption by the semiconductor material free charge carriers are created i.e. electrons and holes. The extraction and collection of these free charge carriers provide a voltage that needs to drive the current through an electrical circuit.

The efficiency of a PV device depends on the ability to convert the radiated light into electrical energy. This is explained as power conversion efficiency (η_e) which is derived from IV-characterization. η_e can be obtained from the experimentally attained IV-curve as shown in **Figure 1.8**

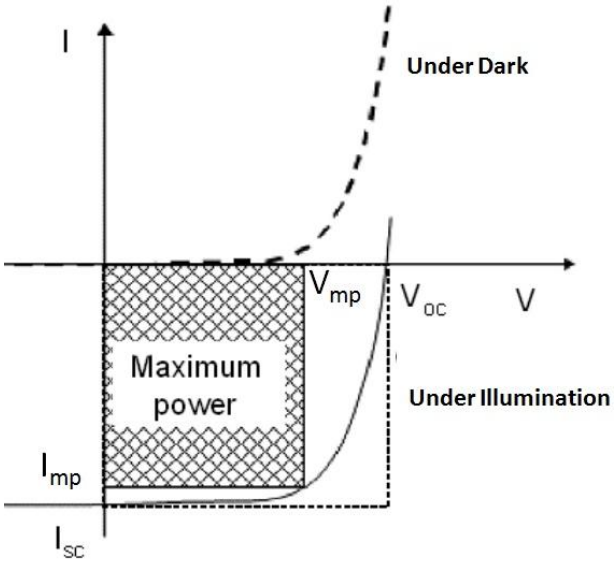

Figure 1.8: The IV-characteristic curves under dark and illuminated conditions.

In **Figure 1.8**, the maximum power (P_{mp}) is at the point (V_{mp} ,I_{mp}) and is given by equation 1.2, where V_{mp} is the maximum voltage, and I_{mp} is the maximum current.

$$P_{mp} = V_{mp} I_{mp} \quad (1.2)$$

This product also corresponds to the area of an inner rectangle shown in **Figure 1.8**. I_{SC} stands for short circuit current. This is the current flowing through the device when no external voltage is applied (V = 0 V). Since the short circuit current depends on the area of the photovoltaic device, it is better to use the short circuit current density (J_{SC}) which is defined as current/unit area.

V_{OC} stands for open circuit voltage. This is the external voltage (bias) that has to be applied for the device such that the external current flowing through the device is zero (I = 0 A).

The product of I_{SC} and V_{OC} gives a theoretical maximum for the total power that can be delivered by the device. To evaluate the photovoltaic cell performance the fill factor (FF) is introduced. It is defined as the ratio between the actual maximum power delivered and the theoretical maximum power of the cell.

$$FF = \frac{V_{mp} I_{mp}}{V_{oc} I_{sc}} \tag{1.3}$$

The energy conversion efficiency (η_e) is given as follows

$$\eta_e = \frac{P_{mp}}{P_{in}} = V_{mp} \frac{I_{mp}}{P_{in}} = \frac{V_{oc} I_{sc} FF}{P_{in}} \tag{1.4}$$

where P_{in} is power of the incident light source.

1.3 Types of solar cells

From the invention to the development of the first silicon solar cell in the 1950s[11], an enormous potential of photovoltaic systems for large-scale electricity production has been developed. Since silicon wafers are expensive, the focus is drawn towards the development of cheaper thin-film alternative solar cells. This paved the way towards the research and development for various new types of solar cells.[12] Most of them are still in the research phase: dye-sensitized solar cells, organic bulk heterojunction solar cells and hybrid organic:inorganic solar cells. These emerging types of solar cells are briefly discussed in the next sections. In this thesis work attention was drawn towards the development of organic:inorganic hybrid solar cells

1.3.1 Dye-sensitized solar cells

Dye sensitization (a thin film of dye molecules that are sensitive to light on to a TiO_2 layer) achieved a breakthrough in 1990's at the Laboratory of Photonics and Interfaces (EPFL-Lausanne) in Switzerland. Prof. Dr. M. Grätzel and his team developed solar cells by using a successful combination of nanostructured electrodes and efficient charge injection dyes which attained an efficiency of 7 % [13] in 1991 and increased up to 12.3 % [14] in 2011. These solar cells are well known as Dye Sensitized Solar Cells (DSSC) or Grätzel Solar Cells.

A DSSC is a photochemical cell which uses a liquid electrolyte as charge transfer medium. The structure and schematic explain the mechanisms involved in DSSC and are depicted in **Figure 1.9**.[15, 16]. Conventional DSSC mainly consists of six major components: (1) glass/Transparent Conductive Oxide (TCO) i.e. flourine doped tin oxide (FTO) electrode as Anode; (2) metal oxide hole blocking layer (dense layer); (3) mesoporous semiconductor metal oxide layer; (4) dye as a sensitizer; (5) liquid electrolyte (hole transporter) and (6) counter electrode. The TCO/dense TiO_2 layer is coated with mesoporous semiconductor metal oxide (TiO_2), on which the dye molecules are adsorbed. The special anchoring groups attached to the dye molecule can enhance this adsorption. A redox species like I^-/I_3^- is used as an electrolyte and also acts as a hole transporting layer.

The complete DSSC working principle can be well explained by three major processes involved: (a) light absorption; (b) charge separation and (c) charge transport and collection.

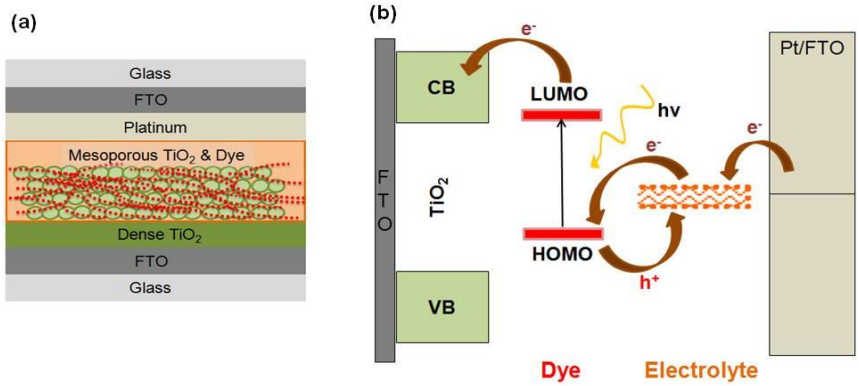

Figure 1.9: The structure **(a)** and schematic **(b)** illustrates the mechanism involved in DSSCs.

The incoming photon is absorbed by the dye molecule, which is adsorbed on the surface on the nanocrystalline TiO_2 particles layer. As a result, an electron from a molecular ground state S^0 of the dye is excited to a higher lying excited state S*. The excited electron is injected into the conduction band of the TiO_2 particles layer leaving the dye molecule to an oxidized state S^+. The injected electron percolates through the mesoporous nanocrystalline structure to the transparent conducting oxide layer on the glass substrate (negative electrode, anode) and finally through an external load to the counter-electrode (positive electrode, cathode). At the counter-electrode the electron is transferred to triiodide in the electrolyte to yield iodine, and the cycle is completed by the reduction of the oxidized dye by the iodine in the electrolyte. This operating cycle is summarized by a set of chemical reactions as described below.[17]

Anode:

Light absorption: $S^0 + hv \rightarrow S^*$

Electron injection: $S^* \rightarrow S^+ + e^- (TiO_2)$

Regeneration: $2\,S^+ + 3I^- \rightarrow 2S + I_3^-$

Cathode:

$I_3^-+2e^-$ (counter electrode) → $3I^-$

Regeneration:

e^- (counter electrode) + hv → e^- (TiO_2)

The maximum theoretical value for the open circuit voltage is determined by the potential difference between the conduction band edge of the TiO_2 and the redox potential of the I^-/I_3^- pair in the electrolyte.[18] The operation process of the DSSC is regenerative.

Different types of ruthenium complex dyes and organic dyes can be used in DSSCs. Some of them are listed and presented in the following:

1. cis-bis(isothiocyanato)bis(2,2′-bipyridyl-4,4′-dicarboxylato)ruthenium(II) (N3 Dye)

2. Di-tetrabutylammonium cis-bis(isothiocyanato)bis(2,2′-bipyridyl-4,4′-dicarboxylato)ruthenium(II) (N719 Dye)

3. cis-dithiocyanato-(2,2′-bipyridyl-4,4′-dicarboxylate) -[4,4′-bis(3-methoxystyryl)-2,2′ bipyridyl]-Ru(II) (Z-910)

4. Tris(isothiocyanato)-ruthenium(II)- 2,20:60,200-terpyridine-4,40,400-tricarboxylic acid, tris-tertrabutylammonium salt (Black Dye)

5. cis-Bis(isothiocanate)(4,40-bis(5-hexylthiophene-2-yl)-2,20-bipyridine)(4-carboxylic acid-40-carboxylate-2,20-bipyridine)ruthenium(II) sodium (C101 dye)

6. 2-cyano-3-(5-{2-[5-(1,1,6,6-tetramethyl-10-oxo-2,3,5,6-tetrahydro-1H,4H,10H-11-oxa-3a-aza-benzo[de]anthracen -9-yl)-thiophen-2-yl]-vinyl}-thiophen-2-yl)-acrylic acid (Couramin based NKX-2700 dye)

7. Dimethylflourenylamino moiety-JK 46 dye

8. Organic Triphenylamine based TA-St-CA dye

Above dye structures are shown in **Figure 1.10** and more dyes can be found in reference[19]. Their photovoltaic performances are referred in **Table 1.1**. The C101, N719 and black dyes were used in this thesis work.

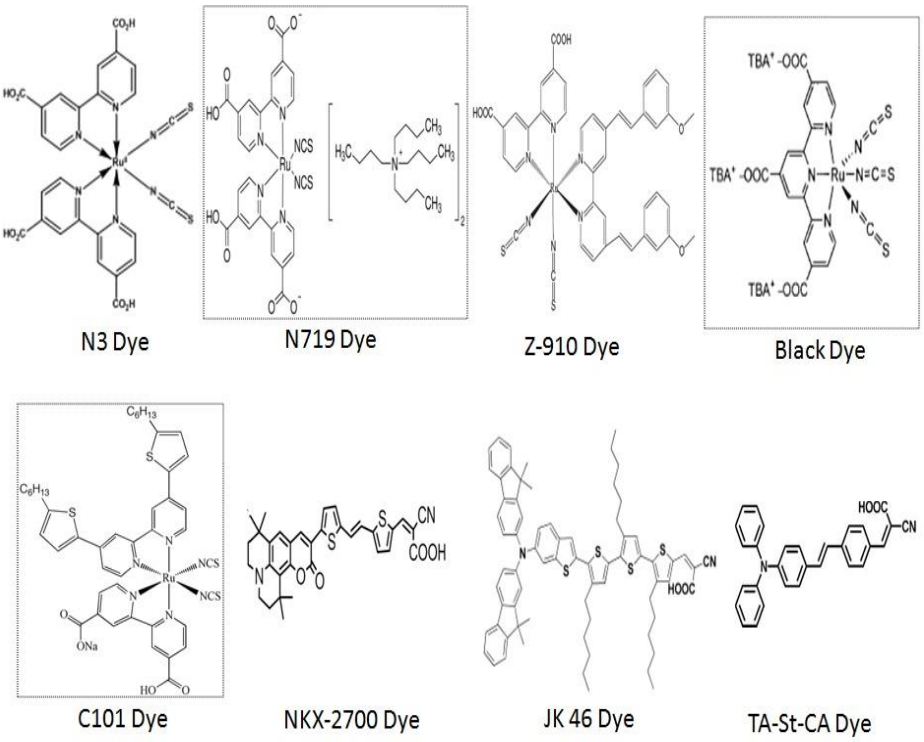

Figure 1.10: Different types of ruthenium based complex and organic dyes used in DSSCs. The dyes placed in rectangle are used in this thesis work. The C101 dye is experimentally synthesized novel dye; the N719 dye and Black dye can be supplied commercially.

Table 1.1: Photovoltaic performances of different dye based DSSCs.

Dye name	Band Gap (eV)	V_{oc} (V)	J_{sc} (mA/cm^2)	FF (%)	η (%)	Ref
N3	2.3	0.79	17.3	72	9.5	20
N719	2.3	0.76	17.5	68	9	20
Z-910	2.3	0.77	17.2	76.4	10.1	21
Black Dye	2.1	0.72	20.53	70.4	10.4	22
C101	2.2	0.77	17.94	78	11	23
NKX 2700	1.9	0.69	15.9	75	8.2	24
JK 46	2.2	0.66	17.5	74	8.6	25
TA-St-CA	2.4	0.74	18.1	67	9.1	26

These DSSCs obtained relatively good efficiencies. Although, the liquid electrolyte inhibits the commercialization due to problems of corrosion and leakage.[27] Therefore much effort is done to replace the liquid electrolyte by solid-state materials like organic hole transporters or p-type semiconductors. These cells are known as solid-state DSSCs (ss-DSSCs).[27] The ss-DSSCs can also be termed as organic:inorganic hybrid solar cells and their working principles will be explained in paragraph 1.3.2.2. In this thesis, novel organic:inorganic and eco-friendly hybrid solar cells were developed and characterized.

1.3.2 Polymer based solar cells

Semiconducting polymers are used in many organic electronic applications. The semiconducting polymers are conjugated materials and consisting of alternate single and double bonds. The doped conjugated organic polymer identified is iodine-doped polyacetylene $(\text{-CH=CH-})_n$[28]. This polymer consists of a long chain of carbon atoms with an alternating single and double bonds. However, only conjugation does not make a polymer conductive. It also requires doping, a process in which extra holes and electrons are added into the material. This can vary the conductive properties from insulators, semiconductors and conductors. An overview of range for the conductivity of

conjugated polymers is shown in **Figure 1.11**.[29] Increasing research efforts are put forward in the direction towards design of novel semiconductive polymers for electronic applications. One of the major application areas of semiconductive polymers is solar cells.

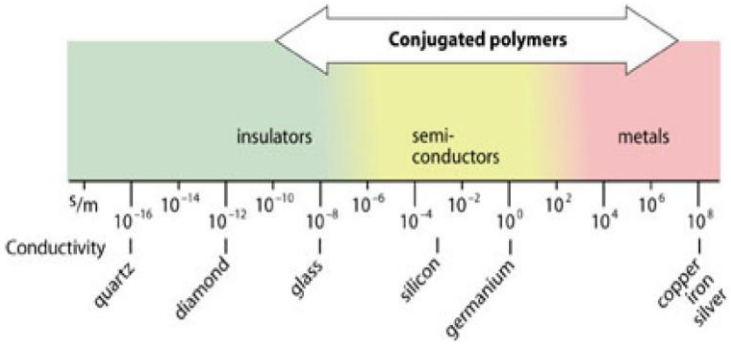

Figure 1.11: Conductivity of semiconductive polymers from quartz (insulator) to copper (conductor).[29]

Many efforts are made to introduce conjugated polymers in solar cells like polymer based bulk heterojunction solar cells (BHJs) and organic:inorganic hybrid solar cells. These kinds of solar cells will be explained in the succeeding paragraphs.

1.3.2.1 Bulk hetero junction organic solar cells

In BHJs, the excitons (bound pair of electrons and holes) are created upon light illumination. The diffusion length of excitons and the thickness of active layer need to be maintained for an efficient solar cell. [30, 31] The BHJ device structure is shown in **Figure 1.12**. The active layer is prepared from a blend of acceptor and donor materials. The combination of work horse donor material P3HT[32] with acceptor spherical fullerene[33] materials have reached to an efficiency of 6.5 %. Nevertheless, there is room to improve the device performance and the recent updates are presented in **Table 1.2**. One of the

important parameters that define the device performance is mobility of the charge carriers (Poly(3-hexylthiophene - P3HT hole mobility is 10^{-4} cm^2/Vs [34] and [6, 6]-Phenyl C61 butyric acid methyl ester - PCBM electron mobility is 10^{-3} cm^2/Vs [35]) with the morphology of the active layer. The morphology can affect the interaction between the donor and acceptor interface. The increased interface area in BHJ cells favors more efficient exciton dissociation. In BHJs, distributed pn-junctions are created between donor and acceptor materials throughout the active area. The complete process is clearly explained in following sections.

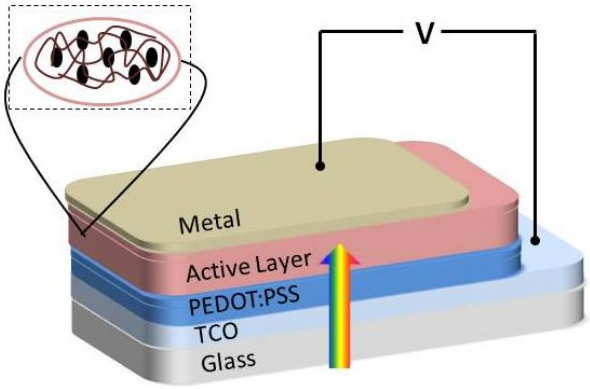

Figure 1.12: Device structure of bulk hetero junction organic solar cells. In inset active layer (donor:acceptor blend) morphology.

Different steps are involved in the photovoltaic process in BHJ. The graphical representation of working principle is shown in **Figure 1.13**.

a **Photon absorption and charge generation**: In organic solar cells, light is generally absorbed by the donor material and by the acceptor materials but in a smaller extent for the latter. Both these materials absorb at different wavelengths. As a result of this absorption, excitons are generated.

b **Exciton diffusion**: In the organic materials, created excitons binding energy is high. The diffusion length is around 5 nm - 10 nm.[36, 37] From the created exciton, the electron is transferred from the donor to the

acceptor material due to an energetic difference between their LUMO levels. Even though the electron is transferred to the acceptor material, it still experiences strong Coulomb force with the hole. At this stage, they are called a polaron pair. The applied electric field dissociates these polarons. Therefore, the photocurrent in organic solar cell strongly depends on the applied voltage. Now, the excitons are separated into free holes in the donor and free electrons in the acceptor.

c **Charge Transport and extraction**: The electrons and holes are transported to their respective electrodes by a hopping mechanism. The charge transport mechanism is field driven and mainly depends on the carrier mobility, the carrier life time, the electric field and on morphology of the donor-acceptor blend.[38] The carriers are collected at the contacts which should be ohmic for one of the charge carriers and blocking contact for the other. If the contact acts as a barrier for one of the charge carriers, the internal field decreases, which results in recombination and lowers the number of extracted charge carriers.

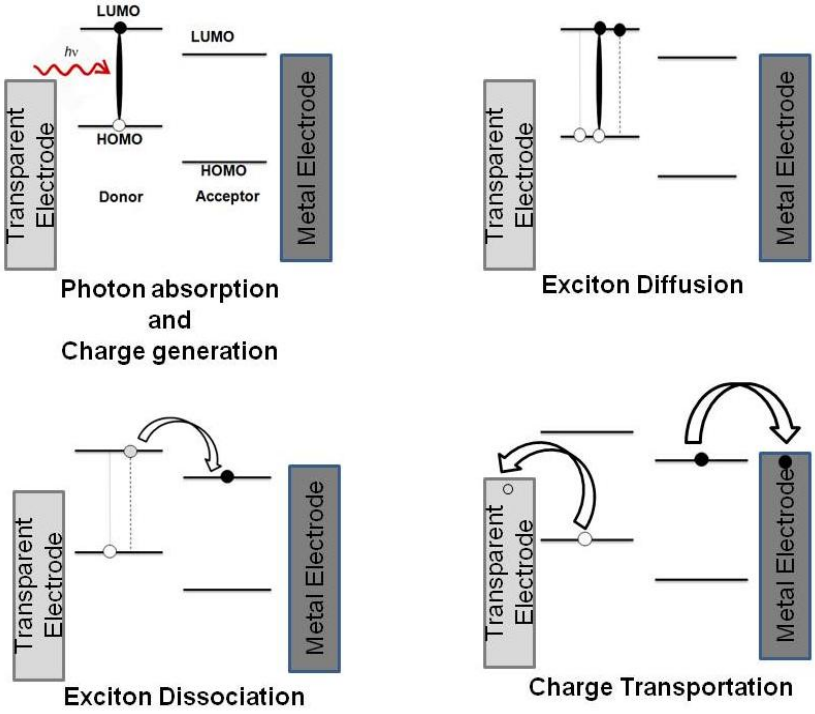

Figure 1.13: Working principle of bulk heterojunction solar cells.

Different types of donor materials and acceptor materials are shown in **Figure 1.14** and their device performances in BHJs are presented in **Table 1.2**.

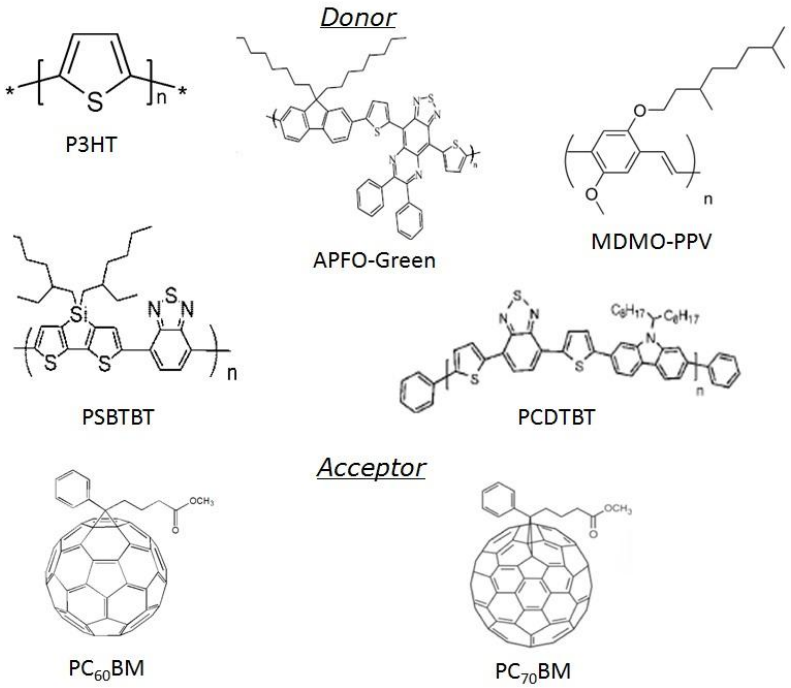

Figure 1.14: Examples of donor and acceptor materials for BHJs.

Table 1.2: Device performances of BHJs

Donor Material	Band gap (eV)	V_{oc} (V)	J_{sc} (mA/cm^2)	FF (%)	η (%)	Ref
P3HT	2.0	0.84	10.61	72.7	6.5	39
APFO Green	1.24	0.78	3	38	0.9	40
MDMO-PPV	2.3	0.82	5.25	61	2.5	41
PCDTBT	1.9	0.9	11.95	66.4	7.2	42
PSBTBT	1.45	0.68	12.7	55	4.7	43

1.3.2.2 Hybrid organic:inorganic solar cells

A hybrid solar cell is a combination of organic and inorganic materials and uses unique properties of both of them. Inorganic semiconductor nanoparticles e.g. have a high absorption co-efficient and the tunable band gap depending on the particle size. Solution based processing like spin coating, dip coating, spray coating, screen printing and roll-to-roll printing can be used.[44] Advanced techniques like vacuum evaporation can also be used. In this thesis work spin coating, dip coating, spray coating and vacuum evaporation techniques were used for building the hybrid solar cells.

Various approaches can be used to construct organic:inorganic hybrid solar cells. The main goal in the development of these solar cells is to obtain an optimal balance of charge carriers at the donor:acceptor interface area. Appropriate phase separation is also needed for effective transport of charges towards their respective electrodes. The three most commonly used types of hybrid organic:inorganic solar cells that have been reported so far are described below. The different steps of the charge separation and collection process involved in these organic:inorganic hybrid solar cells are similar to the BHJ solar cells (**Figure 1.13**).

Different types of organic:inorganic hybrid solar cells are.

1 Bilayered devices: They can be processed by depositing an organic layer above an inorganic semiconductor acceptor layer.

2 Blended devices: The processing of blended devices is similar to the polymer:fullerene bulk heterojunction solar cells i.e. mixing of organic: inorganic (nanoparticles).

3 Structured devices: Deposition of organic semiconducting polymers for filling the mesoporous/nanostructured inorganic layer also results in hybrid solar cells.

1.3.2.2. 1 Bilayered organic:inorganic hybrid solar cells

The bilayered device is depicted in **Figure 1.15a**. These devices are processed in order to the required thickness of an active layer for sufficient absorption of light. As discussed above, the exciton diffusion length is very small and only few of the photogenerated exciton reaches the interface for successful dissociation into free charges. The interface between the donor and acceptor materials challenges the bilayer solar cells; therefore more research was focused on below structured devices.

1.3.2.2. 2 Blended organic:inorganic hybrid solar cells

The device structure of hybrid organic:inorganic hybrid solar cells is depicted in **Figure 1.15b**. The mixing of inorganic nanoparticles of Group II-VI semiconductors with organic polymers has proven to be successful. These materials can be processed from organic solvents such as chloroform, toluene, chlorobenzene and offer optimal blends for the preparation of photo active layers. These systems are reported to have a higher efficiency of 3.13 % when compared to other II-VI group semiconductors (quantum dots).[45] The toxic nature of Group II-VI semiconductor materials limits the use in solar cells. Therefore, an intensive research is focused on the use of semiconducting metal oxides as inorganic acceptors (i. e. TiO_2, ZnO etc). These inorganic acceptors offer low production cost and are non-toxic. The single crystalline metal oxides are interesting for solar cells due to their high electron mobility (0.1 -100 cm^2/Vs [46-51] depending on their crystallinity), highly transparent and easy processability.

These blended configurations are relatively easy to process. Limitations like morphology of the active layer, donor:acceptor interfaces for exciton dissociation and trapping of the charge carriers are hard to control. The solar cells prepared with organic:metal oxides in blends (P3HT:ZnO) in organic solvents had reached up to an efficiency of 2 %.[52] In this thesis work no attention was drawn towards these blended devices. Since this has already been explorated by other ONE^2 group members (e.g. PhD thesis of Ilse Haeldermans 2009)

1.3.2.2. 3 Organic semiconducting polymers filling into the inorganic structured hybrid solar cells

Another approach is to have inorganic semiconductors on conducting substrates developed as mesoporous layers or grown as vertically aligned nanotubes, nanorods or nanowires. The development of this type of systems is an extension of the DSSC either to replace the liquid electrolyte with polymers or to replace both liquid electrolyte and dyes with polymers. Such novel organic:inorganic hybrid solar cells were prepared and subjected to different characterization tools. The device structure is depicted in **Figure 1.15c**. The organic polymer combines the function of both photo-active and hole transporting layer. In this method, the metal oxide acts as an electron acceptor and provides an effective percolation path for the electrons to the transparent bottom electrode. Similarly, holes are transported to the top electrode. The power conversion efficiencies mainly depend on the infiltration of polymer into the inorganic semiconductor layers. The state-of-the-art hybrid solar cell using the Spiro-OMeTAD material (2,2',7,7'-tetrakis-(N,N-di-p-methoxyphenylamine)9,9'-spirobifluorene) obtained the highest efficiency of 6.1 %.[53] Several studies and techniques are implemented for understanding the infiltration of polymer into these layers. There is a need to have better control on the size distributions of oxide layers and more optimizations are required to improve the device performances. Some of the organic:inorganic hybrid solar cell device performances from the literature are presented in **Table 1.3**.

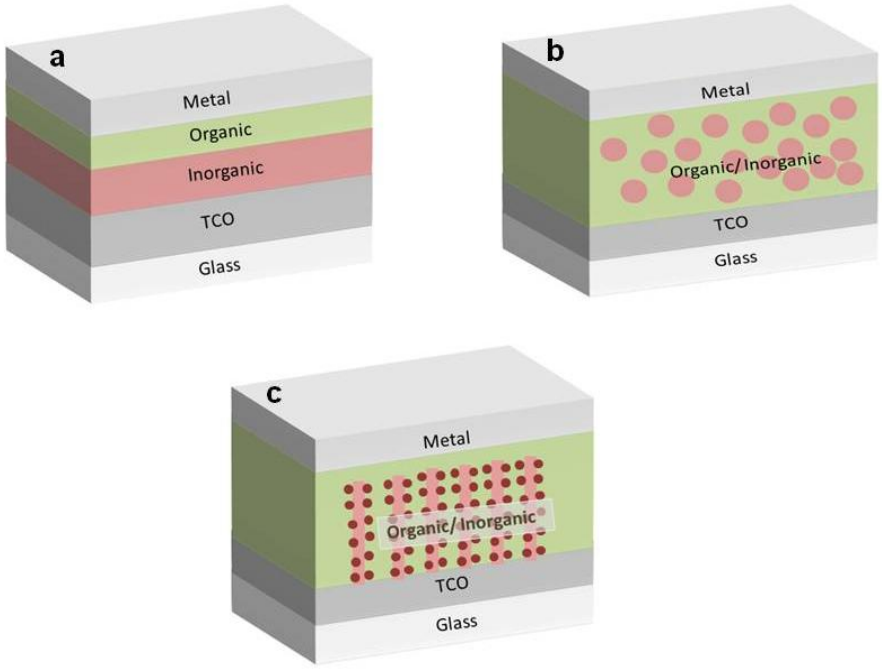

Figure 1.15: Three different configurations of organic:inorganic hybrid solar cells: (a) Bilayer hybrid solar cells (b) Blended organic:inorganic hybrid solar cells (c) Organic semiconducting polymers filling into the inorganic nanostructured hybrid solar cells (structured devices).

Table 1.3: Organic:inorganic hybrid solar device performances.

Material	Polymer	Device Type	V_{oc}	J_{sc}	FF (%)	η (%)	Ref
CdSe quantum dots	P3HT	blend	0.62	5.8	56	2	54
CdSe tetrapods	MDMO-PPV	blend	0.76	9.1	44	2.8	55
CdSe nanorods	P3HT	blend	0.62	8.7	50	2.6	56
TiO_2 nano-particles	Dye+ P3HT	structure	0.83	5.1	61	2.6	57
TiO_2 nano-particles	Dye+ Spiro-OMeTAD	structure	0.88	9.7	71	6.1	53
TiO_2 nanorods	P3HT	blend	0.78	4.33	65	2.2	58
TiO_2 nanorods	P3HT	structure	0.32	3.88	41	0.5	59
ZnO nano-particles	P3HT	blend	0.75	5.2	52	2	52
ZnO nanorods	P3HT	structured	0.54	2.67	53	0.7	60
ZnO	TSCuPc*	Bilayer	0.19	0.043	24	0.04	61

*TSCuPc - tetrasulfonate Copper Phthalocyanine

1.4 Aim and outline of thesis

The DSSCs and polymer based solar cells offer an alluring way for simple and low cost photovoltaics. In the area of photovoltaics research and development, the main goal is to fabricate a low cost photovoltaic device with sufficient stability and high efficiency. In this thesis, the organic: inorganic hybrid solar cells were investigated. Initially, the mesoporous nanostructured oxide layers were prepared with and without various dyes. Different types of photoactive and hole transporting materials were used to build these hybrid solar cells. After producing the cells, a systematic opto-electrical and morphological characterization on the devices has been performed in order to rationalize the device performances.

In chapter 2, the experimental techniques for optical, electrical and morphological characterizations used in this work are presented and briefly described.

In chapter 3, organic:inorganic hybrid solar cells were built by using different dyes for sensitizing the TiO_2 electrodes. Also detailed comparison was made between the photovoltaic devices with and without dye sensitizing. In these devices, P3HT is used as a photoactive and hole transporting layer. The absorption of these materials (TiO_2, TiO_2/P3HT and TiO_2/dyes/P3HT) was studied by using UV-Vis absorption spectroscopy. IV-characterizations were done on these devices followed by photocurrent measurements using Fourier transform photocurrent spectroscopy (FTPS). FTPS will points out the contribution of the dye to the photocurrent in these devices. Furthermore the charge transport, charge separation properties and life-time of the charge carriers were determined and explained by using charge extraction by linearly increasing voltage (CELIV) and transient photovoltage (TPV) techniques.

In chapter 4, small molecule:inorganic hybrid solar cells are investigated. Copper phthalocyanine (CuPc) was vacuum sublimated above TiO_2 electrodes with and without dye. The device performances and opto-electrical properties were studied. The charge transport properties and life-time of the charge carriers were investigated by using the CELIV technique. The charge separation and interface properties were studied by using FTPS and transient absorption spectroscopy (TAS) techniques.

Chapter 5 mainly introduces an eco-friendly preparation procedure for organic:inorganic hybrid solar cells. In this type of solar cells, the dye and P3HT were replaced by a water soluble polymer. The opto-electrical and morphological properties of different water soluble polymers were studied by using UV-Vis absorption spectroscopy, cyclic voltammetry (CV), hole-only diodes and field effect transistor (FET) measurements. Morphological characterizations were done by using scanning electron microscope (SEM), transmission electron microscope (TEM) and X-ray diffraction (XRD) on individual polymer layers and on complete devices. Based on these results, the polymer with the highest hole mobility was introduced above different TiO_2 electrodes by using an alternative new processing method for preparing eco-friendly organic:inorganic hybrid solar cells. Also the device performances were investigated.

In last chapter 6, conclusions are drawn and an outlook is formulated. An important outlook activity is related to the use of poly(isothianaphthene) (PITN) a low band-gap precursor polymer. The PITN oligomer solution can be introduced into nano-oxide layers and polymerized.

1.5 References

1. U.S. Census Bureau, International Data Base (IDB) - World Population - http://www.census.gov/ipc/www/idb/index.php (6-14-2011).
2. C. B. Hatfield, Nature 387 (1997) 121.
3. C. J. Campbell, J. H. Laherrère, Scientific American. (1998) 78.
4. http://www.eia.gov/forecasts/aeo/pdf/0383%282011%29.pdf.
5. B. Welker, REN21. 2010. Renewables 2010 Global Status Report.
6. US electricity production - http://www.eia.gov/electricity/.
7. International Energy Agency (2007). Renewables in global energy supply: An IEA facts sheet, OECD, 34 pages.
8. http://solardat.uoregon.edu/SolarRadiationBasics.html
9. P.R. Gast, "Solar Radiation", in Handbook of Geo- physics, ed. C.F. Campen et al, (1960) 14.
10. Solar spectrum and AM- http://rredc.nrel.gov/solar/spectra/am1.5/.
11. D. M. Chapin, C. S. Fuller, G. L. Pearson, J. Appl. Phys. 25 (1954) 676.
12. E. Arici, N. S. Sariciftci, D. Meissner, Encyclopedia of Nanoscience and Nanotechnology. 3 (2004) 929.
13. B. C. O. Regan, M. Grätzel, Nature 353 (1991) 737.
14. A. Yella, H-W. Lee, H. N. Tsao, C. Yi, A. K. Chandiran, M. K. Nazeeruddin, E. W-G. Diau, C-Y. Yeh, S. M. Zakeeruddin, M. Grätzel, Science 334 (2011) 629.
15. B. A. Gregg, J. Phys. Chem. B. 107 (2003) 4688.
16. L. M. Peter J. Phys. Chem. C. 111 (2007) 6601.
17. D. Matthews, P. Infelta, M. Grätzel, Sol. Energy Mater. Sol Cell. 44 (1996) 119.
18. D. Cahen, G. Hodes, M. Grätzel, J. F. Guillemoles, I. Riess, J. Phys. Chem. B. 104 (2000) 2053.
19. A. Mishra, M. K. R. Fischer, P. Bauerle, Angew. Chem. Int. Ed. 48 (2009) 2474.
20. M. K. Nazeeruddin, R. Humphry-Baker, P. Liska, M. Grätzel, J. Phys. Chem. B. 107 (2003) 8981.
21. P. Wang, S. M. Zakeeruddin, J. E. Moser, R. Humphry-Baker, P. Comte, V. Aranyos, A. Hagfeldt, M. K. Nazeeruddin, M. Grätzel, Adv. Mater. 16 (2004) 1806.
22. M. K. Nazeeruddin, P. Pechy, T. Renouard, S. M. Zakeeruddin, R. Humphry-Baker, P. Comte, P. Liska, L. Cevey, E. Costa, V. Shklover,

L. Spiccia, G. B. Deacon, C. A. Bignozzi, M. Grätzel, J. Am. Chem. Soc.123 (2001) 1613.
23. H. Qin, S. Wenger, M. Xu, F. Gao, X. Jing, P. Wang, S. M. Zakeeruddin, M. Grätzel, J. Am. Chem. Soc. 130 (2008) 9202.
24. F. Gao, Y. Wang, D. Shi, J. Zhang, M. Wang, X. Jing, R. Humphry-Baker, P. Wang, S. M. Zakeeruddin, M. Grätzel, J. Am. Chem. Soc. 130 (2008) 10720.
25. H. Choi, C. Baik, S. O. Kang, J. Ko, M.-S. Kang, M. K. Nazeeruddin, M. Grätzel, Angew. Chem. Int. Ed. 47 (2008) 327.
26. S. Hwang, J. H. Lee, C. Park, H. Lee, C. Kim, C. Park, M-H. Lee, W. Lee, J. Park, K. Kim, N-G. Park, C. Kim, Chem. Commun. (2007) 4887.
27. H. J. Snaith, L. Schmidt–Mende, Adv. Mater. 19 (2007) 3187.
28. H. Shirakawa, E. J. Louis, A. G. MacDiarmid, C. K. Chiang, A. J. Heeger, J. Chem. Soc., Chem. Commun. (1977) 578.
29. http://www.nobelprize.org/nobel_prizes/chemistry/laureates/2000/popular.html.
30. N. S. Sariciftci, L. Smilowitz, A. J. Heeger, F. Wudl, Science 258 (1992) 1474.
31. G. Yu, J. Gao, J. C. Hummelen, F. Wudl, and A. J. Heeger, Science 270 (1995) 1789.
32. J. Roncali, Chem. Rev. 92 (1992) 711.
33. H. W. Kroto, J. R. Heath, S. C. O. Brien, R. F. Curl. R. E. Smalley, Nature 318 (1985) 162.
34. A. Gadisa, W. D. Oosterbaan, K. Vandewal, J.C. Bolsée, S. Bertho, J. D'Haen, L. Lutsen, D. Vanderzande, J. V. Manca, Adv. Funct. Mater. 19 (2009) 3300.
35. V. D. Mihailetchi, J. K. J. van Duren, P. W. M. Blom, J. C. Hummelen, R. A. J. Janssen, J. M. Kroon, M. T. Rispens, W. J. H. Verhees, M. M. Wienk, Adv. Funct. Mater. 13 (2003) 43.
36. M. Theander, A. Yartsev, D. Zigmantas, W. Mammo, M. R. Andersson, O. Inganäs, Phys. Rev. B. 61, (2000) 12957.
37. D. E. Markov, C. Tanase, P. W. M. Blom, J. Wildeman, Phys. Rev. B. 72 (2005) 045217.
38. A. Baumann, T. J. Savenije, D. H. K. Murthy, M. Heeney, V. Dyakonov, C. Deibel, Adv. Func. Mat. 21 (2011) 1687.
39. G. Zhao, Y. He, Y. Li, Adv. Mater. 22 (2010) 4355.
40. F. Zhang, E. Perzon, X. Wang, W. Mammo, M. R. Andersson, O. Inganäs, Adv. Funct. Mater. 15 (2005) 745.
41. S. E. Shaheen, C. J. Brabec, N. S. Sariciftci, F. Padinger, T. Fromherz, J. C. Hummelen, Appl. Phys. Lett. 78 (2001) 841.

42. Y. Sun, C. J. Takacs, S. R. Cowan, J. H. Seo, X. Gong, A. Roy, A. J. Heeger, Adv. Mater. 23 (2011) 2226.
43. J. Hou, H-Y. Chen, S. Zhang, G. Li, Y. Yang, J. Am. Chem. Soc. 130 (2008) 16144.
44. F. C. Krebs, Sol. Energy Mater. Sol. Cells. 93 (2009) 394.
45. Y. Zhou, M. Eck, C. Veit, B. Zimmermann, F. Rauscher, P. Niyamakom, S. Yilmaz, I. Dumsch, S. Allard, U. Scherf, M. Krüger, Sol. Energy Mater. Sol. Cells. 12 (2011) 3227.
46. O. Carp, C.L. Huisman, A. Reller, Prog. Solid State Chem. 32 (2004) 33.
47. D. R. Coronado, G R. Gattorno, M. E. E. Pesqueira, C. Cab, R. de Coss, G. Oskam, Nanotechnology 19 (2008) 145605.
48. M. Koelsch, S. Cassaignon, J. F. Guillemoles, J. P. Jolivet Thin Solid Films. 403 (2002) 312.
49. M. Grätzel, Nature 414 (2001) 338.
50. H. Tang, K. Prasad, R. Sanjinès, P. E. Schmid, F. Lévy, J. Appl. Phys. 75 (1994) 2047.
51. K. Nakahara, H. Takasu, P. Fons, K. Iwata, A. Yamada, K. Matsubara, R. Hunger, S. Niki, J. Crystal Growth. 227 (2001) 923.
52. S. D. Oosterhout, M. M. Wienk, S. S. V. Bavel, R. Thiedmann, L. J. A. Koster, J. Gilot, J. Loos, V. Schmidt R. A. J. Janssen, Nat. Mater. 8 (2009) 818.
53. N. Cai, S-J. Moon, L. Cevey-Ha, T. Moehl, R. Humphry-Baker, P. Wang, S. M. Zakeeruddin, M. Grätzel, Nano Lett. 11 (2011) 1452.
54. Y. Zhou, F. S. Riehle, Y. Yuan, H.-F. Schleiermacher, M. Niggemann, G. A. Urban, M. Kruger, Appl. Phys. Lett. 96 (2010) 013304.
55. B. Sun, H. J. Snaith, A. S. Dhoot, S. Westenhoff, N. C. Greenham, J. Appl. Phys. 97 (2005) 014914.
56. B. Sun, N. C. Greenham, Phys. Chem. Chem. Phys. 8 (2006) 3557.
57. R. Zhu, C. Y. Jiang, B. Liu, S. Ramakrishna, Adv. Mater. 21 (2009) 994.
58. Y-Y. Lin, T-H. Chu, S-S. Li, C-H. Chuang, C-H. Chang, W-F. Su, C-P. Chang, M-W. Chu, C-W. Chen, J. Am. Chem. Soc. 131 (2009) 3644.
59. W. Ergang, W. Li, L. Linfeng, L. Chan, Z. Wenliu, P. Junbiao, C. Yong, Appl. Phys. Lett. 92 (2008) 033307.
60. L. Baeten, B. Conings, H-G. Boyen, J. D'Haen, A. Hardy, M. D'Olieslaeger, J. V. Manca, M. K. Van Bael, Adv. Mater. 23 (2011) 2802.
61. X. Luo, L. Xu, B. Xu and F. Li, Appl. Surf. Sci. 257 (2010) 6908.

Chapter 2:Experimental Techniques

Physics behind the solar cell necessitates the know-how for improving the device performances further. As a part of this optical, electrical and morphological properties of the materials used in the devices were studied. The optical properties of the materials were examined by using UV-Visible absorption spectroscopy and transient absorption spectroscopy measurements. The surface wetting property was studied by using contact angle measurement. Various electrical measurements like fourier transform photocurrent spectroscopy-external quantum efficiency measurements, charge extraction by linearly increasing voltage, transient photovoltage and transient photocurrent, cyclic voltammetery, field-effect transistor measurements, relative dielectric permittivity studies and space charge limited current techniques were employed. For morphological characterization, transmission electron microscope, x-ray diffraction and scanning electron microscopy were used. The techniques used for this thesis are shortly explained in this chapter.

2.1 Optical characterization

2.1.1 UV-Vis absorption measurements

UV-Vis absorption spectroscopy is a technique used to identify the characteristic absorption spectrum of a compound. The UV-Vis region covers the wavelength between 200 nm and 800 nm. The working principle behind absorption spectroscopy is the well-known Lambert – Beer law as described by equation 2.1:

$$A = \varepsilon bc \qquad (2.1)$$

where A is the absorbance and is given as

$$A = \log\left(\frac{\text{Intensity of incident light on the sample}}{\text{Intensityof light transmitted through sample}}\right)$$

ε is the molar absorptive ($M^{-1}cm^{-1}$), b is the path length of the light in the sample (cm) and c is the concentration of the solution (M).

Molecules absorb light energy and electrons are elevated from the HOMO to excited states into the LUMO. This leads to the characteristic absorption spectra and forming corresponding excited states as depicted in **Figure 2.1**. The band offset of an absorption spectrum represents the HOMO-LUMO energy gap.

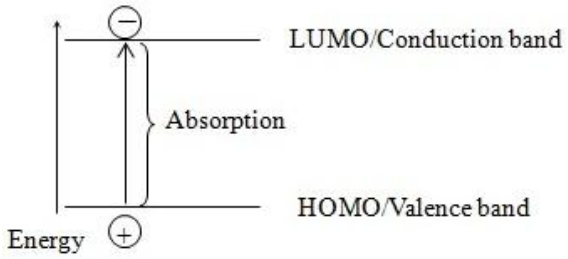

Figure 2.1: Energy level diagram for obtaining the absorption spectrum.

The absorption spectrometer used in this work, consists of four major parts and the block diagram is shown in **Figure 2.2**.

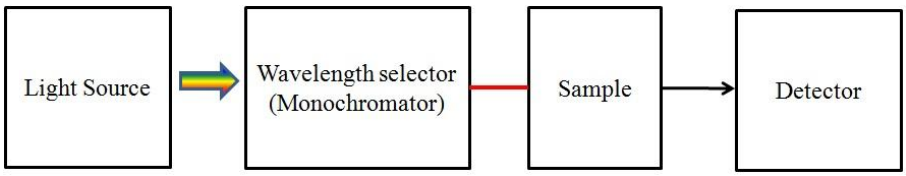

Figure 2.2: Block diagram of the UV-Vis spectrometer.

The light source used in UV-Vis spectroscopy is a deuterium lamp, whose output is mainly in the UV range (115 nm – 350 nm) and diminishes by approaching towards the visible range. Halogen lamps are used for the visible region (250 nm - 2500 nm). A monochromator is used for the wavelength selection. The sample compartment can hold both solid (films) and liquid samples. In this work, glass substrates were mostly used for depositing polymer thin films. The light detector is a photomultiplier tube and this detects the transmitted light through the sample.

In this thesis a Cary 500 Scan UV-Vis-NIR spectrophotometer was used for recording the absorption spectra.

2.1.2 Transient absorption spectroscopy measurements (TAS)

TAS was developed by the Nobel laureate of 1967, i.e. chemist G. Porter[1]. This technique helps in understanding the physical and chemical reactions of transient species which have a very short life-time. It is capable of observing molecular motions from absorption spectra of transient species and also the decay kinetics of these species. In this thesis, TAS measurements were used to study and understand the charge separation properties and optically active long-lived charge carriers. The TAS measurements were performed at the Prof. Dr. Emilio Palomares group ICIQ-Spain

In this method, light is used to excite molecules from ground state to higher energy excited state. The excited molecules are further excited to even higher energy states upon by the absorption of a second laser pulse. The obtained absorption spectrum of the excited state molecules gives information about transient species. This is the working principle of TAS. When a short pulse of light (the excitation pulse) is focused, the consequent change in the sample, the change in optical density (OD) is observed. The change in OD is determined by transmission of a second light beam (probe) focused on the sample. This provides kinetic data on the decay of transient species. The probe wavelength can be varied in between 400 nm - 1000 nm. A time delay of 100 µs is chosen after the excitation pulse to obtain the absorption spectra of transient species.

The block representation of a TAS setup is shown in **Figure 2.3**. The excitation source used was a N_2 laser. This laser produces laser pulses at a wavelength of 337 nm. A variable source of dye laser was used with the N_2 laser to get the wavelength in between 400 nm - 1000 nm. A light guide was used to transmit the excitation pulse to the sample. A tungsten lamp was used as the probe-light source. From monochromator 1, the selected wavelength from the lamp was probed on the sample. Monochromator 2 was used to reduce the emission intensity of second N_2 laser, light scatters after passing through the sample and reaches towards the photodiode detector. The detection system was a Si photodiode and an optical transient voltage amplifier coupled to a Tektronix oscilloscope. Excitation and probe wavelengths were varied according to the absorption maximum of the samples under investigation in this work.

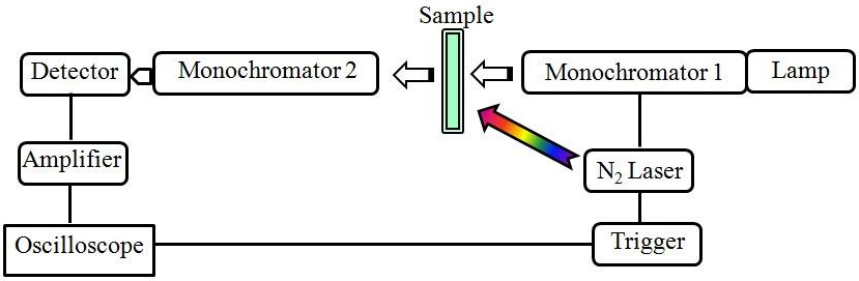

Figure 2.3: Block representation of a TAS setup.

The data collected by the oscilloscope was converted to units of ΔOD. The change in optical density was calculated by using equation 2.2.

$$\Delta OD(t) = \alpha \times \frac{V(t)}{V_0} \qquad (2.2)$$

where V(t) is the transient signal size which is proportional to the light intensity, V_0 is the dc voltage level, which is proportional to the intensity of the probe light. The constant α is the amplification factor, which in the present apparatus has a value of 2.3.

2.2 Contact angle measurements

The sessile drop method was performed with OCA 15 Plus contact angle setup. This device drops an accurate volume of water on the sample surface. The droplet as a function of time was recorded with a video camera and later the contact angle is evaluated with a software package. This technique was used to investigate the sample surface wetting property. The lower contact angle (0^0 to 30^0) resembles a hydrophilic surface, a higher contact angle (> 90^0) points to a hydrophobic surface.

2.3 Electrical characterizations

2.3.1 External quantum efficiency measurements (EQE)

The direct External Quantum Efficiency (EQE) or Incident Photon-to-Current Conversion Efficiency (IPCE) is the number of photogenerated electrons (N_e) produced per incident monochromatic photons (N_p). Apart from determining the solar cell device parameters, it is also important to be determined and the formula is given as in equation 2.3.

$$EQE\ (\lambda) = \frac{N_e}{N_p} = \frac{I_{sc}(\lambda)\ /\ e}{P_{in}(\lambda)\ /(hc\ /\ \lambda)} = \frac{1240 I_{sc}}{P_{in}\lambda} \qquad (2.3)$$

where h is Planck's constant, c is the speed of light, λ is the wavelength of the light beam, e is the elementary charge of the electron, I_{sc} (λ) is the photocurrent generated in short circuit mode and P_{in} is the incident light power.

EQE measured at different wavelengths results in a spectral response of the solar cell. EQE follows the absorption trend of the active layer.[2] If the EQE is integrated over the whole solar spectrum, the short circuit current (J_{sc}) of the solar cell can be calculated.

Fourier transform photocurrent spectroscopy (FTPS) is a photocurrent based technique. This technique helps in understanding the optical absorption at low energies and therefore allows the characterization of sub-bandgap absorption phenomena.[3-5] With FTPS it is also possible to measure the photocurrent EQE spectra of photovoltaic devices over several orders of magnitude. FTPS is introduced by Vanecek et al.[6] It is a fast and sensitive technique for the simultaneous characterization of optical and electrical properties of solar cells.

The basic principle behind FTPS is similar to fourier transform infrared (FTIR) spectroscopy. The block diagram of FTPS is depicted in **Figure 2.4**. The FTIR spectrometer, a light beam (from a halogen lamp) is directed through an aperture entering a Michelson interferometer, equipped with one fixed mirror and one constant speed movable mirror. The position of the movable mirror is recorded by counting the number of interference fringes from a beam. This

follows the same path as the main beam in the interferometer to form constructive interference fringes. The (solar cell) sample works as a detector, either in a coplanar contact configuration or transverse configuration (photovoltaic mode). A voltage bias is applied between the contacts in order to extract the photocurrent of device.

When the sample is illuminated from the output beam, the produced photocurrent depends on the monochromatic light quantity, measurable wavenumber ($\bar{\nu}$) of the light beam, and the optical path length ($\delta = 2vt$) introduced by the moving mirror (at a constant velocity v) of the interferometer as depicted in equation 2.4.

$$I(\delta) = \int_0^\infty B(\bar{\nu}) D(\bar{\nu}) \cos(2\Pi\, \bar{\nu}\delta) d\bar{\nu} \qquad (2.4)$$

where $B(\bar{\nu})$ is the intensity of the polychromatic light source and $D(\bar{\nu})$ is the spectral dependence of the solar device. The fourier transformation of the measured interferogram $I(\delta)$ gives the single-beam IR spectrum.

The photovoltaic device was connected to the sample holder. For the photocurrent measurements, the light beam originates from a Thermo Electron Nicolet 8700 FTIR spectrometer. This was equipped with a quartz beam splitter for the detection in the visible and infrared regions from a halogen light source. This covers the wavelength in the range of 400 nm – 3000 nm. Further, it consists of an external light beam output and can operate with an external detector. The obtained FTIR signal of the sample is corrected to the signal from the spectral independent detector. The FTIR spectrometer is equipped with a pyrodetector and a Si photodiode. The FTPS measurement resolution was set to 32 cm^{-1}. The finally obtained spectrum by FTPS is the assembly of two or three partly overlapping spectra obtained by using different optical filters.

The obtained photocurrent is amplified by a preamplifier. The resulted output voltage is digitized by an analog/digital converter of the external interface and sent back to the spectrometer.[6] All FTPS spectra presented are corrected by a spectrally independent detector. In this way, the FTPS spectra give relative EQE_{pv} when compared to the absolute EQE %. In this work FTPS-EQE_{pv} measurements were performed on the hybrid solar cells.

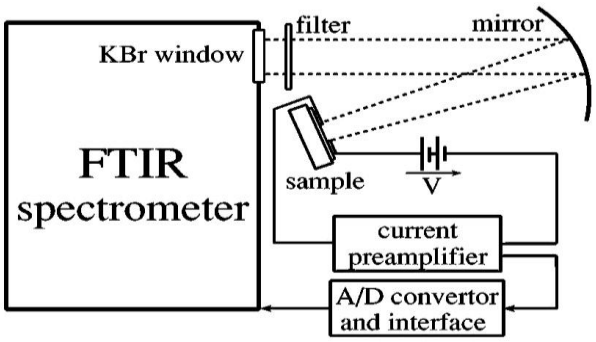

Figure 2.4: Block diagram of fourier transform photocurrent spectroscopy.

2.3.2 Charge extraction by linearly increasing voltage measurements (CELIV)

Charge extraction by linearly increasing voltage (CELIV) [8-10] was implemented for the first time on the model devices used in this work at our lab i.e. on TiO_2/P3HT, TiO_2/N719/P3HT, TiO_2/C101/P3HT and TiO_2/C101/CuPc hybrid solar cell devices. During the CELIV measurement, a linearly increasing voltage was applied to the device. The resultant CELIV signal is the current response comprising of a capacitive part and an extraction current. CELIV is used to measure on the real solar cells with thinner active areas which is a major advantage when compared with other measurement techniques (time of flight technique, double-injection technique etc.). With the other measurement techniques optically thick samples are required which influence charge carrier transit time and energy relaxation time. During the CELIV measurement, solar cells were reverse biased to prevent from the injection of carriers and giving rise to direct charge carrier mobilities of that particular device. The sign of the charge carriers cannot be determined by CELIV. Another limitation is the measurable voltage range. A typical CELIV transient is shown in **Figure 2.5**.

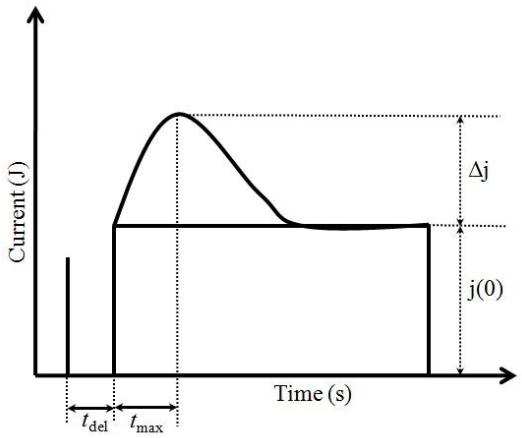

Figure 2.5: Typical CELIV transient signal.

where, t_{max} is the time at which the extraction current reaches its maximum. j(0) is the geometric capacitance displacement current of the sample and Δj is the difference between maximum current (J) and j(0). For photo-CELIV measurements, a laser pulse is applied and t_{del} is the time delay between the laser pulse and the voltage extraction.

In the CELIV technique (dark) the device was shorted, which limits the amount of free charge carriers equilibrium. Therefore, photo-CELIV is an extended version of the CELIV technique is used in this work. In this case, a laser light pulse precedes the carrier extraction in order to increase the amount of free charge carrier equilibrium. By this method, the transit time of the charge carriers will be smaller and the mobility of the charge carrier is increased. There are different stages before obtaining the mobility in photo-CELIV. The photo-CELIV transient looks similar to CELIV transient signal as shown in **Figure 2.5**. By photo-CELIV the photogenerated charge carries undergo recombination or extracted under built-in-field. This was compensated by determining the built-in-field of device i. e. offset voltage. At the same time, some of the charge carries might relax towards the tail states of the density of states. The remaining charge carriers are extracted by using a voltage pulse. Later, different delay times are applied in between the laser light pulses and extraction voltage. By calculating the number of extracted charge carriers as a function of delay time between light pulse and extraction, it is possible to estimate the life-time of long-lived charge carriers. The loss of charge carriers can be either from recombination or via deep trapping. For devices where the loss of charge carriers is from recombination, a recombination constant can be calculated.

In this study, CELIV was used with a triangular-shaped voltage pulse to extract the equilibrium charge carriers of the devices, without and with a laser light pulse at different delay times. This is shown in **Figure 2.6**.

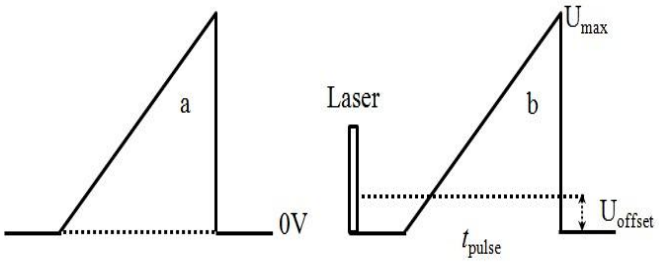

Figure 2.6: Triangular shaped voltage pulse for the extraction of charge carriers with and without laser pulse in CELIV.

where U_{max} is the maximum voltage and U_{offset} is the built-in-field. In some devices, symmetric electrodes with similar work functions are used that match the Fermi level of the semiconductor. In the rest of the devices, one of the working electrodes acts as a blocking electrode to avoid the additional injection of charge carriers during measurements. The built-in-field is not yet clearly understood and needs more research. In these devices, the compensation of the built-in-field was measured approximately i.e. the V_{oc} of a solar cell device. This was used in these measurements that ensure the flat-band condition.

The samples were kept in the dark, and charge carriers were extracted by linearly increasing voltage pulses applied by a digital function generator (Tektronix, AFG 3101). The CELIV and photo-CELIV transients were recorded using a digital oscilloscope (Tektronix, TDS, 620B) of 1 MΩ resistance and also using a set of variable resistances max 50 Ω. The delay time between the laser light pulse and the voltage pulse was varied using a digital delay programmed shutter. The signals were processed by using Labview software. Devices were illuminated from the FTO side. With N_2 laser light pulse of wavelength 337 nm was used. The complete block diagram of the setup is shown in **Figure 2.7**. The mobility of the fastest charge carriers was obtained by using equation 2.5.[8-10]

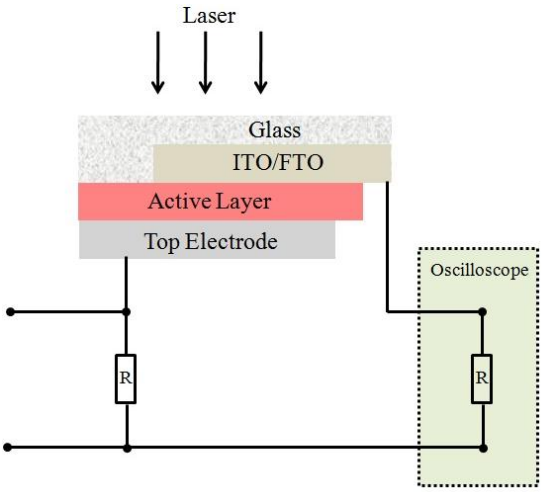

Figure 2.7: The complete block diagram of CELIV setup.

$$\mu = \frac{2d^2}{3At_{max}^2 \left[1 + 0.36\frac{\Delta j}{j(0)} \right]} \tag{2.5}$$

where μ is the mobility of the charge carriers, d is the thickness of the device, A is the voltage rise speed.

The recombination kinetics were studied using a bimolecular recombination formula equation 2.6.[8-10]

$$n(t) = \frac{n_0}{1 + n_0 \beta t} \tag{2.6}$$

where β is the bimolecular recombination coefficient (cm^3/s), n_0 and n(t) are the initial density and density of photo-generated charge carriers (cm^{-3}) respectively.

Bimolecular life-time t_β (s) of the long lived charge carriers is obtained using equation 2.7. [8-10]

$$t_\beta = (n_0 \beta)^{-1} \quad (2.7)$$

2.3.3 Transient photovoltage and transient photocurrent measurements (TPV and TPC)

Charge transport properties in solar cells are studied by using various techniques. However, numerous measurements for recombination are made under open circuit conditions.[11] It is well-understood that the recombination and charge carrier transport in solar cells have a strong relation with voltage.[11] The study of charge carrier transport near V_{oc} is an important contribution to the development of predictive models for solar cell behavior.

In this work, extracted charge carrier life time, charge carrier density and recombination rates obtained at different V_{oc}'s (varying the light intensity) were determined by using transient photovoltage (TPV) and transient photocurrent (TPC) techniques. The TPV measurements were performed at open-circuit conditions. This was first employed to study the charge carrier life time in DSSCs.[11, 12]

In this work the TPV measurements were conducted on TiO_2/P3HT, TiO_2/N719/P3HT and TiO_2/C101/P3HT hybrid solar cell devices. The devices were connected to 1 MΩ input terminal of a digital oscilloscope (Tektronix, TDS, 620B). The schematic block diagram of TPV is shown in **Figure 2.8a**. From an adjustable intensity halogen lamp the measurements were performed by varying the light intensities ~ 0.1 - 1.5 suns for obtaining different V_{oc}'s. The photovoltage for these measurements was driven by a controlled laser N_2 pulse of wavelength 337 nm. This was used as a small optical perturbation which resulted in a voltage transient with an amplitude $\Delta V_0 << V_{oc}$. The intensity of the laser pulse was attenuated as it is necessary to have $\Delta V_0 \leq 10$ mV, where no external current can flow through the external circuit. Thus, the generated charge carriers were maintained to remain in bulk of the device or in the vicinity of the electrodes. The decay of the photovoltage was recorded using an oscilloscope. Obtained profile of TPV decay was used for simplifying the quantitative analysis. The decay curves are presented in Chapter 3.

The Transient photocurrent (TPC) block diagram is depicted in **Figure 2.8b.** This was used to estimate the amount of additional photogenerated charge carriers (ΔQ) that were created due to the laser pulse intensity in TPV studies. The TPC uses the same experimental setup as used for measuring TPV transients. However in TPC, an additional small load resistor 50 Ω was inserted in series with the device. The voltage across the load resistor was detected by using an oscilloscope. The measurements were done in dark/low incident light intensity.

The estimation of ΔQ was required for the calculation of an effective capacitance (C = ΔQ/ΔV0) of the device. This was performed at different light biases and further can be used in the determination of the charge density present in the active layer of the device.

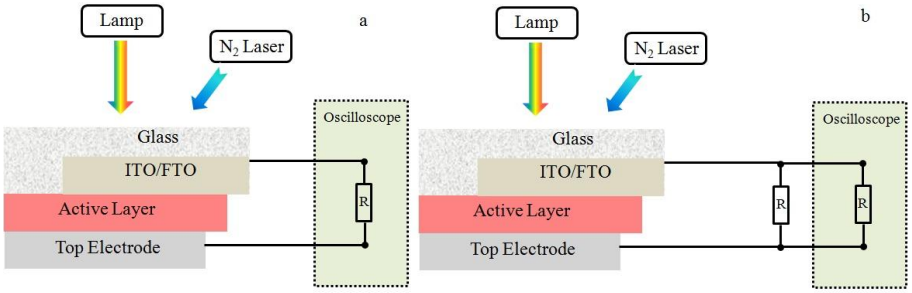

Figure 2.8: Schematic block diagram of TPV (a) and TPC (b).

The TPV decay curves were fitted with the exponential equation 2.8 to extract the life time of the charge carriers. Where ΔV is the amount of voltage generated by the bias light, ΔV_0 is the voltage change by a adding small perturbation by a laser pulse, t is the transit time and τ is the life time of the charge carrier.[13-15]

$$\Delta V = \Delta V_0 \exp \frac{t}{\tau} \qquad (2.8)$$

The TPV technique can also be used to determine the charge carrier concentration (n) and the bimolecular recombination coefficient of the charge carriers. [13-15]

The charge carrier density (n) present in the photoactive layer of the devices is estimated by using equation 2.9.[9-11]

$$n = \frac{1}{Aed}\int_{0}^{V_{oc}} C(V)dV \qquad (2.9)$$

where A is the device active area, e is the elementary electronic charge, d is the thickness of solar cell device (~ 900 nm) and C is the measured capacitance (60 - 140 nF/cm^2). The C was found to increase exponentially with increasing V_{oc} and extrapolated back to V = 0 to estimate C(V)dV.

The bimolecular recombination coefficient (β) was determined by using equation 2.10. [13-15]

$$\beta = \frac{n^{\lambda-1}}{(1+\lambda)\tau_{\Delta n0} n_0^{\lambda}} \qquad (2.10)$$

where λ, n_0 and $\tau_{\Delta no}$ are experimentally determined constants corresponds to the empirical reaction order with respect to n.[13-15]

2.3.4 Cyclic voltammetery measurements

Cyclic voltammetry (CV) is an electrochemical method which analyses the electrochemical behavior of electro active materials. The symmetrical setup of a CV measuring system is depicted in **Figure 2.9**. Thin film electrochemical measurements were performed with an Eco Chemie Autolab PGSTAT 20 Potentiostat/Galvanostat using a conventional three-electrode cell under N_2 atmosphere (electrolyte: 0.1 M TBAPF6 in anhydrous CH_3CN). For these measurements, an $Ag/AgNO_3$ reference electrode (0.01 M $AgNO_3$ and 0.1 M TBAPF6 in CH_3CN), a platinum counter electrode and an indium-tin oxide (ITO) coated glass substrate as working electrode were used. The polymers were drop casted thin films directly onto the ITO substrates. Cyclic voltammograms were recorded at a scan rate of 50 mV/s. All the potentials were referenced using a known standard ferrocene/ferrocinium, which in CH_3CN solution is estimated to have an oxidation potential of -4.98 eV vs. vacuum.

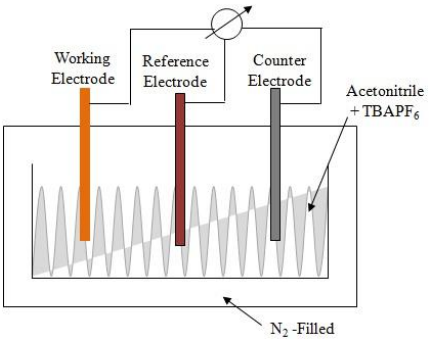

Figure 2.9: Symmetrical setup of a CV measuring system.

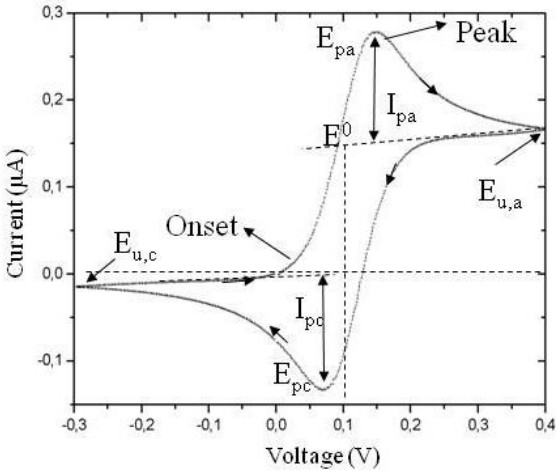

Figure 2.10: The CV of a reversible ferrocene system acetonitrile solution with TBAPF6.

Figure 2.10 shows a CV of an electrochemical reversible reaction of ferrocene used as an example. $E_{u,c}$ and $E_{u,a}$ represent the cathodic and anodic reversible potentials, respectively. E_{pc} and E_{pa} represent the potentials with respect to the peak currents I_{pc} (cathodic) and I_{pa} (anodic) respectively. The ferrocene shows a completely reversible behavior. A calibration of the measurement setup can be done by taking into account the E_0 value compared with the absolute values of ferrocence vs. $Ag/AgNO_3$ electrode (0.54 eV)[16]. The calibration process has been done for the complete CV graphs. The half wave potential $E_{1/2}$ is calculated by averaging E_{pa} and E_{pc}. The ionization potential I_p and the electron affinity E_a determine the HOMO

and LUMO levels respectively. The HOMO and LUMO values are estimated by using equations 2.11 and 2.12.

$$I_p = -(E_{pa} + 4.98) eV \quad (2.11)$$

$$E_a = -(E_{pc} + 4.98) eV \quad (2.12)$$

2.3.5 Field-effect transistor characterization (FET)

A short introduction about FET measurements, working principle and the determination of charge carrier mobilities by field effect transistor (FET) measurements is discussed in this section.

Even though the working principle of FET is known since in 1925, only 20 years after the transistor effect is observed in Bell's lab. The first FETs are produced on metal-oxide semiconductors in 1960's.[17, 18] In 1987, the first organic field-effect transistor based on polymers is developed by Koezuka et al.[19].

Figure 2.11 shows the schematic representation of an organic field effect transistor (OFET). An organic polymer thin film is deposited on top of a gate-insulator layer and contacted with metallic source and drain electrodes. Ideally, the source and drain form an ohmic contact with the active polymer layer. The voltage applied across the source and drain contacts is referred as the source-drain voltage (V_{ds}). If V_{ds} is increased, more and more charge carriers are drawn at the drain. For an applied V_{ds}, the amount of currents that flows through the polymer film from the source to drain electrodes is a function of gate-source voltage (V_{gs}). Ideally, when no V_{gs} is applied, the polymer film conductance is low, i.e. no generation of mobile charge carriers and the device is in "off-state". By sweeping V_{gs} the charge carriers are accumulated as a result of change in resistance of the channel. At this point the transistor is in "on-state" and source contact is grounded.

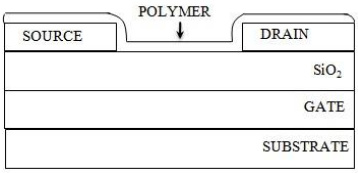

Figure 2.11: Schematic representation of OFET.

To obtain the hole current a negative voltage is applied across V_{gs} and V_{ds}. The holes accumulate near to the interface with the insulator SiO_2. As a consequence, the current saturates. This region is known as the saturation regime and by using equation 2.13 the mobility of the holes can be obtained.

$$I = \frac{WC_0}{L}\mu(V_{gs} - V_T)(V_{ds}) \qquad (2.13)$$

with W the channel width, C_0 the capacitance per unit area of the dielectric SiO_2 (C_0=16.9 nF cm^{-2}), L the channel length, μ the mobility and V_{gs}, V_T, and V_{ds} the gate-source, threshold and drain-source voltages respectively. The FET substrates were purchased from Philips (heavily electron doped Si layer that serves as a gate electrode; a ~200 nm dielectric layer of SiO_2, a 100 nm gold layer evaporated on a 10 nm titanium film forming the source and drain contacts). The SiO_2 surface is treated with hexamethyldisilazane (HMDS) for improving the film adhesion and formation.[20] Channel widths were 10 mm or 20 mm while the length was 30 μm or 40 μm. There was no light focused during these measurements. All OFET measurements were performed in a N_2 filled glove box.

2.3.6 Relative dielectric permittivity measurements

By using impedance spectroscope (IS) the relative dielectric permittivity (ε_r) of conjugated polymer materials was estimated. The relative dielectric permittivity of all the organic semiconducting materials was in between 2 and 4 [21, 22]. The low ε_r in the semiconducting materials has a direct influence on the generated excitons. The excitons are very strongly bounded.[23-28] High values of ε_r weakens the bounded excitons. This could pave a way for the better separation of excitons and has an effect on the performance of solar

cells [21, 22]. This emphasizes the importance in our work to measure the ε_r of water soluble conjugated polymers.

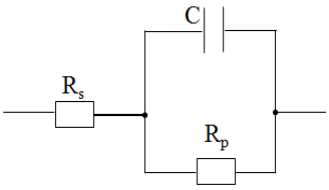

Figure 2.12: Randels equivalent circuit.

An equivalent circuit of the polymer material sandwiched between two electrodes is shown in **Figure 2.12**, which is also known as Randles circuit. The series resistance R_s represents the resistivity from the electrical contacts. R_p represents the parallel resistance which reflects the charge transfer mechanism of the polymer material. C is the capacitance of the polymer material sandwiched between the parallel plates. By applying an AC voltage with circular frequency ω, the impedance Z is given by the equation 2.14.

$$Z = R_s + \frac{1}{\frac{1}{R_p} + i\omega C} \tag{2.14}$$

For the above equivalent circuit (**Figure 2.12**), all the parameters can be estimated by fitting with equation 2.14. The Nyquist plot is obtained between the imaginary part and real part of impedance as shown in **Figure 2.13**. The R_s (high frequency) and R_s+R_p (low frequency) and the circular frequency maximum ω_{max} with the capacitance C is calculated by using equation 2.15.

$$C = \frac{1}{\omega_{max} R_p} \tag{2.15}$$

After obtaining the geometric capacitance C of the polymer material sandwiched between the two electrodes, the relative dielectric permittivity ε_r was calculated by using equation 2.16.

$$C = \varepsilon_0 \varepsilon_r \frac{A}{d} \tag{2.16}$$

where ε_0 is the vacuum permittivity 8.85 x 10^{-12} F/m, C is the determined capacitance and A/d is the device geometry (active area/film thickness).

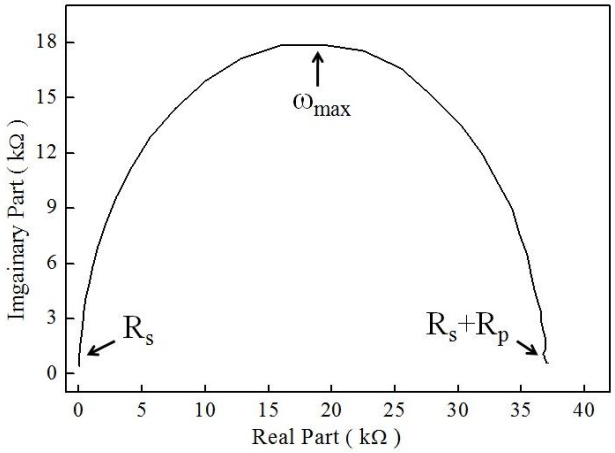

Figure 2.13: Nyquist plot obtained between the imaginary part and real part of the impedance.

2.3.7 Space charge limited current measurements (SCLC)

With the help of SCLC measurements, the charge transport properties of different polymers are estimated. In this method the polymer is sandwiched between the two electrodes, where the charges are injected into the bulk of a polymer film and IV-characteristics are measured simultaneously. The work functions of the electrodes are chosen such that at the positive electrode charges are injected (holes) into the HOMO of the polymer, while the other electrode collects these holes by avoiding the injection of electrons. In order to measure the hole mobility from the diodes, high work function metals like Ag, Au and Pd are evaporated. In working solar cells, the photogenerated or injected charge carriers in the bulk of the polymer layer have to reach the electrodes through the mechanism of diffusion, drift or both. These charge transport mechanisms can be identified with SCLC. In

this section, various features of a typical IV-characteristic of a diode measured in the dark, under forward bias discussed briefly. Three main transport features can be identified i.e. a low bias regime (R1), an intermediate regime (R2) and a high bias regime (R3) as shown in **Figure 2.14a**.

The low bias regime (R1); This region is characterized by an ohmic flow of charges and can be formulated as $J \propto \frac{V}{d}$, where J is the current density, V is the applied bias voltage and d is the thickness of the active layer. In this regime obtained IV-curve of the device is linear and symmetric.[29]

The intermediate regime (R2); Increasing the bias voltage causes a decrease an internal electric field, which enhances the injection of charge carriers from the electrodes into the bulk of polymer. A sharp slope usually determines the injection-limited (IL) region and the current increases exponentially with bias voltage. The current can be formulated as $J \propto \exp(eV/k_B T)$, where T is the absolute temperature, k_B is the Boltzmann constant and e is the elementary charge. The R2 regime is governed by the several factors related to the polymer/metal interfaces.[29]

The high bias regime (R3); After a certain level of bias voltage, it compensates the built-in voltage (V_{bi}) of a diode (i.e flat band can be observed). The current injection becomes higher. However, due to the low charge carrier mobility and the presence of traps in the polymer film, the injected charge carriers can reduce and more charges accumulate in the bulk of the polymer layer. At this resulting saturated current, the transport of the charge carriers is controlled by the space charge limited current (SCLC) and this is formulated as $J \propto \frac{V^2}{d^3}$

In order to determine the mobility of the charge carriers, the R3 regime is assumed to be trap free. This transport region is fitted by using Mott-Gurney's square law equation 2.17 and is often known as the trap free square law or Child's law.[29]

$$J = \frac{9}{8} \varepsilon_0 \varepsilon_r \mu \frac{(V - V_{bi})^2}{d^3} \qquad (2.17)$$

where ε_0, ε_r are the dielectric permittivity of free space and polymer material respectively, μ is the mobility, V_{bi} is the built-in voltage and d is the film thickness. V_{bi} can be estimated from the difference in the work function of contact electrodes and depends the process of device preparation. Experimentally V_{bi} is determined by the position of transition point between the injection current and SCLC. With the help of $J \propto \frac{V^2}{d^3}$ the log-log plot of the IV-curve in the SCLC region is shown in **Figure 2.14b**. The linear slope (red line) is measured two, which indicates that the current is approximately proportional to the square of the voltage.

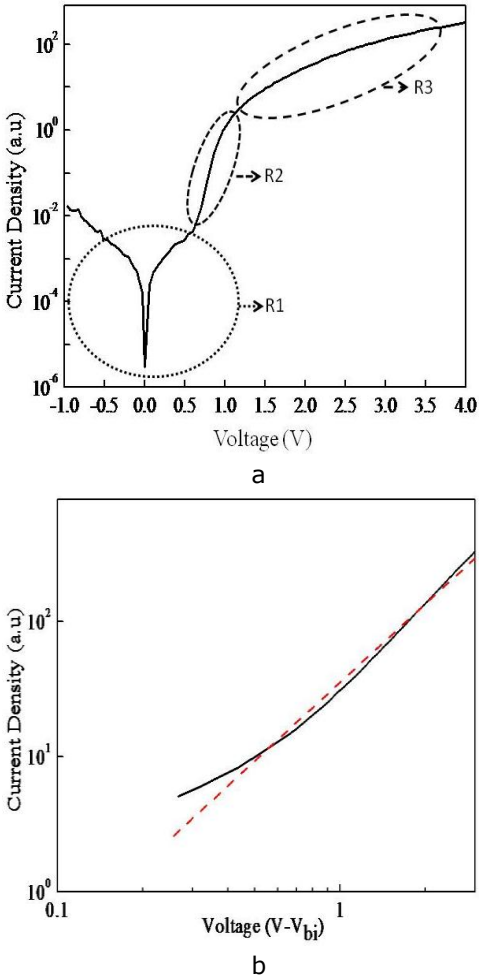

Figure 2.14: (a) Various features of a typical IV-characteristic of diode and (b) The log - log plot of IV-characteristic curve with linear fitting in red line.

2.4 Morphological characterization

2.4.1 Transmission electron microscope (TEM)

The schematic representation of TEM is depicted in **Figure 2.15**. A highly energetic beam of monochromatic electrons is produced by an electrically heated tungsten filament. A FEI Tecnai G2 Spirit Twin is available at IMO-IMOMEC in which electrons are emitted and accelerated across a potential difference of 120 kV.

There are three types of electromagnetic lenses used to obtain the final image by TEM i.e. condenser, objective and intermediate/projector. There are two types of condenser lenses. The main function of the first condenser lens is to control the spot size that determines the size range; the second condenser lens used as an intensity/brightness controller determining the electron beam from disperses spot to a pinpoint which uniformly strikes the sample. The transmitted part of beam from the sample is then focused by the objective lens. The high angle diffracted electrons are blocked by the objective aperture contributing to the contrast of the TEM image. The transmitted part of the image is illuminated on an image plane of the objective lens and the intermediate/projector lens is used to enlarge the final magnification required. Finally the magnified image is observed on a photographic screen or recorded with a CCD camera.

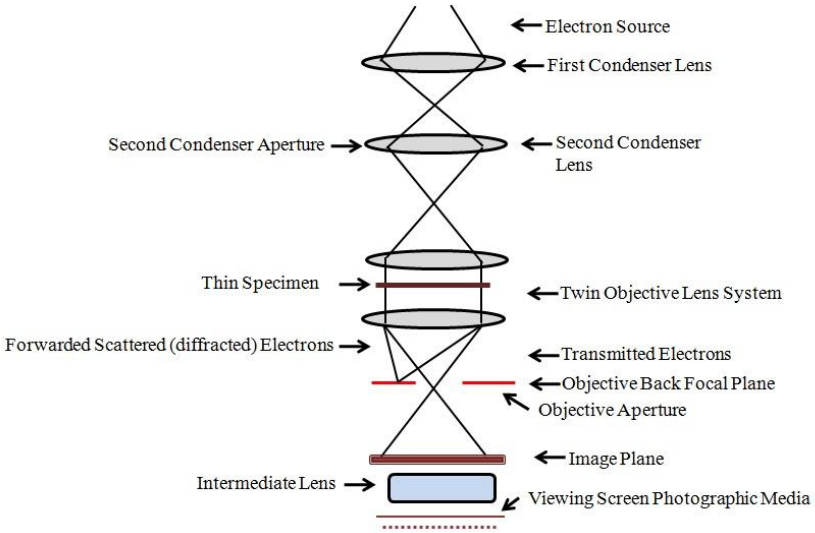

Figure 2.15: Schematic and important components of TEM

TEM can also produce a diffraction pattern for a specific region of the sample by adjusting the strength of the projector and the intermediate lenses. This helps in understanding the crystalline properties of polymers using diffraction principle.

Energy-dispersive X-ray spectroscopy (EDS or EDX) in TEM is a technique that allows for the determination of qualitative and quantitative chemical sample composition at current beam position in the sample. This system makes use of atoms of different chemical elements emitting X-rays at different characteristic energies. When a high energy beam strikes the sample, a discrete range of signals are emitted and these signals are generated by characteristics of X-rays. The obtained energy spectrum by an EDX is collected by a silicon detector.

2.4.2 Scanning electron microscope (SEM)

The scanning electron microscope (SEM) is an instrument that brings a largely magnified image by using a focused beam of high-energy electrons. The systematic representation of SEM is shown in **Figure 2.16**. From the

electron gun (at the top of microscope) a beam of electrons are produced. The complete measurements were held in vacuum and the electron beam follows a vertical path in the microscope. The beam proceeds through electromagnetic fields, lenses and is finally focused toward the sample. Once the beam collides with the sample, electrons and X-rays are ejected from the sample. Detectors collect ejected X-rays, backscattered electrons (BSE) and secondary electrons (SE), convert them into a signal and sent to a computer for further magnifications followed by displaying the final image. BSE analysis gives the composition information and SE analysis gives the topography of the sample. A FEI XL 30 high resolution SEM was used in this thesis work.

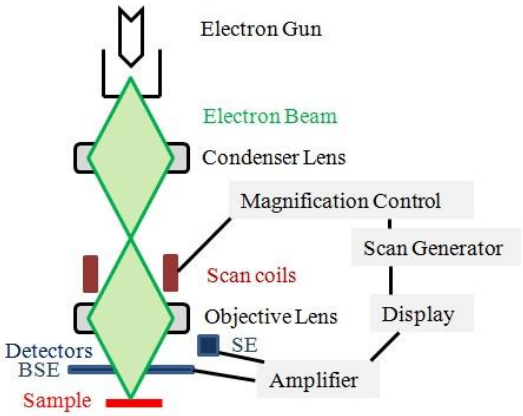

Figure 2.16: Systematic representation of SEM.

2.4.3 X-ray diffraction (XRD)

X-ray diffraction (XRD) is a non-destructive analytical technique used to reveal crystallographic information of polymer materials. The scheme is shown in **Figure 2.17**. The X-rays are generated by X-ray tube and pass through a monochromator to produce an X-ray beam at a specific wavelength, which is illuminated towards the polymer substrate. By using a Siemens D5000 diffractometer using CuKα1 (0.15 nm) radiation X-ray diffraction (XRD) patterns were recorded. When the X-rays strike the polymer substrate, diffraction occurs only for Bragg angles. Consequently, only for certain angles of the incident X-rays, a diffracted X-ray beam can be detected.

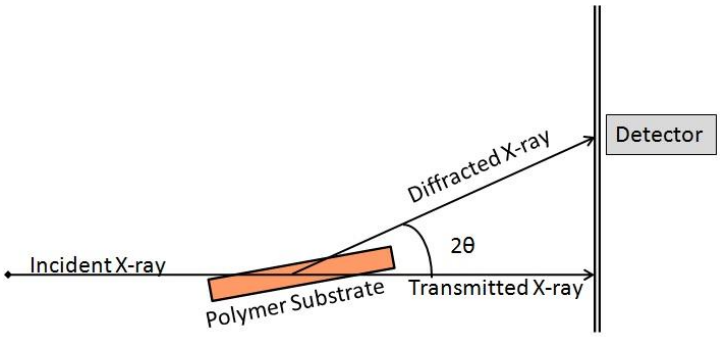

Figure 2.17: Schema X-ray diffraction technique.

2.5 Deposition techniques

2.5.1 Spin coating

The spin coating technique is a laboratory standard technique for producing thin polymer films for optical devices. This coating technique was used over 30 years in the semiconductor industry. Spin coating technique yields highly reproducible films with high structural uniformity.[30, 31]

In the process of spin coating, a polymer solution is dropped on to a horizontal rotating substrate. The substrate is tight held by vacuum which is located in the center of the substrate holder. The motor shaft drives the substrate holder with an initial acceleration and speed, finally reaching to the given input acceleration and speed. During this process the acceleration rate and speed can be adjusted at different time intervals. The spincoating technique is schematically shown in **Figure 2.18**.[32]

The thickness of the polymer film by spin coating mainly depends on the rotation speed, the solvent viscosity and the concentration of the polymer solution. The spinning time also plays a major role in spin coating technique. The spin coater is assembled in the N_2 glove box.

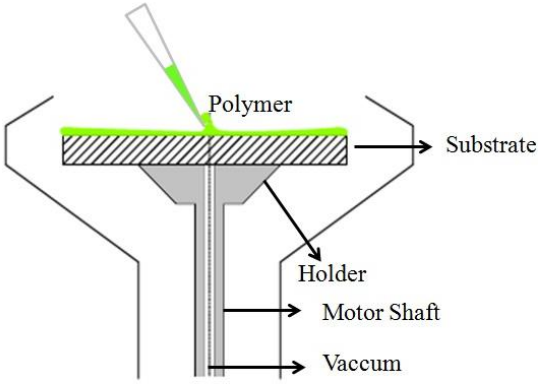

Figure 2.18: Schematic representation of spin coating technique.[32]

2.5.2 Spray coating

Spray coating is a commonly used technique in different sectors like medical, automotive, electronics, food processing etc. for large scale surface depositions The deposition of polymer thin films was demonstrated by using a commercially available hand airbrush[33-36] and high uniform thin layers were produced. There is a novel spray coater also available on the market which is used for the deposition of thin layers.[37]

Spray coating of polymer thin films with a commercially available airbrush has raised some issues regarding the control of film thickness and roughness.[38] Interestingly, surface roughness of the polymer thin film as an active layer produced by spray coating in solar cells did not affect the device performances[38]. In case of OLEDs, the surface roughness should be reduced and morphology is to be well defined in order to avoid electrical short circuits caused by topographical spikes.[39, 40]

The typical spray coating process is shown in **Figure 2.19**.[31] The polymer films are produced in a sequential process. Microscopic droplets from the polymer solution (from the sink) are carried by the aerosol nozzle to the substrate. The aerosol is formed by a continuous flow of inert gas. This gas scatters with the polymer solution into microscopic droplets inside the airbrush. When these droplets reach the substrate the solvent evaporates and starts creating a thin film. There are some limitations: if the droplets are not dried or too wet during the deposition process, the gas pressure will blow

aside the formed layer disturbing the creation of a polymer thin film on the susbstrate. On the other hand, if the droplets dry too early before reaching the substrate, film formation will be inhibited. These limitations can be overcome by heating the substrate during deposition depending on the solvent used for the polymer solution, by controlling the distance between the nozzle and the substrate, by controlling or varying the spray time interval for a better film formation for desired thickness and by adjusting the droplet size and flow rate.

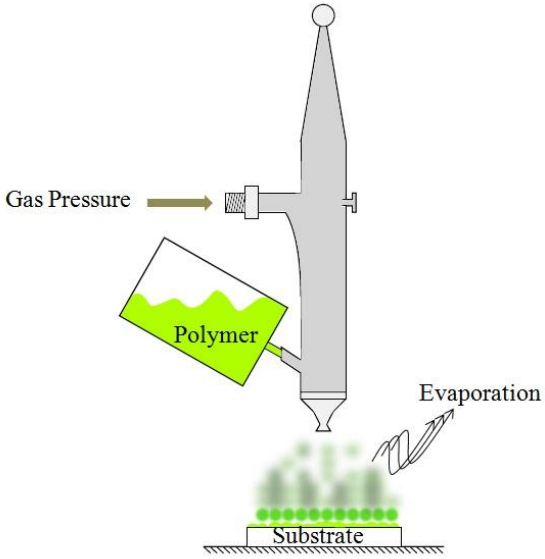

Figure 2.19: Typical spray coating process used in this work.[31]

2.5.3 Deposition of small molecules

The vacuum sublimation/evaporation of small molecules is an alternative approach for deposition of photoactive/hole transporting layers. First opto-electrical device (OLED) material deposited by evaporation was investigated by Tang and his coworker.[41] The main advantage of evaporated small-molecule-based devices is that the active layer can consist of various layers with different functional materials, which can lead towards efficient devices.[42] With evaporation, oxidation of the materials can be prevented during and after the layer preparation. Moreover, the active layer and metal contacts can be evaporated in a single session. In this work for vacuum evaporation of small molecules for pores filling into nano-oxide electrodes was performed. The metallo-organic small molecule copper phthalocyanine (CuPc) was vacuum sublimated.

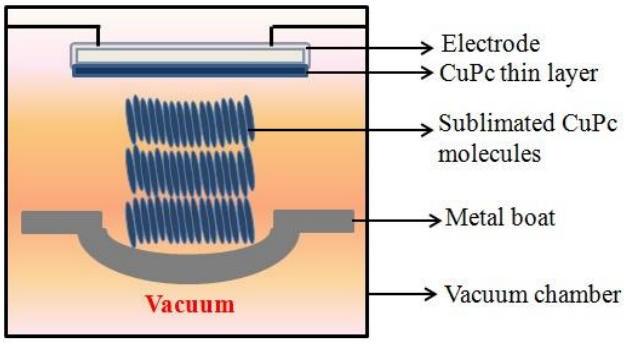

Figure 2.20: Schematic representation of evaporation/vacuum sublimation used for deposition of CuPc.

The schematic of the evaporation/vacuum sublimation of CuPc is shown in **Figure 2.20**. In the vacuum chamber, under high vacuum, the current is supplied to the boat/crucible which generates the heat. Due to this, the CuPc powder on the boat sublimates. The boat/crucible is made up from molybdenum. The sublimated CuPc molecules form a thin layer above the electrode with a certain thickness. The complete process takes place in a N_2 glove box.

2.6 References

1 G. Porter, Proc. Roy. Soc. A 200 (1950) 284.
2 C. Goh, S.R. Scully, M.D. McGehee, J. Appl. Phys. 101 (2007) 114503.
3 L. Goris, A. Poruba, L. Hodákova, M. Vaneček, K. Haenen, M. Nesládek, P. Wagner, D. Vanderzande, L. De Schepper, J. V. Manca, Appl. Phys. Lett. 88 (2006) 052113.
4 M. Vaněček, A. Poruba, Thin Solid Films. 515 (2007) 7499.
5 K. Vandewal, L. Goris, I. Haeldermans, M. Nesládek, K. Haenen, P. Wagner, J. V. Manca, Thin Solid Films. 516 (2008) 7135.
6 M. Vaněček, A. Poruba, Appl. Phys. Lett. 80 (2002) 719.
7 P. R. Griffiths, J. A. deHaseth, Fourier Transform Infrared Spectroscopy, Wiley, New York, 1986.
8 A. J. Mozer, Charge Transport and Recombination in Bulk Heterojunction Plastic Solar Cells. PhD Thesis-ULinz/LIOS, 2004.
9 A. Pivrikas, Charge Transport and Recombination in Bulk-Heterojunction Solar Cells. PhD Thesis-Åbo Akademi University, 2006.
10 L.M. Andersson, Electronic Transport in Polymeric Solar Cells and Transistors. PhD Thesis-Linköping University, 2007.
11 B. C. O'Regan, K. Bakker, J. Kroeze, H. Smit, P. Sommeling, J. R. Durrant, J. Phys. Chem. B. 110 (2006) 17155.
12 X. Wang, S. Karanjit, L. Zhang, H. Fong, Q. Qiao, Z. Zhu, App. Phys. Lett. 98 (2011) 082114.
13 C. G. Shuttle, B. O'Regan, A. M. Ballantyne, J. Nelson, D. D. C. Bradley, J. R. Durrant, Phys. Rev. B. 78 (2008) 113201.
14 C. G. Shuttle, B. O'Regan, A. M. Ballantyne, J. Nelson, D. D. C. Bradley, J. De Mello, J. R. Durrant, Appl. Phys. Lett. 92 (2008) 093311.
15 C. G. Shuttle, R. Hamilton, B. C. O'Regan, J. Nelson, J. R. Durrant, PNAS. 107 (2010) 16448.
16 L. Meies, Handbook of Analytical Chemistry. Ed. McGraw-Hill, New York, 1963. Unpaged. Illus.
17 D. Kahng, M. M. Atalla, IRE Solid-State Devices Research Conference, Carnegie Institute of Technology, Pittsburgh, PA 1960.
18 G. Horowitz, Adv. Mater. 10 (1998) 365.
19 H. Koezuka, A. Tsumura, T. Ando, Synth. Met. 18 (1987) 699.
20 M. Morana, P. Koers, C. Waldauf, M. Koppe, D. Muehlbacher, P. Denk, M. Scharber, D. Waller, C. Brabec, Adv. Funct. Mater. 17 (2007) 3274.

21 V. D. Mihailetchi, L. J. A. Koster, P. W. M. Blom, C. Melzer, B. de Boer, J. K. J. van Duren, R. A. J. Janssen, Adv. Funct. Mat. 15 (2005) 795.
22 I. V. Severen, M. Breselge, S. Fourier, P.r Adriaensens, J. Manca, L. Lutsen, T. J. Cleij, D. Vanderzande, Macromol. Chem. Phys. 208 (2007) 196.
23 A. Gadisa, W. D. Oosterbaan, K. Vandewal, J-C. Bolsée, S. Bertho, J. D'Haen, L. Lutsen, D. Vanderzande, J. V. Manca, Adv. Funct. Mater. 19 (2009) 3300.
24 D. Moses, R. Schmechel, A. J. Heeger, Synth. Met. 139 (2003) 807.
25 M. Chandross, S. Mazumdar, S. Jeglinski, X. Wei, Z. V. Vardeny, E. W. Kwock, T. M. Miller, Phys. Rev. B. 50 (1994) 14702.
26 P. da C. Gomes, E. M. Conwell, Phys. Rev. B. 48 (1993) 1993.
27 J.-L. Brédas, J. Cornil, A. J. Heeger, Adv. Mater. 8 (1996) 447.
28 G. D. Scholes, G. Rumbles, Nat. Mater. 5 (2006) 683.
29 P. Stallinga, Electrical Characterization of Organic Electronic Materials and Devices. Wiley (2009) ISBN: 978-0-470-75009-4.
30 F. C. Krebs, Sol. Energy Mater. Sol. Cells. 93 (2009) 394.
31 O. J. Weiss, Adv. Solid State Phys. 46 (2008) 321.
32 K. Gilissen, Pre-doctoral Thesis-UHasselt/XIOS, 2010.
33 D. Vak, S-S. Kim, J. Jo, S-H. Oh, S-I. Na, J. Kim, D-Y. Kim, Appl. Phys. Let. 91 (2007) 081102.
34 C. Girotto, B. P.Rand, J. Genoe, P. Heremans, Sol. Energy Mater. Sol. Cells. 93 (2009) 454.
35 E. Treossi, A. Liscio, X.Feng, V. Palermo, K.Müllen, P. Samorì. Appl. Phy A: Mater. Sci. Process. 95 (2009) 15.
36 S-I. Na, B-K. Yu, S-S. Kim, D. Vak, T-S. Kim, J-S. Yeo, D-Y. Kim, Sol. Energy Mater. Sol. Cells, 94 (2010) 1333.
37 K. X. Steirer, M. O. Reese, B. L. Rupert, N. Kopidakis, D. C. Olson, R. T. Collins, D. S. Ginley, Sol. Energy Mater. Sol. Cells. 93 (2009) 447.
38 C. Girotto, D. Moia, B. P. Rand, P. Heremans, Adv. Funct. Mater. 21 (2011) 64.
39 S. F. Tedde, J. Kern, T. Sterzl, J. Fürst, P. Lugli, O. Hayden. Nano Lett. 9 (2009) 980.
40 C. N. Hoth, R. Steim, P. Schilinsky, S A. Choulis, S. F. Tedde, O. Hayden, C. J. Brabec, Org. Electron. 10 (2009) 587.
41 C. W. Tang, S. A. VanSlyke, Appl. Phys. Lett. 51 (1987) 913.
N. I. Craciun,J. Wildeman, P. W. M. Blom, J. Phys. Chem. C. 114 (2010) 10559.

Chapter 3: Preparation and Characterization of P3HT Based Organic:Inorganic Hybrid Solar Cell

3.1 Introduction

The conjugated polymer poly-(3-hexylthiophene) (P3HT) is considered as a work horse material in organic solar cells and is also an interesting candidate as a hole transporting/photo-active layer in organic:inorganic hybrid solar cells (HSCs). This is due to its absorption band gap, high charge carrier mobility and high optical absorbance. The HSCs modified with dye sensitizers combined with P3HT had shown a disappointed device efficiency.[1] However; Mor et al.[2] reported HSCs with promising efficiency upto 3.8 % by utilizing TiO_2 nanotube arrays sensitized with a dye. Efficiencies for HSCs (TiO_2/dye/P3HT) have been attained from 2.7 to 3.8 %.[3-5] After the dye sensitization, these devices are treated with different salts and ionic liquids in order to improve mobility of the charge carriers in the TiO_2 layers. Without the treatment of salts and ionic liquids the device performance is 0.04 %, only ionic liquid treatment it is 0.1 %, with only salt incorporation it is 2.45 % and by the combination of salt and ionic liquid, an efficiency of 2.61 % is achieved.[6] The devices are treated with different salt and ionic liquids for attaining the higher efficiencies in literature as discussed elsewhere[3-5].

In this work, one of the aims is to investigate and prepare HSCs without and with dye sensitization, using mesoporous TiO_2 layers and P3HT as photoactive/hole transporting layer. The dye is expected to have several functions. One of the main functions is to passivate the hydrophilic surface of the oxide layer and to help infiltration of the hydrophobic polymer into the porous layer. Also an increase in the light harvesting can be obtained which can sequentially contribute to the increase in efficiency. Some of the dyes used in this work are commercially available (i.e. Black Dye and N719); others are novel synthesized dyes (i.e.TT1, TT3, TT4 and C101) as shown in **Figure 3.1**. The salts and ionic liquids treatment is an irksome task.[3-6] The devices processed in this work were prepared without any further treatment. The optical UV-Vis absorption properties of HSCs with and without dyes sensitization were studied. The HSC devices prepared in this work with C101 dye have reached an efficiency of 1.3 %. With the help of fourier transform photocurrent spectroscopy (FTPS), the photocurrent contribution of the dyes and the external quantum efficiencies (EQE) of the HSCs were studied. The charge transport and charge separation properties were also investigated by using charge extraction by linearly increasing voltage (CELIV), transient photovoltage (TPV) and transient photocurrent (TPC) techniques.

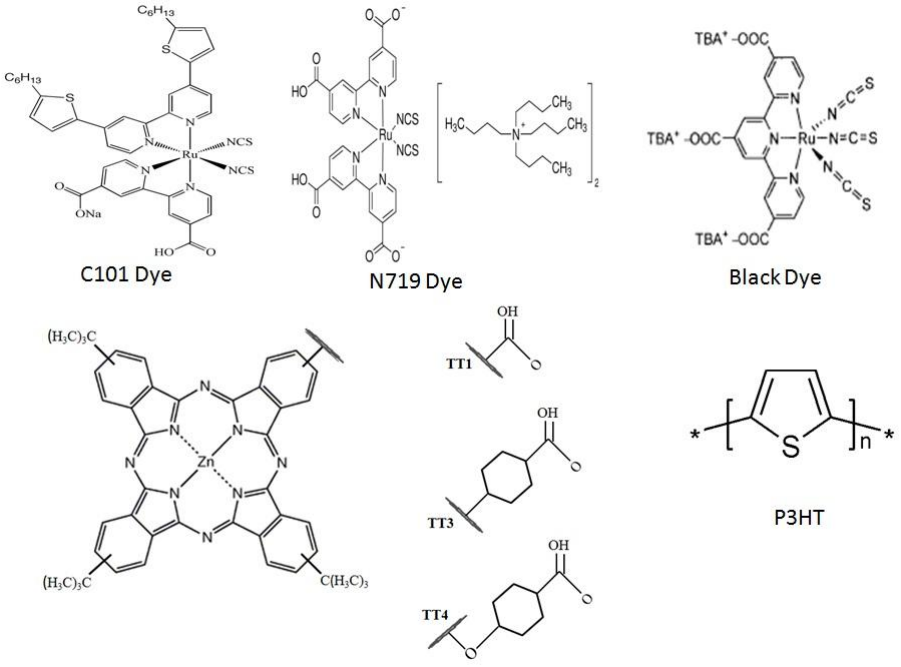

Figure 3.1: Structures of the C101, N719, Black, TT1, TT3 and TT4 dyes respectively and P3HT.

3.2 Materials and device preparation

3.2.1 Materials

The TiO_2 nanoparticles (grain size 37 nm) paste was purchased from Solaronix and regioregular P3HT from Rieke metals. All the dyes (TT1[7], TT3[7], TT4[7], Black dye, N719 and C101) used in this work were supplied from Prof. Palomares-ICIQ lab and the structures are depicted in **Figure 3.1**.

3.2.2 Device Preparation

The fluorine doped tin oxide (FTO) substrates were cleaned (manually rinsing with soap solution, subjected to ultrasonic treatment in soap solution - 30

min, deionized water - 10 min and acetone - 10 min, boiling in isopropanol - 10 min and dried with N_2 flow). Onto clean FTO substrates (15 Ωsq^{-1}) a compact dense TiO_2 layer with a thickness of ~ 70 nm was deposited according to literature [8, 9] by spray coating (explained in chapter 2.5.2) and calcinated at 450 ^{0}C for 20 min. Onto this, a second layer with thickness of ~ 0.9 µm nanocystalline TiO_2 was deposited by spin coating followed by sintering at 450 ^{0}C for 30 min, resulting in mesoporous layers.

Mesoporous TiO_2 electrodes were dye sensitized for 4 h in solutions of $5x10^{-5}$ M TT1, TT3 and TT4 dyes and in $5x10^{-4}$ M of N719, Black Dye and C101 dyes. Ethanol was used a solvent. The dye solutions were prepared according to the procedure from the literature.[7, 10] All the dye solutions contained chenoxycholic acid (10-30 mM) to avoid dye aggregation on the surface of TiO_2 as discussed elsewhere[10] except for N719 dye, as no aggregation is expected. After dye sensitization all the samples were rinsed with ethanol for the removal of unsensitized dye and dried with N_2 flow.

P3HT was incorporated into the mesoporous TiO_2 dye sensitized electrodes in the glove box under inert conditions as similarly discussed in literature[11]. First, the electrodes were dipped in a dilute P3HT solution (3 mg/ml) in chlorobenzene for 30 min. The electrodes were allowed to completely dry and were annealed at 50 ^{0}C for 10 min. A second concentrated solution of P3HT (16 mg/ml) was spin coated (see section 2.5.1) at 2000 RPM onto the P3HT dipped electrodes. These samples were annealed again at 100 ^{0}C for 10 min. Above the P3HT layers a thin layer of PEDOT:PSS at 2000 RPM was spin coated and annealed at 120 ^{0}C for 10 min. Finally, a top contact of 40 - 50 nm gold was evaporated onto the samples at a pressure of 10^{-6} Pa. Each substrate consisted of either active area devices of 3 mm^2 or 5 mm^2. The IV-characteristics were measured with an Oriel solar simulator under AM 1.5 radiation in ambient conditions.

3.3 Results and discussions

3.3.1 Device structure

The HSC device geometry is shown in **Figure 3.2**.

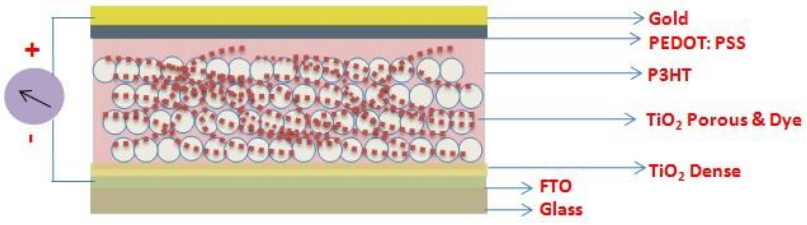

Figure 3.2 : Device geometry of organic:inorganic HSC.

3.3.2 UV-Vis absorption measurements

The UV-Vis absorption spectra of the prepared TiO_2/dye combinations: TiO_2/TT1, TiO_2/TT3, TiO_2/TT4, TiO_2/Black Dye, TiO_2/N719 and TiO_2/C101 are shown in **Figure 3.3**. The black dye, N719 and C101 show broad absorption in the UV-Vis region due to the typical metal-to-ligand charge transfer (MLCT) observed for Ru complex dyes.[12] The TT1, TT3 and TT4 dyes showed an absorption peak at 700 nm. The broadened absorption window in the near-IR region is due to the phthalocyanine Q-band.

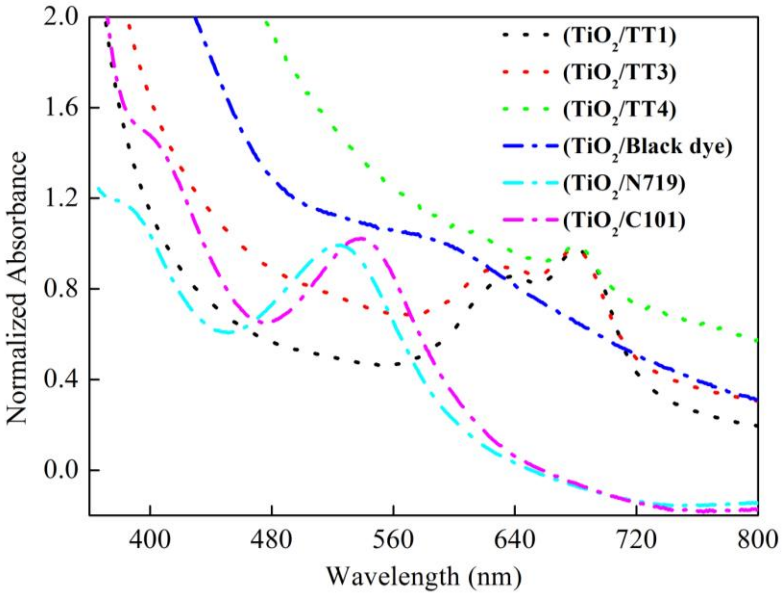

Figure 3.3: Absorption spectra of the dye sensitized TiO_2 layers on glass.

The absorbance spectra for Ru complex dyes N719, Black Dye and C101 in combination with P3HT are shown in **Figure 3.4**. The P3HT had a narrow band at 570 nm. All the Ru complex dyes showed a broad absorbance around 570 nm. The minor contribution of dyes to the absorbance was due to low absorption extintcion coefficients when compared to P3HT. The dye sensitized mesoporous TiO_2 layers can also effect the amount of P3HT into the samples. When C101 dye is used as sensitizer, the amount of P3HT in the porous electrode could be high and might be due to the orientation of the thiophene-functionalized pyridine ligands of C101 dye[13], away from the TiO_2 surface. As a result hydrophobic P3HT side chains interact with the TiO_2/C101 dye surface allowing for the infiltration into the pores of the TiO_2 film. Black dye shows the opposite effect, with less P3HT infiltration into TiO_2 films. This can be due to the anchoring of dye terpyridine ligands near to TiO_2 surface resulting in the orientation of polar groups away from the surface. The N719 dye has little impact on the amount of P3HT infiltration into the TiO_2 layer. The time for sensitization of dyes was 4 h. Beyond this sensitisation time a minor impact in absorption with P3HT was observed.

The absorbance spectra for Zinc phthalocyanine dyes TT1, TT3 and TT4 with P3HT are also depicted in **Figure 3.4**. The contribution of each

phthalocyanine dye was observed at 680 nm, in addition to the P3HT band at 550 nm. It was surprising that inspite of high conjugation and high absorption extincion coefficient of phthalocyanine dyes, the absorption contribution of TT1, TT3 and TT4 dyes was low compared to P3HT. Further studies are required to understand the interaction between the dyes and the polymer.

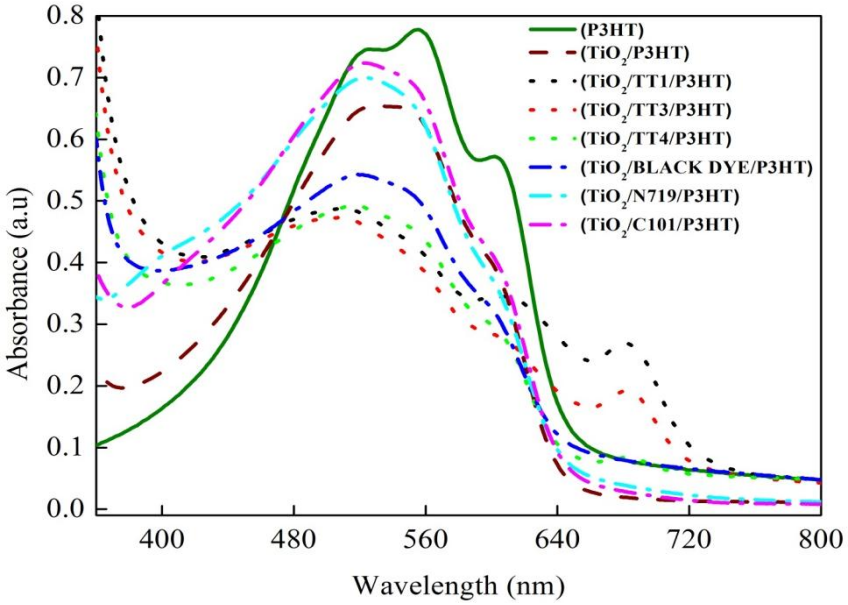

Figure 3.4: Absorption spectra of dyes sensitized TiO_2 electrodes with/without incorporation of P3HT and only P3HT on a glass susbstrate.

3.3.3 IV-characterizations

The IV-charaterization of the HSCs are summarized in **Table 3.1** and shown in **Figure 3.5**.

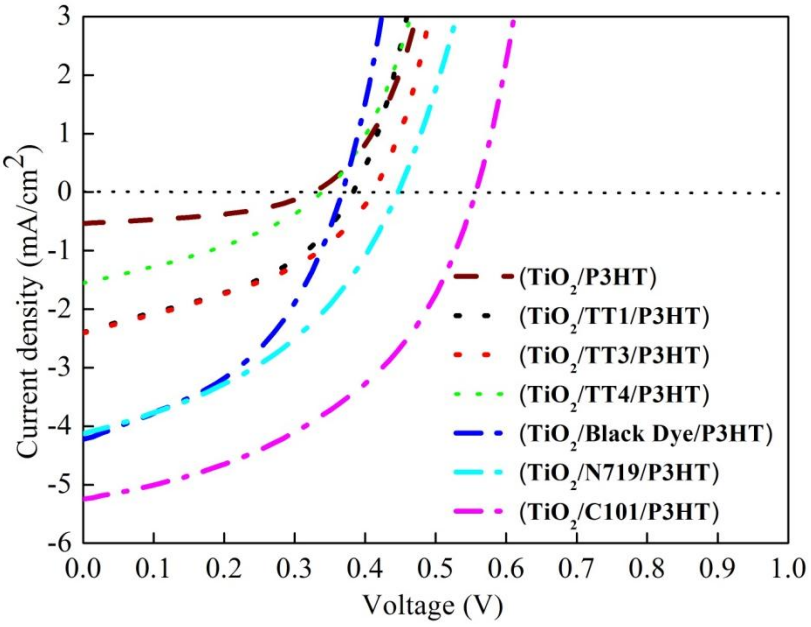

Figure 3.5: IV-curves of HSC devices without and with dyes.

Table 3.1: Summarized data of open circuit voltage (V_{oc}), short-circuit current (J_{sc}), fill factor FF (%) and efficiency η (%)

Device Structure	V_{oc} (V)	J_{sc} (mA/cm^2)	FF (%)	η (%)
TiO_2/P3HT	0.336	0.66	41	0.08
TiO_2/TT1/P3HT	0.38	2.38	41	0.37
TiO_2/TT3/P3HT	0.41	2.79	33	0.37
TiO_2/TT4/P3HT	0.34	1.6	33	0.18
TiO_2/Black Dye/P3HT	0.36	4.2	41	0.62
TiO_2/N719/P3HT	0.45	4.2	41	0.77
TiO_2/C101/P3HT	0.56	5.3	45	1.3

*on FTO with gold top contact.

The dye sensitizated TiO_2 layer in hybrid devices with incorporation of P3HT has improved the device performances when compared to a control device TiO_2/P3HT without dye.

The increased efficiency of devices with incorparation of red absorbing dyes (TT1, TT3 and TT4) can be due to the improved light harvesting towards near-IR region, when compared to control device. Also with Ru complex sensitizied TiO_2 layers there was an improvement in device performance. The improvement in devices prepared from Black dye and N719 dye with P3HT, can be related to more excitons harvesting capability. There can be better interaction between P3HT and dye incorporated TiO_2 layers. The C101/TiO_2 layer with P3HT showed improved device performance and reached a power conversion efficiency of 1.3 %. This can be ascribed to the improved inflitration of P3HT into the pores as discussed in the absorption measurements. Even tough the molecular structure variations of N719 dye and C101 dye are small the effect of device performance was relatively large. This shows that the tenuous changes in molecular structure can have a big effect on the device performances.

3.3.4 External quantum efficiency measurements (EQE)

Photocurrent external quantum efficiency (EQE) is an important characteristic that defines the number of electrons produced per incident photon in solar cells. The relative EQE of the HSC devices were investigated by FTPS (described under section 2.3.1). The obtained EQE spectra for devices made without dye (control device TiO_2/P3HT) and with dyes are shown in **Figure 3.6**.

From the EQE spectra, the contribution of photocurrent from the materials (dye or P3HT or both) can be clearly observed. The EQE peak value of the control device was at 2.3 eV (~ 540 nm). The EQE spectra of the devices obtained from TT1, TT3, TT4, Black Dye, N719 and C101 dyes with P3HT exhibited a very similar profile like the control device with maximum peak at 2.3 eV. The EQE spectral signal increased. An important result is the observation of a widening of the absorption window (from 1.9 eV to 1.6 eV) due to the dyes in HSCs compared to the control device in these EQE spectra. Relatively high EQE was obtained from the TiO_2/C101/P3HT device.

The devices prepared by using red absorbing dyes TT1, TT3, TT4 showed an additional peak at lower energy of 1.8 eV (~ 675 nm) and improved the light harvesting towards the near-IR region. Furthermore, the photocurrent contribution was low when compared to the TiO_2/C101/P3HT device and higher than the control sample, with these dyes in HSCs.

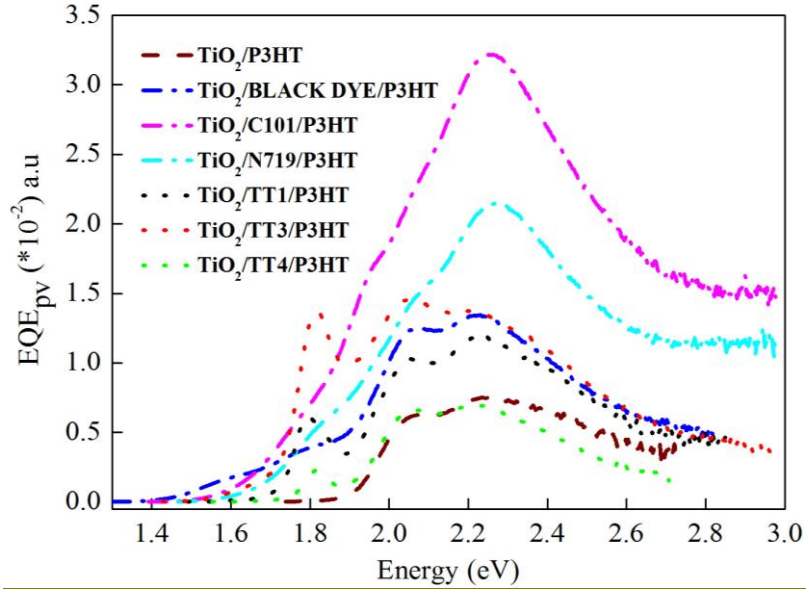

Figure 3.6: EQE spectra of devices wihout and with dyes measured by FTPS on HSCs.

From the **Figure 3.6** EQE maxima of the HSC devices obtained by FTPS followed the trend as below:

TiO_2/C101/P3HT < TiO_2/N719/P3HT < TiO_2/TT3/P3HT < TiO_2/Black dye/P3HT < TiO_2/TT1/P3HT < TiO_2/TT4/P3HT < TiO_2/P3HT.

This highest EQE of TiO_2/C101/P3HT was intriguing compared to TiO_2/N719/P3HT devices as C101 and N719 dyes have similar band gap levels and expected to conduct equally. This unusual performance might lie with the arrangement of alkyl side chains of these dyes resulting in reduced charge carrier recombination. In addition to this, a higher photocurrent was also observed for TiO_2/C101/P3HT device depending on the ability to accept the electrons by TiO_2 from P3HT. This also explains the higher charge separation behavior when TiO_2 layers are modified with dyes when compared to no dye in HSCs. From the work of C. Goh et al.[14], a model for an

increased photocurrent has been derived for the interface modifier with and without dyes onto TiO_2 layers in a scheme of TiO_2/P3HT device and also well explained with PL quenching measurements. On the basis of these EQE measurements TiO_2/P3HT, TiO_2/N719/P3HT and TiO_2/C101/P3HT devices were further selected to study the charge transport and separation properties.

3.3.5 Charge extraction by linearly increasing voltage measurements (CELIV)

Charge carrier mobility was measured by using Charge extraction by linearly increasing voltage (CELIV) on TiO_2/P3HT, TiO_2/N719/P3HT and TiO_2/C101/P3HT devices. A linearly increasing voltage pulse was applied to the device to extract the charge carriers during these measurements. In this way the mobility of the fastest charge carrier can be obtained according to equation 2.5.

Some of the CELIV transient curves obtained are shown in **Figure 3.7**. The transients were obtained as a function of applied voltage pulses at fixed ramp delay time of 15 µs with fixed light intensity. Photo-CELIV curves as a function of delay time are shown in **Figure 3.7**. The t_{max} becomes shorter with increasing voltage, indicating that the charge carrier velocity depends on the voltage.

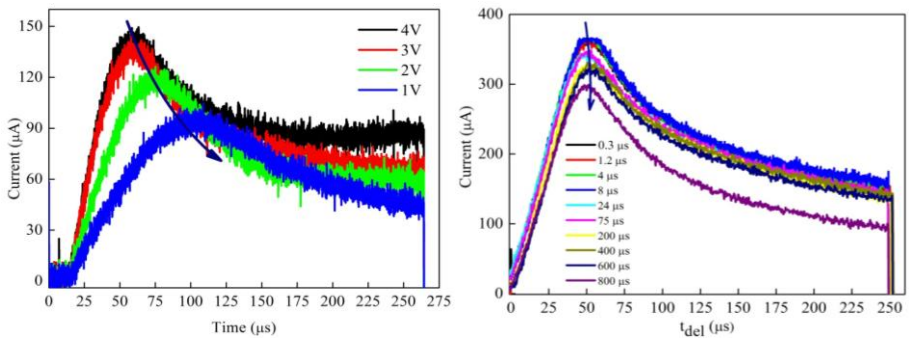

a b

Figure 3.7: CELIV transients of TiO_2/P3HT device (a) as a function of applied voltage (V) pulses at fixed ramp delay time of 15 µs at fixed light intensity and (b) photo-CELIV curves as a function of delay times.

From the **Figure 3.8** (inset) shows the CELIV mobility versus square root of electric field (electric field is given as At_{max}/d where, A is linearly increasing voltage pulse with the slope $A = U_{max}/t_{pulse}$, here U_{max} is the maximum voltage of triangle pulse and t_{pulse} is the pulse duration, t_{max} is the maximum time and d is the thickness) on TiO_2/P3HT, TiO_2/N719/P3HT and TiO_2/C101/P3HT devices. The obtained mobility of the fastest charge carriers is in the order of 10^{-3} - 10^{-4} cm^2 /V s which might be hole mobility, as P3HT hole mobility is in the range of 10^{-3} - 10^{-4} cm^2 /V s[15]. On the first observation in **Figure 3.8** it can be noticed that the higher charge carrier mobility (obtained by photo-CELIV measuements) in TiO_2/C101/P3HT devices is in the order of $\sim10^{-3}$ cm^2/Vs, when compared to TiO_2/N791/P3HT and TiO_2/P3HT devices ($\sim10^{-4}$ cm^2/Vs). The charge carrier mobility was nearly constant with an increasing delay time of TiO_2/P3HT, TiO_2/N719/P3HT and TiO_2/C101/P3HT devices. The higher charge carrier mobility in TiO_2/C101/P3HT device is due to the higher hole-transfer yield[16, 17] from C101 dye to P3HT. Hole-transfer yield is related to the P3HT covering the TiO_2/C101 mesoporous electrode and to the quantity of pore fill fraction[16, 17]. The investigations are still ongoing on the quantity of filling of pores by P3HT in the TiO_2/C101 layer. The device with C101 dye has a factor of 10 times higher charge carrier mobility compared to other devices. A higher photocurrent and hole mobility obtained from TiO_2/C101/P3HT device was clearly observed.

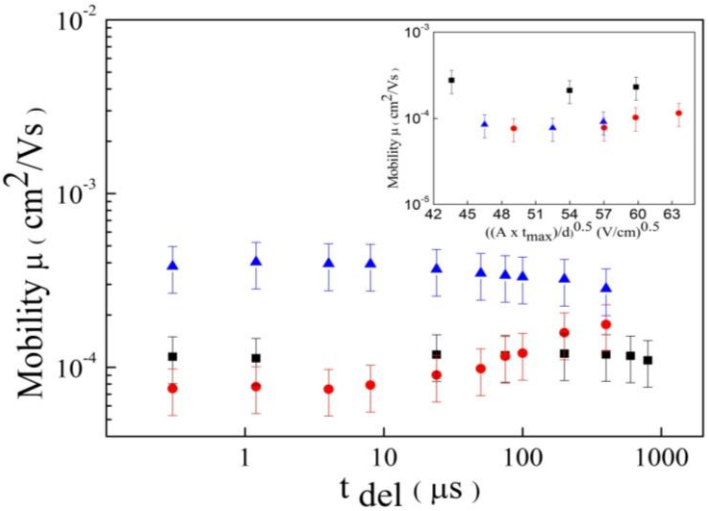

Figure 3.8: CELIV mobility as a function of different delay time of TiO_2/P3HT (solid square), TiO_2/N719/P3HT (solid circle) and TiO_2/C101/P3HT (solid triangle) and (inset) as a function of electric field of TiO_2/P3HT (solid square), TiO_2/N719/P3HT (solid circle) and TiO_2/C101/P3HT (solid triangle).

3.3.6 Transient photovoltage and transient photocurrent measurements (TPV and TPC)

In order to extract the life-time of charge carriers and the recombination rate of HSCs at different V_{oc}'s, the TPV technique was used. The typical TPV decay curves at different light intensities for measuring the life-time of the charge carriers and the recombination are shown in **Figure 3.9**.

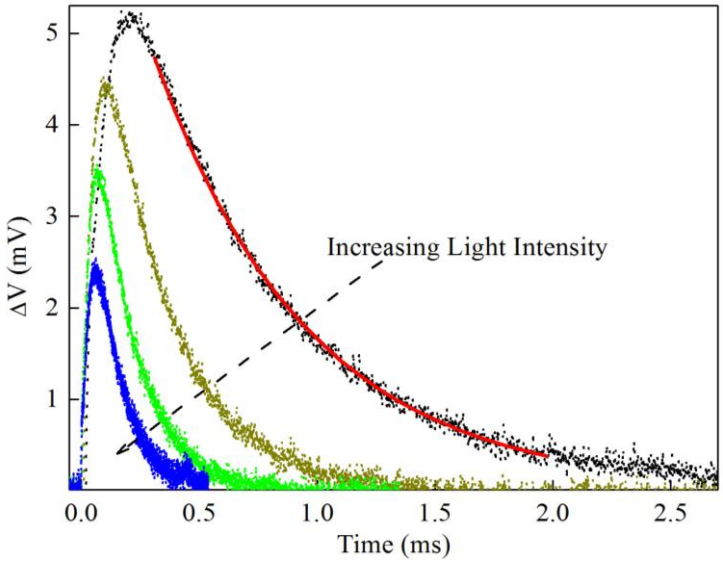

Figure 3.9: Representation of the transient photo voltage decay curves measured at 0.1 – 1.5 different sun light intensities for a TiO_2/C101/P3HT device. The red line represents the fit to extract the life-time of the charge carriers by using equation 2.8.

The TPV decays become faster and smaller as depicted in **Figure 3.9** with the increase of light bias. This is due to the decrease of charge carriers life-time. Higher light intensities create more charge carriers and at the same time a higher rate of recombination. The TPV life time of charge carrier measurements in the devices TiO_2/P3HT, TiO_2/N719/P3HT and TiO_2/C101/P3HT was obtained by fitting with the equation 2.8. They exhibit a life time of ~ 10 ms at lower light intensity and ~ 1 ms at higher light

intensity. The life-times are shown in **Figure 3.10a**. This typically long life time is ascribed to the trapping-detrapping of electrons in the TiO_2 film.[18-20]

The bimolecular recombination coefficient (β) and charge carrier density (n) were calculated by using the equations 2.9 and 2.10. The graphs have been plotted for different V_{oc}'s versus (n) as shown in **Figure 3.10a**. Higher values of (n) for TiO_2/C101/P3HT compared to TiO_2/N719/P3HT devices were observed. From the EQE spectra (**Figure 3.6**) the separation of charge carriers in TiO_2/P3HT was difficult as explained under section 3.3.4. Due to this, the (n) in TiO_2/P3HT at different voltages was too low to be determine with our setup.

Figure 3.10b depicts (n) versus (β) plot of TiO_2/N719/P3HT and TiO_2/C101/P3HT by deriving the (β) values from **Figure 3.10a** and using equation 2.10. The bimolecular recombination coefficient (β) increases with increasing in charge carrier density (n) of TiO_2/N719/P3HT and TiO_2/C101/P3HT devices. The TiO_2/C101/P3HT device exhibits a (β) of 10^{-15} cm^3/s at lower light intensity and 10^{-18} cm^3/s at higher light intensity, whereas TiO_2/N719/P3HT device exhibits a (β) of 10^{-15} cm^3/s at lower light intensity and 10^{-16} cm^3/s at higher light intensity. The rate of recombination was reduced by using C101 dye to 100 times compare to N719 dye at higher light intensities. The decrease of (β) of TiO_2/C101/P3HT device may be due to the better charge carrier separation occurring at the TiO_2/C101 dye in HSCs. The better charge carrier separations are possibly related to the better infiltration of P3HT into the pores of TiO_2/C101 electrode. Further investigations by TAS and X-ray photoelectron spectroscopy are underway to resolve the reasons behind these observations.

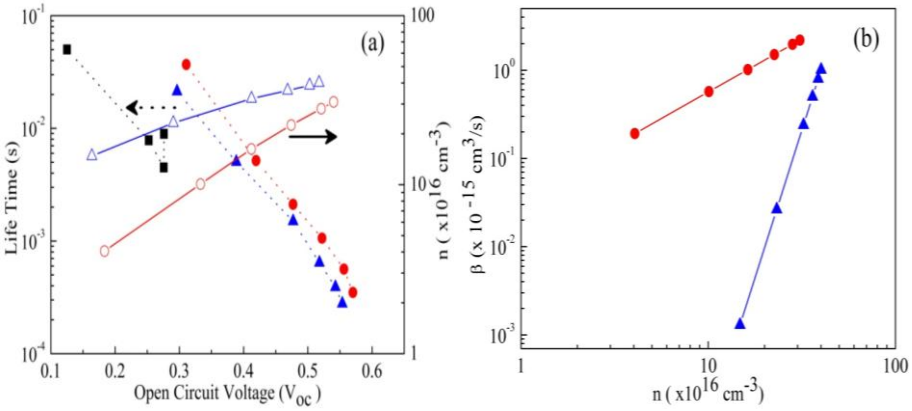

Figure 3.10: (a) Charge carrier life-time and extracted charge carriers density measured at different V_{oc}'s of TiO_2/P3HT (**s**:solid square), TiO_2/N719/P3HT (**s**:solid circle, **n**: open circle) and TiO_2/C101/P3HT (**s**:solid triangle, **n**: open triangle), where **s** is the charge carrier life-time and **n** is the charge carrier density and (b) bimolecular recombination coefficient as a function of extracted charge carrier density of TiO_2/N719/P3HT (solid circle) and TiO_2/C101/P3HT (solid triangle).

3.4 Conclusions

P3HT based HSC devices with and without dye were prepared and characterized. The optical properties were studied by using UV-Vis absorption measurements on the dye sensitized TiO_2 layers with and without (control sample) P3HT. The C101 dye was seen to be the best dye for helping P3HT infiltration into the pores of TiO_2 film. In all the cases with dye treatment, there was improved device performance compared to the control device. The HSC device made with the dye C101 obtained the highest efficiency i.e. 1.3 %. With the help of FTPS the photocurrent contribution of dyes and relative EQE were determined. Devices made with the red absorbing dyes all show improved light harvesting and with C101 dye the highest EQE was obtained. The charge separation and charge transport properties were investigated on TiO_2/P3HT, TiO_2/N719/P3HT and TiO_2/C101/P3HT HSCs by using CELIV, TPV and TPC techniques. From CELIV measurements the highest charge carrier mobility was observed for TiO_2/C101/P3HT. This might be related to the better P3HT infiltration with C101 dye treatment resulting in higher hole-transfer yield from C101 dye to P3HT. The C101 dye based HSC device exhibited long charge carrier life-time, higher charge carrier generation and lower recombination rate compared to N719 dye based HSC device which was drawn from TPV and TPC measurements. These investigations help in order to understand cell processes governing efficiencies for improvement of future devices with novel dyes and other forms of metal-oxides (nanorods, nanotubes, nanofibers etc.). In particular to optimize and enhance the device performance of HSCs after dye sensitization of TiO_2 layers with different treatments are required.

3.5 References

1 C-W. Hsu, L. Wang, W-F. Su, J. Coll. Int. Sci . 329 (2009) 182.
2 G. K. Mor, S. Kim, M. Paulose, O. K. Varghese, K. Shankar, J. Basham, C. A. Grimes, Nano Lett. 12 (2009) 4250.
3 K. Jiang, K. Manseki, Y. Yu, N. Masaki, K. Suzuki, Y. Song, S. Yanagida, Adv. Funct. Mater. 19 (2009) 2481.
4 R. Zhu, C. Jiang, B. Liu, S. Ramakrishna, Adv. Mater. 21 (2008) 994.
5 W. Zhang, R.Zhu, F. Li, Q. Wang, B. Liu, J. Phys. Chem. C 115 (2011) 7038.
6 W. Zhang, R. Zhu, B. Liu, S.Ramakrishna, Appl. Energy. 90 (2012) 305.
7 J. J. Cid, M. García-Iglesias, J. H. Yum, A. Forneli, J. Albero, E. Martínez-Ferrero, P. Vázquez, M. Grätzel, M. K. Nazeeruddin, E. Palomares, T. Torres, Chem. Eur. J. 15 (2009) 5130.
8 S. Ito, P. Chen, P. Comte, M. K. Nazeeruddin, P. Liska, P. Péchy, M. Grätzel, Prog. Photovolt Res. Appl. 15 (2007) 603.
9 L. Schmidt-Mende, M. Grätzel, Thin Solid Films 500 (2006) 296.
10 A. Reynal, E. Palomares, Energy Environ. Sci. 3 (2010) 805.
11 H. J. Lee, H. C. Leventis, S. A. Haque, T. Torres, M. Grätzel, M. K. Nazeeruddin, J. Pow. Sour. 196 (2011) 596.
12 M. K. Nazeeruddin, R. Humphry-Baker, P. Liska, M. Grätzel, J. Phys. Chem. B. 34 (2003) 8981.
13 F. Gao, Y. Wang, D. Shi, J. Zhang, M. Wang, X. Jing, R. Humphry-Baker, P. Wang, S. M. Zakeeruddin, M. Grätzel, J. Am. Chem. Soc. 130 (2008) 10720.
14 C. Goh, S.R. Scully, M.D. McGehee, J. Appl. Phys. 101 (2007) 114503.
15 W. D. Oosterbaan, J. C. Bolsée, A. Gadisa, V. Vrindts, S .Bertho, J. D'Haen, T. J. Cleij, L. Lutsen, C. R. McNeill, L. Thomsen, J. V. Manca, D. Vanderzande, Adv. Funct. Mater. 20 (2010) 792.
16 W. Zhang, Y. Cheng, X. Yin, B. Liu, Macromol. Chem. Phys. 212 (2010) 15.
17 J. Melas-Kyriazi, I.-K. Ding, A. Marchioro, A. Punzi, B. E. Hardin, G. F. Burkhard, N. Tétreault, M. Grätzel, J.-E. Moser, M. D. McGehee, Adv. Energy. Mater. 1 (2011) 407.
18 J. Nelson, Phys. Rev. B. 59 (1999) 15374.
19 J. Nelson, S. A. Haque, D. R. Klug, J. R. Durrant, Phys. Rev. B. 63 (2001) 205321.
20 H. J. Snaith, L. Schmidt-Mende, Adv. Mater. 19 (2007) 3187.

Chapter 4: Preparation and Characterization of CuPc Based Organic:Inorganic Hybrid Solar Cells

Gopala Krishna T.V.V, .J. N. Clifford, D. Spoltore, F. Piersimoni, E. Palomares and J. V. Manca, 'Optoelectrical and photophysical properties of solid-state dye sensitized solar cells using evaporated CuPc layers as hole transporting material', *Submitted. 2011*.

4.1 Introduction

Phthalocyanine materials are widely used as dyes for printing and painting industries, as catalysts and in medical applications.[1] They are often employed in nano-structured photovoltaic devices such as in DSSCs due to their high stability, high molar extinction coefficients and excellent electron donating capabilities.[2-4] Indeed they have been used extensively as electron-donors in heterojunction solid-state solar cells with electron-accepting materials such as fullerenes.[5, 6] As a first approach; cell assembly, cell efficiency, optical and photo-physical characterizations of hybrid solar cells were performed. In these hybrid solar cells, where a layer of CuPc is evaporated onto without and with dye sensitized TiO_2 layers. CuPc replaces the liquid electrolyte and is used as a photo active/hole transporting layer. Evaporation as a means of depositing the hole transporting material (HTM) is attractive as it is possible to prepare many samples at once under inert conditions and also to evaporate the metal contact immediately thereafter. Charge separation in these devices was investigated using Charge Extractions by Linearly Increasing Voltage (CELIV) and Transient Absorption Spectroscopy (TAS) techniques in order to understand the cell processes that govern the efficiency.

4.2 Materials and device preparation

4.2.1 Materials

Glass/FTO electrodes (15 Ω/sq) and 37 nm TiO_2 paste were purchased from Solaronix. The chemical structures of C101 dye and CuPc (95% purity) are shown in **Figure 4.1 a** and **b** and were supplied from the Prof. Palomares-ICIQ lab (ICIQ-Spain) and Alfa Aesar respectively.

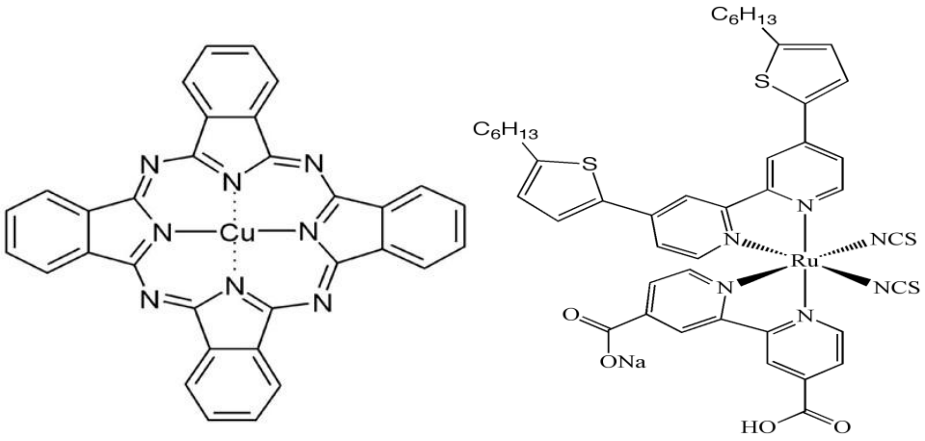

a b

Figure 4.1: Chemical structures of CuPc (a) and C101 dye (b).

4.2.2 Device preparation

The fluorine doped tin oxide (FTO) substrates were cleaned (manually rinsing with soap solution, subjected to ultrasonic treatment in soap solution - 30 min, deionized water - 10 min and acetone - 10 min, boiling in isopropanol - 10 min and dried with N_2 flow). Onto clean FTO substrates (15 Ωsq^{-1}) a dense TiO_2 blocking layer of ~ 100 nm was deposited deposited by spin coating from a mixture of titanium isopropoxide: ethanol: acetic acid (ratio of 1: 9: 0.1)[9] at 7000 rpm followed by sintering at 450 ^{0}C for 30 min. Onto this, a layer of ~ 800 nm mesoporous TiO_2 was spin coated followed by sintering at 450 ^{0}C for 30 min. The TiO_2 electrode was then dye sensitized for 4 h in 0.5 mM solution of C101 in ethanol containing 10 mM chenoxycholic acid to avoid the dye aggregations. The CuPc (~ 60 nm) was vacuum sublimated at a pressure of 10^{-7} Pa onto the bare TiO_2 and TiO_2/C101 electrodes. Finally to complete the devices, metal contacts were evaporated consisting of first 5 nm gold followed by 50 nm silver by evaporation through a shadow mask at a pressure of 10^{-6} Pa.

The indium tin oxide (ITO) substrates were cleaned by using the same sample cleaning procedure. These substrates were subjected to UV ozone treatment for 15 minutes and directly transferred into the N_2 glove box. Then a CuPc layer of 140 nm was evaporated onto ITO substrates and the metal contact Al of 50 nm was evaporated. The ITO/CuPc/Al device was used as a hole-only diode to extract the hole mobility by IV-measurements. The active areas of prepared devices are 3 mm^2 or 5 mm^2 and the IV-

characterization of all devices was performed under ambient conditions. Sun light illumination was provided by a LOT Oriel solar simulator with simulated AM1.5 radiation and IV-curves were measured using a programmable Keithley 2400 source meter.

4.3 Results and discussions

4.3.1 Schematic energy levels

The LUMO energy levels of CuPc[11] and C101[12] are aligned as depicted in **Figure 4.2**. As indicated, these levels are sufficient to allow for electron injection into the TiO_2 conduction band from the excited states of both/either species. Furthermore, hole-transfer from the C101 to the CuPc layer is energetically possible. This means that CuPc can act as the hole transporting material between the working electrode (FTO) and the metal contacts (Au/Ag) in these devices. It should be noted that CuPc does not contain any anchoring moiety such as carboxylic acid that allows covalent bonding to the TiO_2 surface.

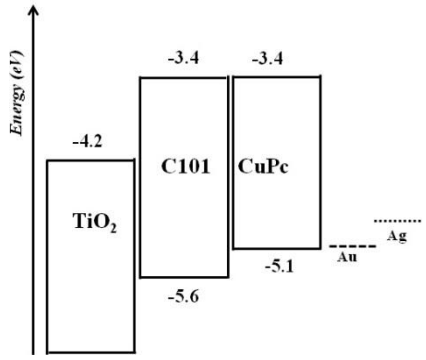

Figure 4.2: Schematic energy levels of the TiO_2/C101/CuPc device.

4.3.2 Scanning electron microscope (SEM)

A SEM (as discussed under section 2.3.1) topographical view of the deposited CuPc film is given in **Figure 4.3**. There it can be observed that, the formed film was homogeneous with small crystal grains with an average diameter of 100 - 160 nm. This value is in good agreement with the literature results.[13, 14] Moreover charge carrier mobility is higher in crystalline materials than in amorphous materials.[14]

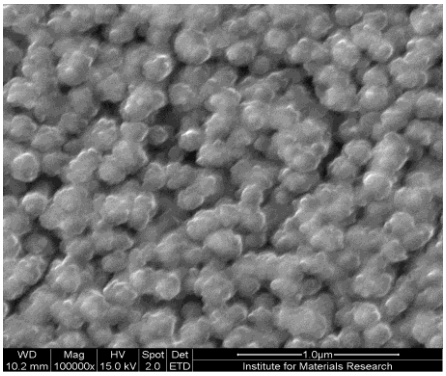

Figure 4.3: Topographical view of deposited CuPc film by SEM.

4.3.3 UV-Vis absorption measurements

The UV-Vis absorption measurements were performed as described in the section 2.1.1. The UV-Vis absorption spectra of films of TiO_2, CuPc, TiO_2/C101, TiO_2/CuPc and TiO_2/C101/CuPc are shown in **Figure 4.4**. Different absorption peaks were observed for CuPc in UV-Vis region. The absorption peak of CuPc at 330 nm is due to the Soret band or B-band of porphyrin molecules. The two absorption peaks in between 600 nm - 800 nm are due to the Q-band of phthalocyanine molecules. This accounts for the blue color of CuPc material.

The C101 dye shows a broad absorption in the UV-visible due to the typical metal-to-ligand charge transfer-MLCT (i.e transfer of electrons from molecular orbits with metal-Ru to TiO_2 with ligand) observed for Ru(II)polypyridyl complexes.[15] Moreover, from the absorption spectra there was a red shift from TiO_2/C101/CuPc compared to TiO_2/C101. The better

anchoring of C101 dye to the surface of mesoporous TiO_2 possibly results in development of better interfacial dipoles[16] in TiO_2/C101/CuPc. The absorption spectrum of TiO_2/C101/CuPc shows clearly the contributions of both dye species.

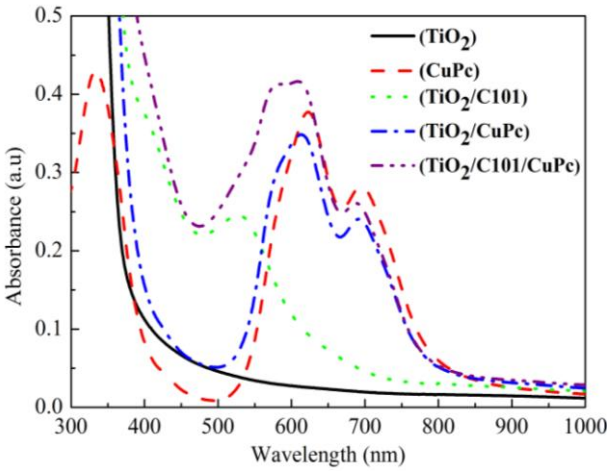

Figure 4.4: The UV-Vis absorption spectra of films of TiO_2 (-), CuPc (- -), TiO_2/C101 (···), TiO_2/CuPc (–·–) and TiO_2/C101/CuPc (-..-).

4.3.4 IV-characteristics

The IV-characteristics of devices containing films of CuPc, TiO_2/CuPc, TiO_2/C101 and TiO_2/C101/CuPc under AM 1.5 illumination are shown in **Table 4.1** and **Figure 4.5 a** and **b** with superiority of the TiO_2/C101/CuPc device was clearly apparent. The TiO_2/C101 device shows the highest photocurrent however the poor fill-factor and voltage (may be due to recombination losses occurring at short circuit).[17]

The CuPc only device measures low photocurrent with poor fill-factor and greater voltage as shown in **Figure 4.5a**, resulting in a much lower efficiency than the TiO_2/C101/CuPc device. The efficiencies of TiO_2/CuPc and TiO_2/C101/CuPc were in line with similar solid-state devices investigated, involving metal-oxides and phthalocyanine films as HTM.[11, 18-21] In this work, the charge transport and charge separation properties at the interfaces are well elaborated. The V_{oc} value obtained for the TiO_2/CuPc device (0.26 V) was greatly inferior to that of the TiO_2/C101/CuPc device (0.7 V). Moreover,

if one considers the HOMO energy of CuPc (-5.1 eV) allows up to 1V V_{oc}, this value is also extremely poor indeed [22] in these hybrid devices.

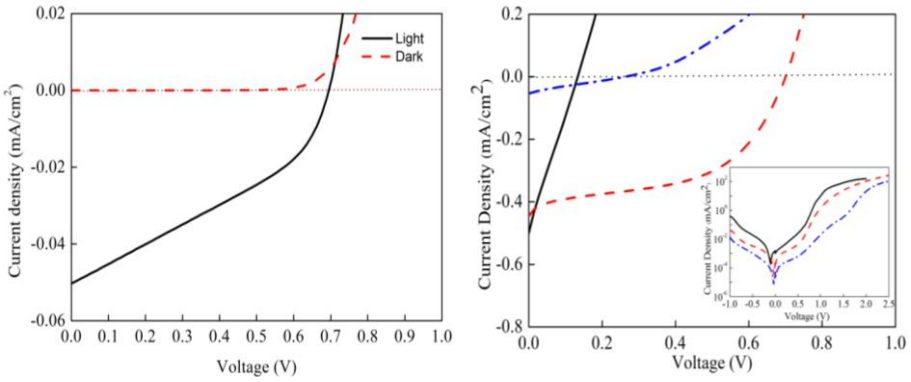

a b

Figure 4.5: (a) IV-measurements of device measured under standard AM 1.5 illumination CuPc (-), in dark (--) and (b) IV-measurements of TiO_2/C101 (—), TiO_2/CuPc (-·-) and TiO_2/C101/CuPc (--) devices illumination (main figure) and in the dark (inset).

Table 4.1: Summarized data of open circuit voltage (V_{oc}), short-circuit current (J_{sc}), fill factor FF (%) and efficiency η (%) of ITO/CuPc/Al, FTO/TiO_2/C101/Au/Ag, FTO/TiO_2/CuPc/Au/Ag and FTO/TiO_2/C101/CuPc/Au/Ag solar cells.

Sample	V_{oc} (V)	J_{sc} (mA/cm^2)	FF (%)	η (%)
CuPc	0.69	0.05	35	0.013
TiO_2/C101	0.13	0.52	23	0.016
TiO_2/CuPc	0.26	0.05	23	0.003
TiO_2/C101/CuPc	0.7	0.44	48	0.15

The TiO_2/C101/CuPc device showed higher photocurrents and a 50-fold enhancement in performance when compared to TiO_2/CuPc device. Clearly the differences in photocurrent and V_{oc} between these devices explain the

huge difference in cell efficiencies recorded for these devices. As mentioned above (UV-Vis absorption), CuPc does not contain any linker group to allow for covalent attachment to the TiO_2 surface. Such an attachment has often been cited[23] in order to achieve strong electronic overlap between the LUMO of the excited dye species and the conduction band of the TiO_2, thus to facilitate efficient electron injection. This could be one reason for the poor photocurrent and V_{oc} observed in the TiO_2/CuPc device. Furthermore the degree to which CuPc penetrates into the pores of the mesoporous TiO_2 electrode might be limited (needs additional investigations).

4.3.5 External quantum efficiency measurements (EQE)

Normalized External Quantum Efficiency (EQE) photocurrent spectra of these devices were also measured by FTPS (discussed in Chapter 2.3.1) on CuPc, TiO_2/C101, TiO_2/CuPc and TiO_2/C101/CuPc and is shown in **Figure 4.6**. The TiO_2/CuPc device clearly shows the contribution of CuPc to the photocurrent with peaks at 1.8 and 2.0 eV corresponding to the absorption maxima of CuPc. The TiO_2/C101 device shows a peak at 2.3 eV corresponding to the absorption maximum of C101. The TiO_2/C101/CuPc photocurrent spectrum clearly resembles that of the spectrum of TiO_2/C101 indicating that in TiO_2/C101/CuPc the main contribution to the photocurrent was measured from C101.

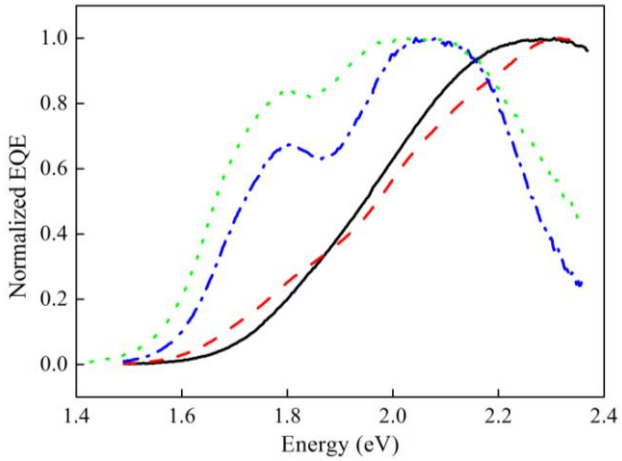

Figure 4.6: Normalized EQE photocurrent spectra of CuPc (…), TiO_2/C101 (—), TiO_2/CuPc (–·–) and TiO_2/C101/CuPc (--) as a function of energy measured by FTPS.

4.3.6 Transient absorption spectroscopy measurements (TAS)

TAS measurements (according to the earlier discussions in chapter 2.1.2) were conducted on TiO_2/C101, TiO_2/CuPc and TiO_2/C101/CuPc samples. In order to investigate the light induced processes occurring at the interfaces. Following the excitation at 530 nm (where C101 mostly absorbs) the resultant transient decay was monitored at 750 nm (**Figure 4.7**) corresponding to the maximum of the C101 cation spectrum of TiO_2/C101/CuPc sample. This decay shows typical stretched exponential kinetics as observed previously in DSSCs [24, 25] with slow milli-second recombination that is typically ascribed to the trapping-detrapping of electrons in the TiO_2 electrode film (i.e. sub-bandgap states to deep in the tail of the density-of-states, to the conduction band).[26, 27] Moreover these kinetics were almost identical to the kinetics recorded for a TiO_2/C101 sample indicating that, evaporation of the CuPc layer does not affect electron injection from C101 into the conduction band of TiO_2 in TiO_2/C101/CuPc. Finally, when TiO_2/CuPc sample was excited at 600 nm no signal was observed over the 600 nm - 900 nm region indicating that either there is negligible electron injection from CuPc into the conduction band of TiO_2 or

that the recombination is too fast to be recorded with our set-up. No signal was observed from CuPc only sample.

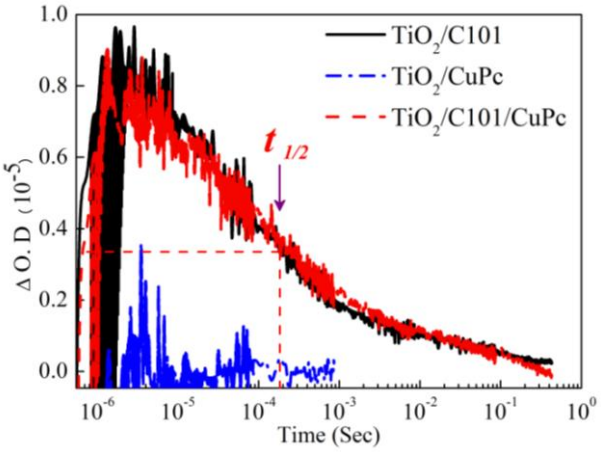

Figure 4.7: TAS kinetics of TiO_2/C101 (black), TiO_2/CuPc (blue) and TiO_2/C101/CuPc (red). TiO_2/C101 and TiO_2/C101/CuPc kinetics were recorded at 750 nm following excitation at 530 nm. TiO_2/CuPc kinetics were recorded at 850 nm following excitation at 600 nm.

4.3.7 Charge extraction by linearly increasing voltage measurements (CELIV)

Based on the observations of CELIV in section 2.3.2, the measurements were performed on TiO_2/C101/CuPc device only. On the other devices the measurements could not be performed, due to the injections of charges in the reverse bias condition. The CELIV curves were recorded as a function of applied voltage pulses at fixed ramp delay time of 15 μs at fixed light intensity and the photo-CELIV curves as a function of delay time are shown in **Figure 4.8**.

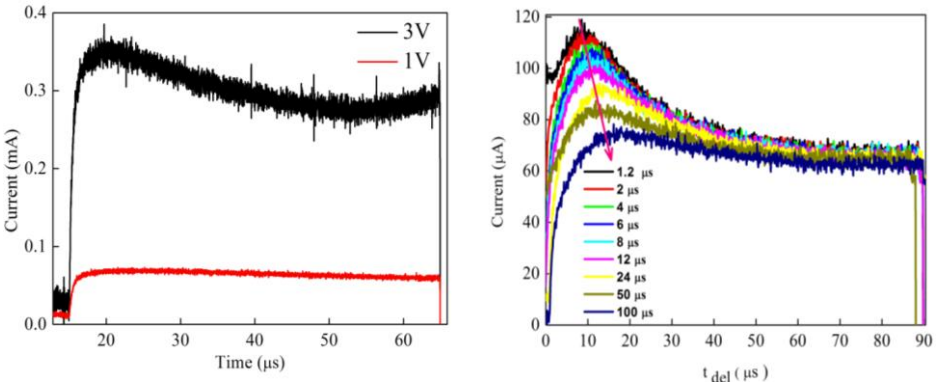

a b

Figure 4.8: CELIV curves of TiO_2/C101/CuPc device (a) as a function of applied voltage (V) pulses at fixed ramp delay time of 15 µs at fixed light intensity and (b) photo-CELIV curves as a function of delay times.

The mobility of the fastest charge carrier can be obtained according to equation 2.5. **Figure 4.9** shows the CELIV mobility versus square root of electric field. The obtained mobility of the fastest charge carriers is in the order of 10^{-4} cm^2/Vs which might be hole mobility, since the CuPc hole mobility is in the order of 10^{-4} cm^2/Vs.[28] From the dark IV-curve of CuPc only device with the SCLC measurements (of equation 2.7), a hole mobility of 2 x 10^{-4} cm^2/Vs was attained and the fitting is shown in **Figure 4.10** (with ε_r 3.6[29] and V_{bi} was ~ 1 V).

From photo-CELIV curves, obtained mobility values were plotted against delay time as shown in **Figure 4.9,** the mobility is decreasing with t_{del} till 20 µs, and remains constant for longer delay time. This can be attributed to energy relaxation of the charge carriers towards the tail states of density of states distribution.[30]

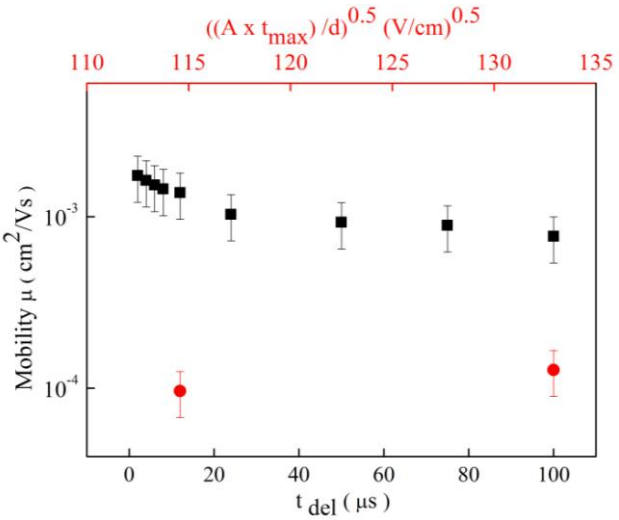

Figure 4.9: photo-CELIV mobility as a function of delay time (■) CELIV mobility as a function of electric field (●).

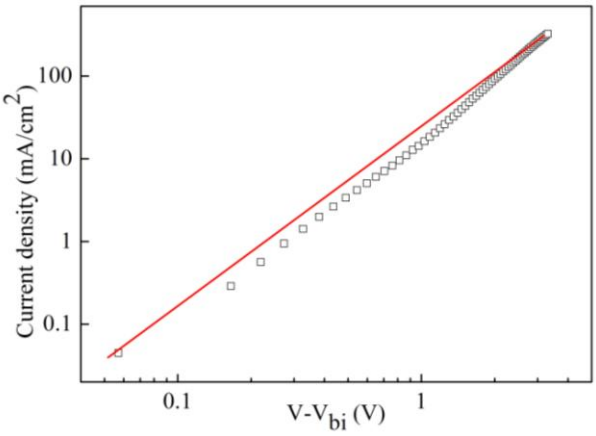

Figure 4.10: The log – log plot of current density (J) – voltage ($V-V_{bi}$) of CuPc only device. Solid lines represent the linear fit used for obtaining the hole mobility of CuPc.

The **Figure 4.12** depicts the recombination where the number of charge carriers extracted versus the delay time is plotted.

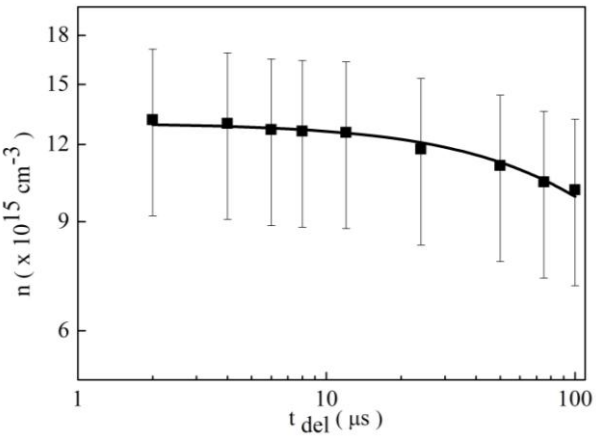

Figure 4.12: The concentration of the extracted charge carriers as function of delay time with solid line fitting for life time of charge carriers in TiO_2/C101/CuPc devices.

The recombination kinetics was studied using a bimolecular recombination formula equation 2.6. The exponential bimolecular decay dynamics was observed by TAS. This is attributed to an exponential tail decay of sub-bandgap localised ('trap') states in TiO_2.[26, 31] The solid line in inset of **Figure 4.12** was a fit of equation 2.6 with n_0=1.3 x 10^{16} cm^{-3} and β=2.37 x 10^{-13} cm^3/s were achieved (β is the bimolecular recombination coefficient (cm^3/s), n_0 and n(t) are the initial density and density of photo-generated charge carriers (cm^{-3})). The bimolecular life-time t_β (s) of the long lived charge carriers was obtained by using equation 2.7 and to be 0.32 ms.

As can be observed from the TiO_2/C101/CuPc TAS kinetics in **Figure 4.7** the $t_{1/2}$[12] (time taken for 50 % of the signal to decay due to the presence of relatively long-lived photoexcited charges) was around 0.18 ms. TAS measurements are sensitive to optically active long-lived charge carriers, whereas CELIV detects the mobile optically excited charge carriers extracted by the electrical field and are therefore complimentary techniques to study the life-time of the long-lived charge carriers. The long life-time and slow bimolecular recombinations of the charge carriers are observed in these devices. This is due to slow electron transport through the nanocrystalline mesoporous TiO_2 layers as explained elsewhere.[32]

4.4 Conclusions

In this chapter an alternative assembly of hybrid solar cells has been demonstrated incorporating CuPc as the hole transporting material which was deposited via evaporation. Sensitization of the TiO_2 film with the dye C101 improves cell efficiency when compared to devices where no dye in present. The device that does not contain C101 shows much lower photocurrent and V_{oc} indicating that CuPc has either negligible electron injection into TiO_2 or the recombination process was extremely fast. Charge separation and charge mobility measurements using the CELIV and TAS techniques show rather long lifetimes that were ascribed to the trapping/detrapping of electrons in the nanocrystalline mesoporous TiO_2 layer. It is believed that efficiency of this type of solid-state hybrid device can be optimized through the use of different metal-oxide nanostructures such as nanorods that may lead to improved infiltration by the HTM and needs future investigations.

4.5 References

1 P. Gregory, J. Porphyrins Phthalocyanines, 4 (2000) 432.
2 J. J. Cid, M. García-Iglesias, J. H. Yum, A. Forneli, J. Albero, E. Martínez-Ferrero, P. Vázquez, M. Grätzel, M. K. Nazeeruddin, E. Palomares, T. Torres, Chem. Eur. J. 15 (2009) 5130.
3 H. J. Lee, H. C. Leventis, S. A. Haque, T. Torres, M. Gräztel, M. K. Nazeeruddin, J. Pow. Sour. 196 (2011) 596.
4 M. Ouyang, R. Bai, L. Yang, Q. Chen, Y. Han, M. Wang, Y. Yang, H. Chen, J. Phys. Chem. C. 112 (2008) 2343.
5 J. G. Xue, S. Uchida, B. P. Rand, S. R. Forrest, Appl. Phys. Lett. 84 (2004) 3013.
6 Z. R. Hong, B. Maennig, R. Lessmann, M. Pfeiffer, K. Leo, Appl. Phys. Lett. 90 (2007) 203505.
7 C. W. Tang, S. A. VanSlyke, Appl. Phys. Lett. 51 (1987) 913.
8 N. I. Craciun, J. Wildeman, P. W. M. Blom, J. Phys. Chem. C. 114 (2010) 10559.
9 Q. Fan, B. McQuillin, D. D. C. Bradley, S. Whitelegg, A. B. Seddon, Chem. Phys. Lett. 347 (2001) 325.
10 G. Porter, Proc. Roy. Soc. A 200 (1950) 284.
11 M. Thelakkat, C. Schmitz, H.-W. Schmidt, Adv. Mater, 14 (2002) 577.
12 A. Reynal, E. Palomares, Energy Environ. Sci. 3 (2010) 805.
13 F. Yakuphanoglu, M. Caglar, Y.Caglar, S. Ilican, Synth Metal. 160 (2010) 1520.
14 J. Puigdollers, C. Voz, M. Fonrodona, S. Cheylan, M. Stella, J. Andreu, M. Vetter, R. Alcubilla, J. Non-Cryst. Solids. 352 (2006) 1778.
15 F. Gao, Y. Wang, D. Shi, J. Zhang, M. Wang, X. Jing, R. Humphry-Baker, P. Wang, S. M. Zakeeruddin, M. Grätzel, J. Am. Chem. Soc. 130 (2008) 10720.
16 R. Zhu, C. Jiang, B. Liu, S. Ramakrishna, Adv. Mater.21 (2008) 994.
17 B. C. O'Regan, F. Lenzmann, J. Phys. Chem. B. 108 (2004) 4342.
18 R. Signerski, G Jarosz, B. Koscielska, J. Non-Cryst. Solids. 355 (2009) 1405
19 R. Signerski, B. Koscielska, Opt. Mat. 27 (2005) 1480.
20 J. Takada, H. Awaji, M. Koshioka, W. A. Nevin, M. lmanishi, N. Fukada, J. Appl. Phys. 75 (1994) 4055.
21 J. Takada, H. Awaji, M. Koshioka, A. Nakajima, W. A. Nevin, Appl. Phys. Lett. 61 (1992) 2184.
22 M. C. Scharber, D. Mühlbacher, M. Koppe, P. Denk, C. Waldauf, A. J. Heeger, C. J. Brabec, Adv. Mater. 18 (2006) 789.

23 K. Kalyanasundaram, M. Grätzel, J. Chem. Sci. 109 (1997) 447.
24 H. Chen, H. Huang, X. Huang, J. N. Clifford, A. Forneli, E. Palomares, X. Zheng, L. Zheng, X. Wang, P. Shen, B. Zhao, S. Tan, J. Phys. Chem. C. 114 (2010) 3280.
25 J. N. Clifford, E. Palomares, M. K. Nazeeruddin, M. Gräztel, J. Nelson, X. Li, N. J. Long, J. R. Durrant, J. Am.Chem. Soc. 126 (2004) 5225.
26 J. Nelson, Phys. Rev. B. 59 (1999) 15374.
27 J. Nelson, S A. Haque, D. R. Klug, J. R. Durrant, Phys. Rev. B. 63 (2001) 205321.
28 B. P. Rand, J. Xue, S. Uchida, S. R. Forrest, J. Appl. Phys. 98 (2005) 124902.
29 R. F. Salzman, J. Xue, B. P. Rand, A. Alexander, M. E. Thompson, S. R. Forrest, Org. Electron. 6 (2005) 242.
30 A. Mozer, N. S. Sariciftci, A. Pivrikas, R. Oesterbacka, G. Juska, L. Brassat, H. Baessler, Phys. Rev. B. 71 (2005) 035214.
31 C. G. Shuttle, B. C. O Regan, A. M. Ballantyne, J. Nelson, D. D. C. Bradley, J. De Mello, J. R. Durrant, Appl. Phys. Lett. 92 (2008) 093311.
32 H. J. Snaith, L. Schmidt-Mende, Adv. Mater. 19 (2007) 3187.

Chapter 5: Towards the Development of Eco-Friendly Hybrid Solar Cells

Gopala Krishna V.V. Thalluri, J-C. Bolsée, A. Gadisa, M. Parchine, T.Boonen, J. D'Haen, A. E. Boyukbayram, J. Vandenbergh, T. J. Cleij, L. Lutsen, D. Vanderzande and J. V. Manca, 'Opto-electrical and morphological characterization of water soluble conjugated polymers for eco-friendly hybrid solar cells', *Solar Energy Materials & Solar Cells 95 (2011) 3262–3268.*

VIEW FROM... 2010 MRS SPRING MEETING

Solar cells stimulate discussion

One point that was raised time after time, particularly by those attending presentations, was that solar technology should be truly green. The environmental impact of various solar cell materials and manufacturing processes came under fi re during several talks. Some presentations specifi cally tackled this issue, including that of *Gopala Krishna* and Jean-Christophe Bolsée, both from Hasselt University in Belgium, who described recent progress in 'green' Grätzel solar cells with water-soluble constituents. Grätzel cells, also known as dye-sensitized solar cells, have attracted interest due to their potentially low cost when compared with standard silicon solar cells. However, many researchers are concerned about the environmental impact of the particular liquid electrolytes being used in such cells. Several talks at the meeting focused on all-solid-state designs, in which the liquid electrolyte is replaced with a solid-state hole transport material such as polythiophenes. However, polythiophenes are soluble in organic solvents, which make them toxic and not environmental friendly, according to the Belgian researchers. "To overcome this, we introduced water-soluble polythiophenes as hole conductors and photo-active layers for solar cells," Bolsée told **Nature Photonics**. "Solid-state polymer/ TiO_2 nanocrystalline hybrid solar cells deliver efficiencies of up to 0.7%, which is five times higher than the efficiencies achieved so far using water-soluble polythiophenes."

5.1 Introduction

The main drawback of organic solvents and liquid electrolytes for the production of hybrid solar cells (HSCs) or dye sensitized solar cells (DSCCs) is that they are not environmental friendly. To overcome these drawbacks, eco-friendly processed materials are required. Towards eco-friendly processing and development, water soluble conjugated polymers (WSCPs) showed great interest for many applications such as highly sensitive biological[1] or chemical sensors[2], opto-electronic devices[3], (multilayer) organic light emitting diodes (OLEDs)[4], polymer light-emitting electrochemical cells (PLECs)[5] and in photovoltaic devices [6,7] e.g.: [Poly 3-(sodium-6-hexanoate) thiophene-2, 5-diyl] (P3SHT) and [(Sodium (poly [2-(3-thienyl)-ethoxy-4-butyl sulfonate)] (PTEBS). The hydrophilic side chains in WSCPs consist of charged groups such as phosphonates, sulfonates, carboxylates[8] or ammonium salts or neutral groups such as hydroxyl and ethylene glycol moieties rendering the polymer water soluble[9]. In exploratory work on WSCP based HSC power conversion efficiencies around 0.14 %[6], [7] have been reported. On the other hand, WSCP (PTEBS) used with C_{60} fullerene in a bilayer configuration has resulted in an efficiency of 0.4%[10]. In polymer based solar cells, four subsequent layers (ZnO/Active layer/PEDOT: PSS/Ag) have been processed from aqueous solution above ITO (indium tin oxide) and have reached up to 0.7 % efficiency.[11, 12] Layer-by-layer assembly and electrochemical deposition was so far not successful for aqueous based active layer materials.[13]

In this work, it is essential to understand the opto-electrical and morphological properties of the water soluble conjugated polymer derivative called poly[3-(potassium-m-alkanoate)thiophene-2,5-diyl]s (P3PmTs) see **Figure 5.1**, with m the number of carbon atoms in the alkanoate side chain varying from 4 to 7. This study is done to evaluate their suitability for solar cell applications. Optical characterization by UV-Vis absorption spectroscopy, estimation of band edge and band gap values by cyclic voltammetry, determination of relative dielectric permittivity by using impedance spectroscopy, charge transport properties by Field Effect Transistor (FET) and Space Charge Limited Current (SCLC) measurements techniques are used to evaluate these material properties. By comparing the obtained opto-electrical properties of the various P3PmTs, the highest hole mobility was found in P3PmT (m = 6) and this has been selected, for further investigation as a photo-active donor in HSCs. The preparation of eco-friendly HSCs by replacing dye and liquid electrolyte with P3P6T taking the role of dye and liquid electrolyte was demonstrated. For this preparation, a simple alternative new processing method has been introduced for the uniform

deposition of a thin hole transporting layer (HTL) consisting of two steps (spin coating + spray coating) above the mesoporous TiO_2 layer. This two step process resulted in a significant improvement of the photovoltaic conversion efficiency attaining 0.7 %, for this type of solar cells. Morphological and topographical studies by using transmission electron microscope (TEM), X-ray diffraction (XRD) and scanning electron microscope (SEM) are presented and discussed for these P3PmTs, TiO_2 layers and of HSC device are also presented and discussed.

5.2 Materials and device preparation

5.2.1 Materials

In **Table 5.1** and **Figure 5.1** the chemical properties and chemical structures of different P3PmTs studied in this work are listed. The P3PmTs were purchased from Rieke Metals. The polymer solutions were prepared with 15 mg/ml (1.5%) concentration in deionized water. These polymer solutions were stirred for 2 h at 80 °C, cooled to room temperature and filtered with 0.45 µm filters. The P3PmTs are bearing a hydrophilic potassium carboxylate salt side chain which makes them to be water-soluble.

Different grain sized nanoxide titania pastes (grain sizes of 13 nm, 20 nm and 37 nm) were supplied from Solaronix. The exact chemical composition of these pastes is not available. According to the provided data, titiania nanoparticles are dispersed in ethanol and water with organic binders that prevent aggregation.

Table 5.1: Summarized chemical properties of different P3PmTs.

Polymer	P3PmT (m–alkyl chain lengths)	Regio-regularitiy (%)*	Molecular weight (kg/mol)*
poly[3–(potassium–4–butanoate)thiophene–2,5–diyl]	P3P4T	90–93	~18
Poly[3–(potassium–5–pentanoate)thiophene–2,5diyl]	P3P5T	90–93	~20
Poly[3–(potassium–6–hexanoate)thiophene–2,5–diyl]	P3P6T	90–93	~26
Poly[3–(potassium–7–heptanoate)thiophene–2,5–diyl]	P3P7T	90–93	~76

*Data has been provided by the Rieke metals

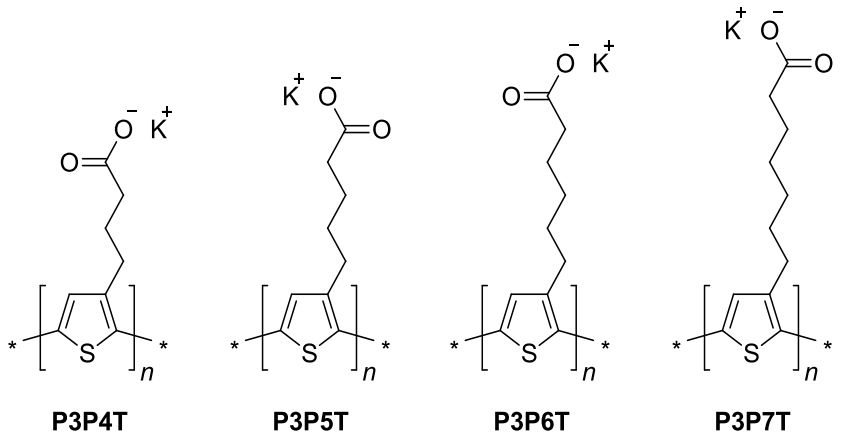

Figure 5.1: Chemical structures of the P3PmTs.

5.2.2 Device preparation

The P3P*m*Ts and TiO_2 layers were spin coated on glass, transparent conductive oxides (TCO) and FET substrates which were cleaned. The substrates were cleaned (manually rinsing with soap solution, subjected to ultrasonic treatment in soap solution - 30 min, deionized water - 10 min and acetone - 10 min, boiling in isopropanol - 10 min and dried with N_2 flow). The cleaned FET samples were subjected to UV Ozone treatment for 15 min and directly transferred into N_2 glove box. The P3PmTs film were deposited by spin coating at 1000 RPM and annealed at 120 ^{0}C for 10 min. The cleaned ITO substrates were subjected to UV Ozone treatment for 15 min. Then water soluble P3PmTs were deposited by using an alternative new processing method, i.e. spin coating + spray coating followed by drying according to the plastic petri dishes[13] for 4 h after each step of deposition. The P3PmTs are not capable of producing thick films by multilayer processing from the same solvent; this is due to the effect that each layer dissolves with previous layer. In order to increase the thickness it is thus not possible to apply a subsequent spin coating step. This encouraged us for the investigation of this alternative new processing method. Spin coating at 600 RPM for 1 min and annealing at 120 $^{\circ}$C for 15 min, result in the formation of very thin P3PmTs layer. A second layer of polymer was spray coated uniformly on top of the spin coated polymer layer. A commercially available airbrush (SEALEY AB931) pressurized by N_2 gas was used for this spray coating. The standard settings include gas pressure of ≥ 10 psi and an airbrush nozzle-substrate distance of ~ 8 cm. The polymer was uniformly sprayed on the complete sample by moving the airbrush across the substrate (25 mm x 25 mm) and again the samples were annealed at 120 $^{\circ}$C for 15 min. An intermediate layer of PEDOT: PSS (BAYER EL grade) solution in isopropanol[14] was spin coated above the layers of P3PmTs forming 80 nm – 100 nm layers to avoid the devices from shunting before the evaporation of top contact. Finally, 50 nm of Ag anode contact was evaporated through a shadow mask at a pressure of 10^{-6} bar with active areas of 3 mm^2 and 5 mm^2. The IV-measurements were performed under dark conditions by using Keithley a 2400 source meter in glove box. To check reproducibility, several devices were prepared and measured. The impedance was measured with a HP 4294A Precision Impedance Analyzer (V_{dc} is 0 V and V_{ac} is 50 mV). The thickness of these P3PmT spin coated layers ranged from 50 nm to 70 nm. The P3P*m*Ts were deposited on glass substrates by an alternative new processing method (where the thickness of films ranged from 100 nm to 120 nm. The highest hole mobility P3P6T was deposited above different grain sized TiO_2 layers. All the above samples were annealed at 120 ^{0}C for 15 min.

Glass/FTO electrodes (15 Ω/sq) were supplied from Solaronix. The active layers of the HSC devices were formed with water soluble conjugated polymer and TiO_2 layers between the two electrodes. On to the cleaned bottom glass/FTO electrodes a dense TiO_2 layer ~ 110 nm (measured by Dektak surface profilometer) is spin coated from a mixture of titanium isopropoxide: ethanol: acetic acid (ratio of 1: 9: 0.1) at 7000 rpm according to the litrature[15]. Then the samples were sintered at 450 ^{0}C for 30 min. On these substrates mesoporous TiO_2 layers with different grain sizes (13, 20 and 37 nm) were spin coated at 7000 rpm for 1 min and sintered at 450 ^{0}C for 30 min (thicknesses ~ 700 nm – 850 nm). Solid polymer P3P6T films above the TiO_2 layers were formed by using the alternative new procedure (spin coating + spray coating) and annealed at 120 ^{0}C for 15 min. Finally 50 nm of silver (Ag) anode contact was evaporated through a shadow mask at a pressure of 10^{-6} bar. On each substrate active areas of 3mm^2 and 5mm^2 were IV-characterized. All the photovoltaic devices presented here were processed in air. The sunlight was generated from an Oriel Sol3A Class AAA Solar Simulator giving AM1.5 (100 mW/cm^2) radiation. Current–voltage (IV) characteristics of solar cells were measured by using a programmable Keithley 2400 source meter.

5.3 Results and discussions

5.3.1 Contact angle measurements

A schematic configuration of the complete HSC device studied in this work is presented in **Figure 5.2a**. Upon light absorption, photo-generated charge carriers are created in the WSCP as depicted in **Figure 5.2b**.The excited electrons are injected into the titania (TiO_2) and collected at the bottom fluorine doped tin oxide (FTO) electrode. The holes diffuse through the WSCP network into the silver electrode. The low efficiencies reported elsewhere [6, 7] could be due to inefficient and incomplete hopping charge transport, limited polymer infiltration into the mesoporous TiO_2 layer and deposition of thick hole transporting layers to avoid shunting of the devices. In these hybrid devices the metal-oxides are hydrophilic in nature and conventional conjugated polymers are hydrophobic, which can cause compatibility problems at the donor-acceptor material interface. To overcome this issue, hydrophilic WSCPs are introduced for having a better anchoring[16] with metal-oxides. The P3P*m*Ts wetting with mesoporous TiO_2 layer is due to its

hydrophilicity with a measured contact angle < 27 ° which is shown in **Figure 5.3**.

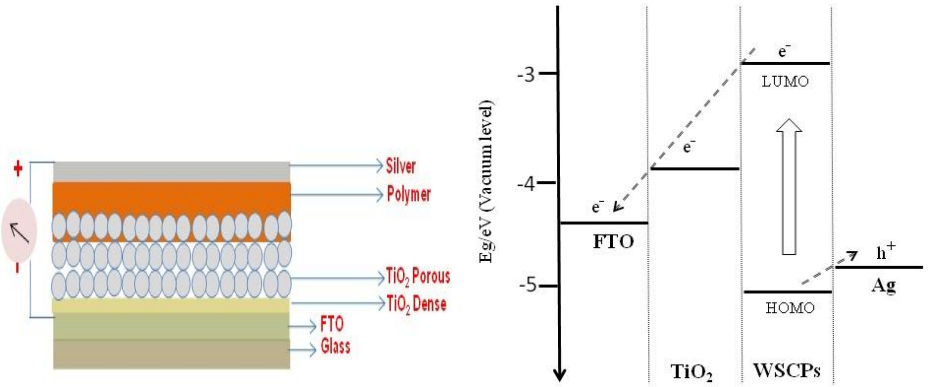

a b

Figure 5.2: (a) Schematic configuration of the eco-friendly hybrid polymer/TiO_2 solar cell, (b) Energy structure diagram of the WSCPs/TiO_2 hybrid solar cells.

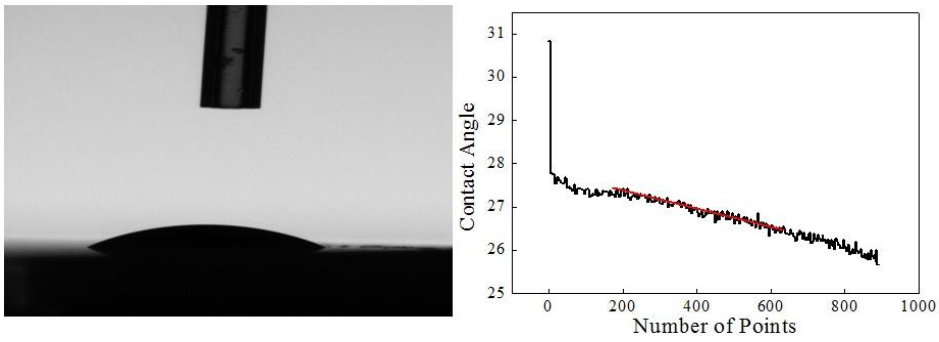

a b

Figure 5.3: (a) wetting behavior and contact angle between P3P*m*Ts and mesoporous TiO_2 and (b) the solid red line represents point's average for determination of final contact angle.

To optimize the hybrid solar cells, optical and electrical properties of different P3PmTs serve as a base. These properties are discussed systematically in the following section.

5.3.2 UV-Vis absorption on P3PmTs

The UV-Vis absorption spectra of different P3P*m*T spin coated films are shown in **Figure 5.4a**. From these measurements it can be concluded that P3P*m*Ts have high absorption in the visible region, the absolute absorption of WSCP is measured elsewhere[17]. They have an optical band gap which around to be (1.92±0.1) eV, estimated from the onset of the low energy absorption band. The P3P*m*T films deposited by the new processing method (spin coating + spray coating) showed similar absorption spectra like the spin coated P3P*m*Ts as depicted in **Figure 5.4b**. In **Figure 5.4a**, π-π^* absorption band signals are clearly present for all P3P*m*Ts showing sign of less pronounced vibrational structures, when compared to P3HT film (inset of **Figure 5.4a**). This is probably due to the more disorder in the P3P*m*Ts backbone compared to P3HT, where a similar effect of crystalline order with increasing side-chain length was found for poly (3-alkylthiophene)s. [18-20]

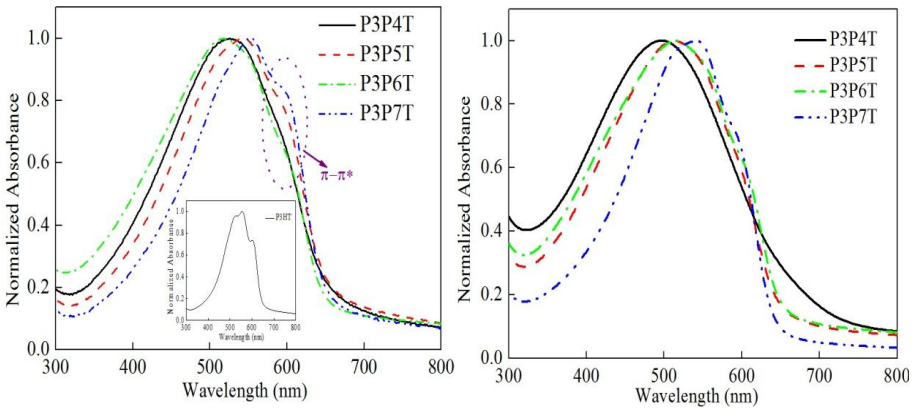

Figure 5.4: (a) UV-Vis absorption spectra of spin coated (~ 50 - 70 nm) pure P3P*m*Ts layers and P3HT layer (inset), (b) UV-Vis absorption spectra of new processing method deposition (~ 100 - 120 nm) pure P3P*m*Ts layers.

5.3.3 Cyclic voltammetry

The electrochemical properties of P3PmTs were studied using cyclic voltammetry as discussed in the section 2.3.4. Irreversible oxidation and reduction processes were observed on thin films as shown in **Figure 5.5**. Especially the oxidation process is completely irreversible during the first potential scan. Upon repeated scanning, the currents associated with the oxidation significantly get reduced. Onset potentials of the oxidation (first oxidation scan) and reduction (third reduction scan) were utilized to estimate the position of the highest occupied molecular orbital (HOMO) and the lowest unoccupied molecular orbital (LUMO) energy levels. The variations in the oxidation and reduction peaks were due to the thin film drop casting. From these measurements it is evident that the energy levels of P3P*m*Ts are in the same order of magnitude as those found for poly(3-hexylthiophene) (P3HT). The resulting electrochemical band gaps (E_g^{EC}) of these polymers were all in the range of 2.15 eV - 2.33 eV, which were slightly greater than the optical band gaps (E_g^{OP}) of 1.9 eV determined from the absorption spectra onset potentials. This is not unexpected, since electrochemically determined onsets of oxidation and reduction peaks measured show some level of ± 0.4eV errors. This is due to the occurrence of irreversible electrochemical processes and a small over-potential was required to allow the electrolyte ion to migrate through the polymer film during oxidation and reduction. Therefore, the cyclic voltammetry measurements confirm the very similar band gap values for all P3P*m*Ts and P3HT. CV estimated onset potentials; HOMO–LUMO and band gap values are summarized in **Table 5.2**.

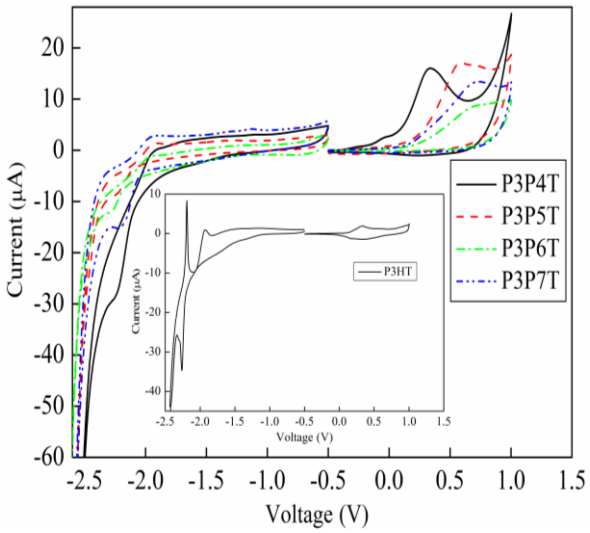

Figure 5.5: The cyclic voltammograms of the casted P3PmTs films and inset P3HT thin film.

Table 5.2: From CV estimated onset potentials, HOMO–LUMO and band gap values.

Polymer	E^{OX}_{onset} (V)	E^{RED}_{onset} (V)	HOMO (eV)	LUMO (eV)	E^{EC}_{g} (eV) (film) ±0.4 eV	E^{OP}_{g} (eV) (film)
P3P4T	0.09	−2.06	−5.02	−2.87	2.15	1.91
P3P5T	0.27	−2.06	−5.20	−2.87	2.33	1.91
P3P6T	0.24	−2.08	−5.17	−2.85	2.32	1.92
P3P7T	0.22	−2.06	−5.15	−2.87	2.28	1.92
P3HT	0.13	−2.20	−5.06	−2.73	2.33	1.92

5.3.4 Field effect transistor measurements (FET)

The FET IV-transfer characteristics of P3PmTs with fits are shown in **Figure 5.6**. With equation 2.13 the fits were made to estimate the hole mobility in P3PmTs. The FET hole mobilities are presented in **Table 5.3**. Differences in FET IV-transfer characteristics might be attributed to the orientation of P3PmT layers with respect to the SiO_2 substrate. This type of behavior is previously observed in poly(3-alkylthiophene) transistors.[21]

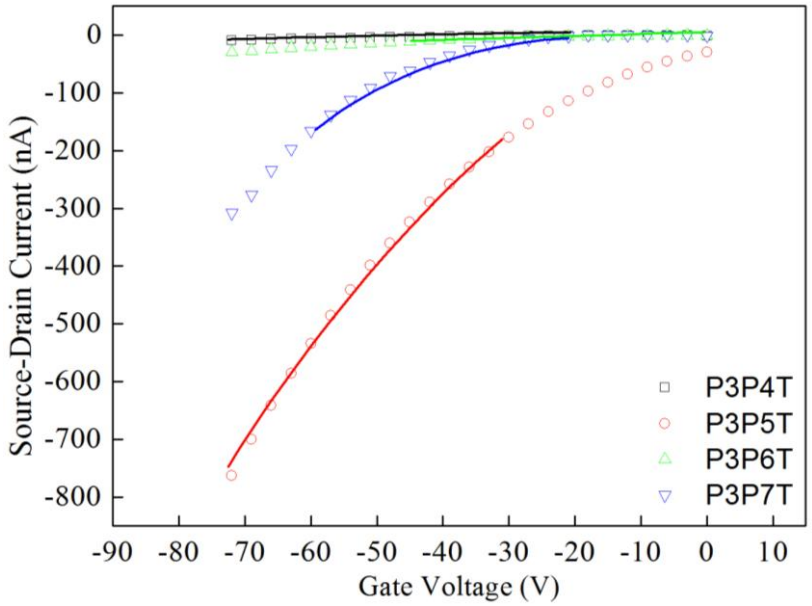

Figure 5.6: FET IV-transfer characteristics of P3PmTs with fits (solid lines) for obtaining the hole mobility.

5.3.5 Dielectric permittivity measurements

The measured dielectric permittivity (ε_r) of P3PmTs is determined by using equation 2.16. Linear fits were according to this equation and are shown in **Figure 5.7**. The ε_r of different P3PmTs obtained were in between 2.9 – 3.4.

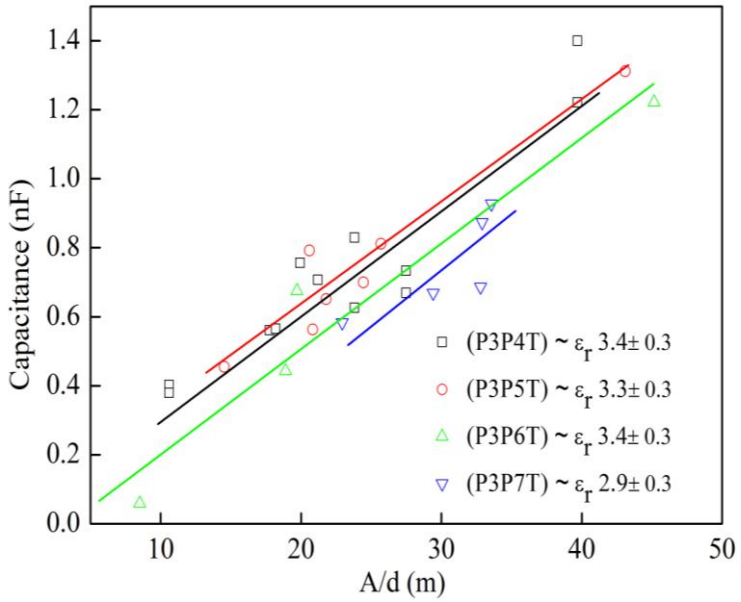

Figure 5.7: The dielectric constant of P3PmTs obtained by using linear fits according equation 2.16. Solid lines represent the fit.

5.3.6 Space charge limited current measurements (SCLC)

The charge transport properties play a major role in the device performances.[47] Techniques for studying the charge transport properties are SCLC modeling and FET characterizations.

The SCLC regime from dark IV-curve (as discussed under section 2.3.7) allows to determine the hole mobility of the charge carriers by using the Mott–Gurney equation 2.17. For studying the hole mobilities, hole – only diodes were prepared.

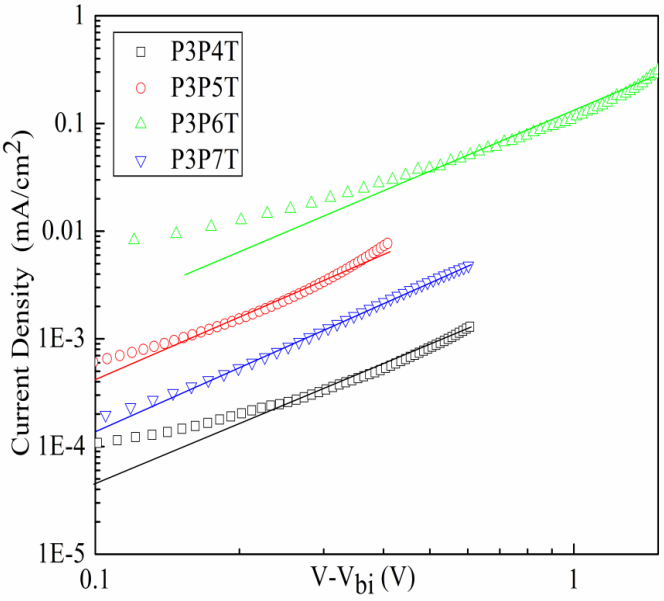

Figure 5.8: The log – log plot of current density (J) – voltage (V) characteristics of hole–only diodes of P3P*m*Ts. Solid lines represent the linear fits used for obtaining the hole mobilities of these P3P*m*Ts.

In these measurements transition points are very close to zero and obtained built in voltages (V_{bi}) values were very small (0.001V – 0.1V). **Figure 5.8** represents the experimental data of current densities J (mA/cm^2) for different P3PmTs plotted against the voltage (V). The obtained ε_r were used to estimate the hole mobilities. The estimated hole mobilities of P3PmTs by SCLC are summarized in **Table 5.3**.

Table 5.3: Measured SCLC and FET hole mobilities of P3PmTs, together with the thicknesses of the polymer film. The P3PmTs layers were deposited by using the new processing method (spin coating +spray coating).

Polymer	FET-Hole mobility (cm^2/Vs)	SCLC-Hole mobility (cm^2/Vs)	Hole only diodes Film thickness (nm)
P3P4T	$4\pm2 \times 10^{-7}$	$7.3\pm0.7 \times 10^{-8}$	195±60
P3PBT*		5.1×10^{-8}	–
P3P5T	$1.5\pm0.7 \times 10^{-5}$	$4.5\pm0.5 \times 10^{-7}$	165±30
P3P6T	$5\pm2 \times 10^{-7}$	$5.5\pm0.6 \times 10^{-6}$	240±50
P3P7T	$6\pm3 \times 10^{-5}$	$3\pm0.3 \times 10^{-7}$	190±50
P3HT#	8×10^{-3}	$5.6 \pm0.70 \times 10^{-4}$	–

*Ref.[22] (P3PBT – poly [3–(potassium–4–butanoate) thiophene–2, 5–diyl])
#Ref.[20]

For evaluating the bulk conductivity of the materials to be used in solar cells, SCLC is a more relevant method in comparison with FET measurements. The major advantage of the SCLC measurements is the sandwich structure between two electrodes, where the charge carriers move in perpendicular direction to the substrate, whereas in FET measurements the charge carriers are transported in the horizontal direction. This SCLC geometry is close to the geometry of a working solar cell. Moreover, the transport properties of charge carriers are well described by the SCLC modeling measurements. The highest hole mobility was found in P3P6T, which is 10 - 70 times higher than in other P3PmTs, but remains 100 times smaller than P3HT.

5.3.7 Morphology measurements of P3PmTs

The absorption spectra of P3PmTs (**Figure 5.2**) were already on indication for the lower crystallinity of P3PmTs. This is further confirmed by transmission electron microscope (TEM) and X-ray diffraction (XRD) measurements on P3P6T (high hole mobility polymer). Due to the use of water as solvent in the P3P6T layer, the preparation of the TEM samples was

difficult and tedious. A thin layer of P3P6T was drop casted above Cu grids and dried. For comparison, P3HT solution was also drop casted. The TEM images and XRD spectra are shown in **Figure 5.9**. It is clearly evident from the TEM-diffraction rings pattern in **Figure 5.9a** generated by the P3HT polymer crystallinity, while the TEM image of P3P6T depicts lower ordered (amorphous) material structure. In the TEM image of P3HT **Figure 5.9a**, a fiber network is visible, which was completely absent in the TEM-micrograph of P3P6T **Figure 5.9b**. From the XRD measurements **Figure 5.9c** P3HT shows a diffraction peak at $2\theta = 5.4$ (d-spacing of 1.6 nm), whereas P3P6T did not show any diffraction peaks by XRD or TEM measurements essentially indicating that the P3P6T layer is amorphous. This amorphous structure in P3P6T is possibly due to the presence of bulky alkanoate side chain groups. The same is explained with poor molecular ordering of bulky side chain groups substituted to P3HT.[23] These differences in morphology can justify the obtained low hole mobility for P3P6T and for other P3P*m*Ts in comparison with P3HT.

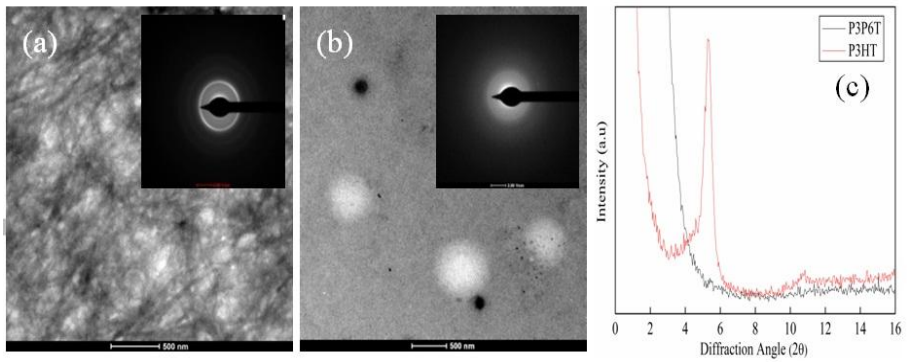

Figure 5.9: The TEM images with the corresponding selected - area electron diffraction patterns of casted solid films from (a) P3HT, (b) P3P6T (amorphous) scale bars are 500 nm and (c) XRD measurements on spin coated thin films of P3P6T and P3HT on Si substrates.

5.3.8 UV-Vis absorption measurements of P3P6T/TiO_2

Prior to the study of photovoltaic properties, the interaction between the polymer P3P6T and mesoporous TiO_2 layers was analyzed by using UV-Vis spectroscopy. A blue shift (~ 60 nm) in the absorption was observed as shown in **Figure 5.10** for P3P6T on a mesoporous TiO_2 layer, when

compared to a pure P3P6T layer on glass. This can be an indication that the side chains interact with the TiO_2 layer. According to Coakley et al.,[24] in such conditions the polymer chains are sterically hindered or twisted, and with this phenomenon, free movement/infiltration of the polymer into the mesoporous TiO_2 layers can be hampered. From **Figure 5.10** the low sharpness peak at 620 nm (lower crystalline) in pure P3P6T material disappears after spin coating above the TiO_2 layer which represents the interaction between the P3P6T and TiO_2 layer.

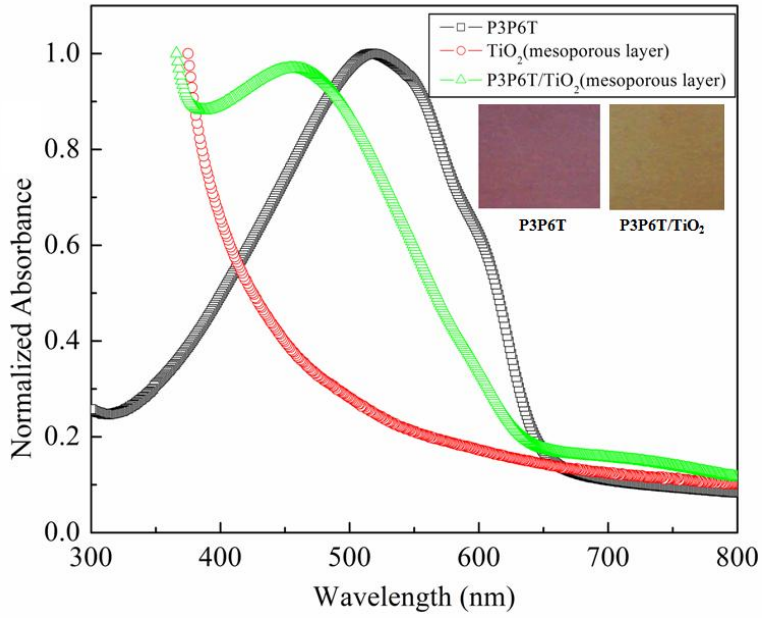

Figure 5.10: Normalized absorption spectra of films P3P6T (square), TiO_2 mesoporous layer (circle) and P3P6T/TiO_2 mesoporous layer (triangle) deposited on the glass substrates. The inset shows the color of the pure P3P6T layer (purple-red) and the P3P6T/TiO_2 layer (orange).

5.3.9 Morphology measurements on P3P6T/TiO_2

In order to increase the light absorbing capability by increasing the surface area, three-dimensional mesoporous TiO_2 films of 800 nm thicknesses were

prepared. In normal DSSCs, 20 nm grain sized TiO_2 layers are used. In the hybrid solar cells, created excitons have a diffusion length around 10 nm[25]. Therefore, the initial test was started on 13 nm grain sized nanoparticle layers, where the efficiency and device performance was low 0.21 % (**Table 5.4**). Later, the investigations were performed with 20 nm and 37 nm grain sized nanoparticle TiO_2 layers along with P3P6T. The SEM images of different grain sized TiO_2 layers are shown in **Figure 5.11**. The 37 nm grain sized titania layer was more porous compared to 13 nm and 20 nm grain sized TiO_2 layers. It was expected that polymer can better infiltrate into the pores of 37 nm grain sized TiO_2 layer.

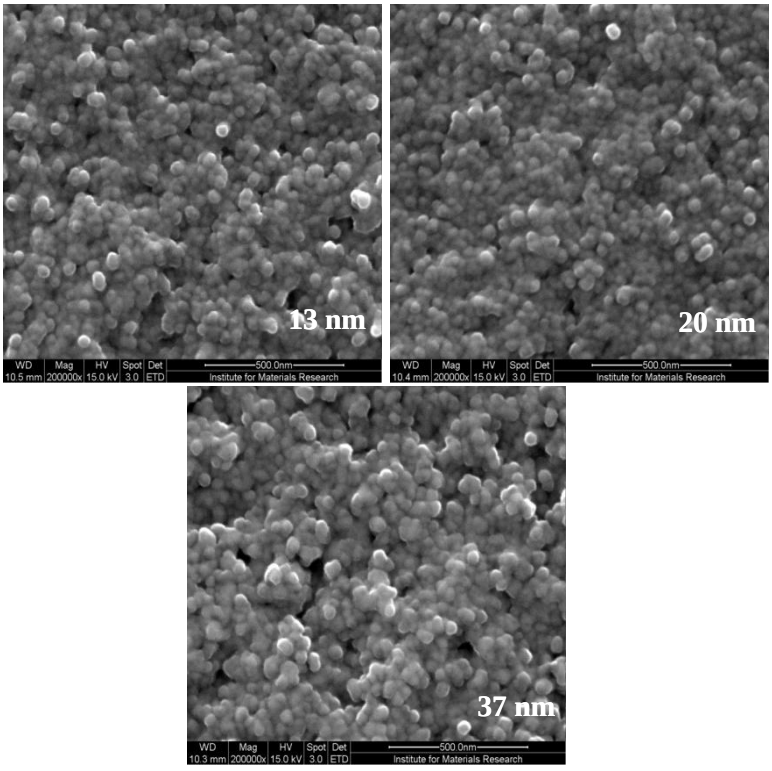

Figure 5.11: SEM images of spin coated different grain sizes nanoparticle TiO_2 layers (scale bar 500 nm).

From TEM image investigations on a P3P6T/TiO_2 (37 nm) sample, a bilayered structure was obtained and depicted in **Figure 5.12**. As already discussed for the UV-Vis absorption spectrum of P3P6T onto a mesoporous TiO_2 layer and now confirmed by TEM, the polymer infiltration into the porous TiO_2

layer is ~ 40 nm (where the thickness of TiO_2 layer is ~ 800 nm), which is incomplete. From the diffraction pattern of the polymer layer, crystalline structured rings were observed which do not correspond to the crystallinity of the very thin polymer layer, but to the dimensions of diaphragm used (Φ 290 nm).

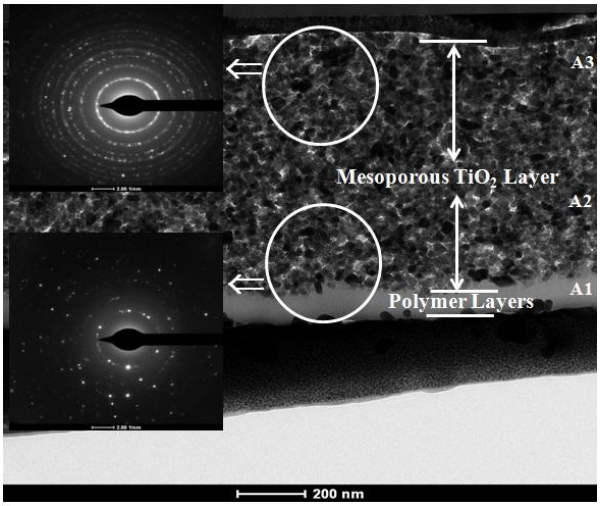

Figure 5.12: The TEM image of the bilayer device formed between P3P6T/TiO_2 layers, with the corresponding selected-area electron diffraction patterns. Polymer layer was deposited by the new processing method (spin + spray) coatings.

In addition to this cross-sectional TEM image, the sample was used to examine the chemical contribution of P3P6T polymer present in the mesoporous TiO_2 layer by energy-dispersive X-ray (EDX explained in section 2.4.1) measurements. The EDX spectra were recorded at three different regions as shown in **Figure 5.13** (A1 - polymer layer, A2 - middle of the TiO_2 layer and A3 - at the bottom of the TiO_2 layer) of the cross-section film by means of TEM, equipped with an EDX system and showed in **Figure 5.13**. In region A1, the presence of sulphur and potassium originating from P3P6T polymer was clearly observed. In regions A2 and A3, there is presence of potassium in the mesoporous layer. The other elements visible in the EDX spectra are from materials used for the sample preparation. The contribution of potassium in A2 and A3 regions can be explained in two different ways: 1) The potassium ions present in the P3P6T side chain are weakly bounded. Due to this, after deposition of the P3P6T layer, the potassium ions migrate into the TiO_2 mesoporous layer this is observed from EDX spectra. 2) The X-rays are emitted in the focused direction. They may

escape from the path resulting in out of focus covering large areas of the complete sample (P3P6T/TiO_2) measuring the potassium signal.

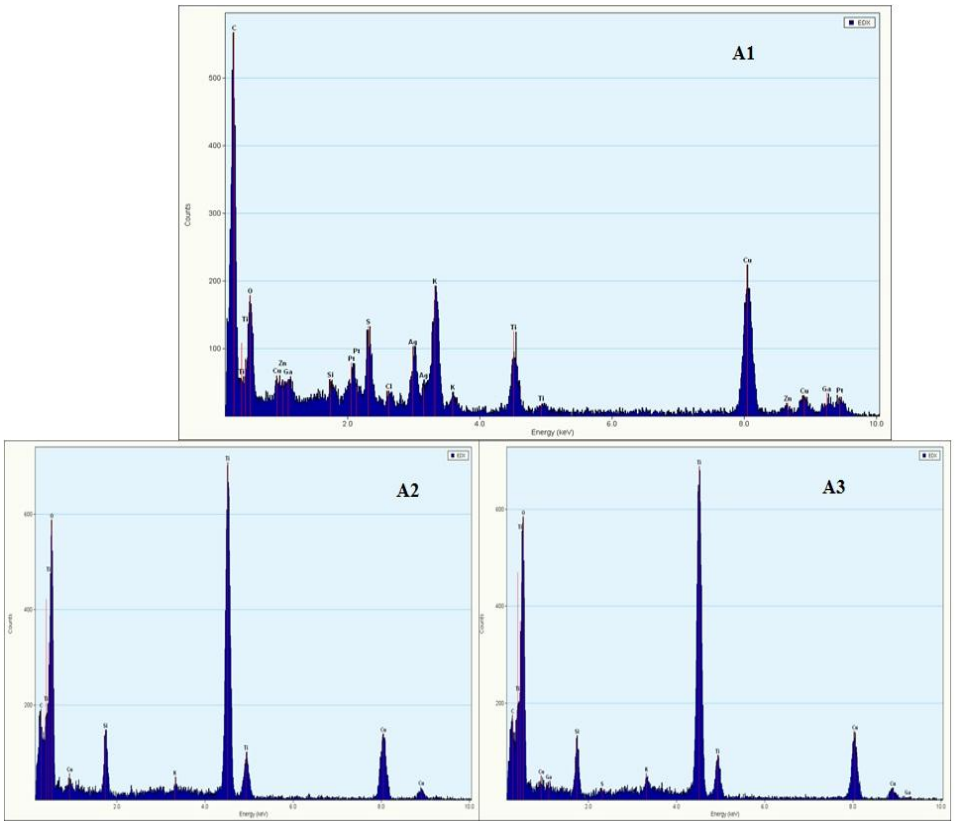

Figure 5.13: EDX spectra at three different regions in bilayer device formed between P3P6T/TiO_2 layers (A1 - polymer layer, A2 - middle of the TiO_2 layer and A3 - at the bottom of the TiO_2 layer).

5.3.10 IV-measurements

The photovoltaic characteristics of bilayered P3P6T/TiO_2 devices were measured in N_2 and in ambient environment conditions are shown in **Figure 5.14**. The light IV-characteristics under N_2 and under ambient conditions are summarized in **Table 5.4**. In N_2 conditions, the IV-curves develop ohmic behavior during measurements.[26-29] This behavior is attributed to the vacant oxygen formation, by release of oxygen from TiO_2 during measurements. Higher amounts of oxygen vacancies can be formed depending upon the phase of TiO_2. Since oxygen vacancies are well known for electron traps, as

a result, higher amount of recombination can be expected at these centers. At the same time, the TiO_2 electrode becomes highly conductive and the charge carrier density increases by the reduction of series and shunt resistance which affects the photovoltaic properties.[26-29] Subsequently, if the samples are re-exposed and measured in air, the trapped electrons in the oxygen vacancies can scavenge by ambient oxygen in TiO_2 layers, resulting in improvement of the device performance. This is well explained elsewhere.[26-29]

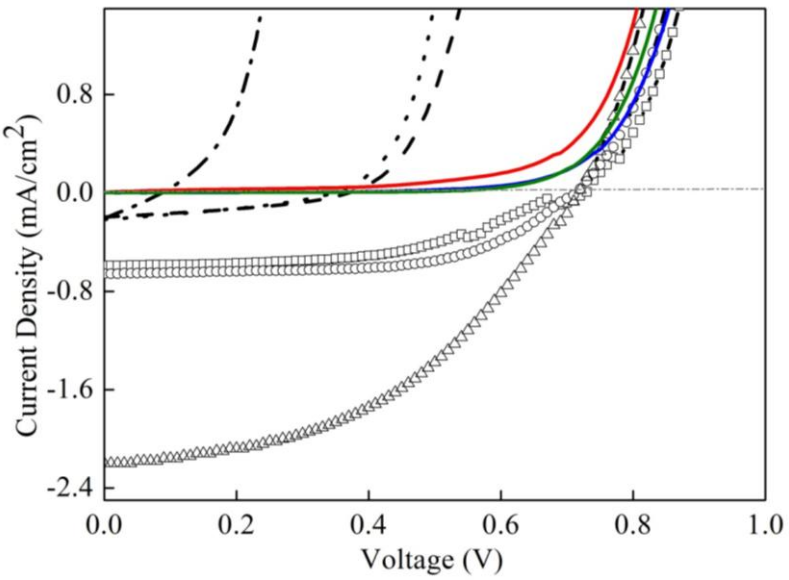

Figure 5.14: Light IV-measurements of P3P6T/TiO_2 -13 nm (**N_2**: dash, **O_2**: square), P3P6T/TiO_2 -20 nm(**N_2**: dot, **O_2**: circle) and P3P6T/TiO_2 -37 nm (**N_2**: dash dot, **O_2**: triangle) where **N_2** measurements were performed in glove box and **O_2** measurements were performed in air. Dark IV measurements -under ambient conditions of P3P6T/TiO_2 -13 nm (red), P3P6T/TiO2 -20 nm (green) and P3P6T/TiO_2 -37 nm (blue).

The devices based on P3P6T/TiO_2 -13 nm and P3P6T/TiO_2 -20 nm showed similar devices performance, whereas P3P6T/TiO_2 -37 nm device showed a significant increase in the device performance. It is expected that, if larger grain sized particle layers were used then the infiltration of the polymer into these layers is more significant. However, in this case from the TEM cross-sectional image the polymer infiltration is incomplete in all the devices. The increase in photocurrent with 37 nm compared to 13 nm and 20 nm is due to the interface surface area of the pores that has an influence over exciton

diffusion (10 nm). Therefore the best overall device performances can be obtained and compromised in between titania nanoparticles size of 13 nm to 37 nm layers. This type of pore size effect is observed in hybrid solar cells prepared from spiro-OMeTAD incorporation with PbS quatum dot-sensitized TiO_2 layers and P3HT deposition on to TT1 dye sensitized TiO_2 layers.[30, 31]

Table 5.4: Summarized set of data for J_{sc} (mA/cm^2), V_{oc} (V), FF (%) and η (%) for different solar cells prepared from P3P6T/TiO_2 (13 nm), P3P6T/TiO_2 (20 nm) and P3P6T/TiO_2 (37 nm). Last two rows are data from Refs[6, 7] and shown for the comparison.

TiO_2 nanoparticles size (nm)	Measuring Medium	Polymer	J_{sc}	V_{oc}	FF	η	Ref
13	O_2	P3P6T	0.6	0.7	50	0.21	This work
20	O_2	P3P6T	0.65	0.7	60	0.28	This work
37	O_2	P3P6T	2.21	0.7	45	0.7	This work
13	N_2	P3P6T	0.3	0.17	38	0.02	This work
20	N_2	P3P6T	0.27	0.35	22	0.03	This work
37	N_2	P3P6T	0.21	0.13	34	0.008	This work
13	NA	P3SHT	1	0.43	33	0.14	6
30	NA	PTEBS	0.35	0.8	40	0.13	7

5.4 Conclusions

Opto-electrical properties of water soluble P3P*m*Ts have been presented and discussed. Using P3P6T polymer as hole transporting layer and an alternative new processing method (spin coating + spray coating) followed by petri dish drying after each step of processing, the power conversion efficiency obtained for these eco-friendly HSC is greater than the literature reported efficiencies with water soluble conjugated polymers[6, 7]. This promising result opens a new path way and stands as a proof-of-principle for making eco-friendly HSCs by replacing dye and liquid electrolyte. From the dark IV-measurements in the bilayer P3P6T/TiO_2 device the hole mobility has been determined to be in the order of 10^{-6} cm^2/Vs. The electron mobility of the porous TiO_2 layer is in the order of 10^{-6} to 10^{-7} cm^2/Vs discussed elsewhere [32, 33]. It is important to note that these mobility values are three orders of magnitude smaller than the ones found in polymer: fullerene solar cells. The intrinsic hole mobility of the polymer is not influenced by infiltration depth, but influences the hole-transfer yield.[34] The further improvement in the device performance can be anticipated if morphology of the eco-friendly processable conjugated polymers is better tuned with an increase of crystallinity. Future work is on going towards a detailed study of interface properties and better control of the metal oxide: polymer interface morphology, in order to obtain completely infiltrated polymer for three dimensional heterojunctions instead of bilayers. Also the use of novel generation polar materials might enhance the device performances. In this context of eco-friendly solar cells it is important to cite that initial life cycle analysis studies[35, 36] have shown that organic photovoltaics (OPV) have a promising potential. But more research is needed to establish a completely green production process for OPV in which finally they do not harm the environment during their preparation.

5.5 References

1. B. S. Gaylord, A. J. Heeger, G. C. Bazan, J. Am. Chem. Soc. 125 (2003) 896.
2. D. T. McQuade, A. E. Pullen, T. M. Swager. Chem. Rev. 100 (2000) 2537.
3. C. V. Hoven, A. Garcia, G. C. Bazan, T-Q. Nguyen, Adv. Mater. 20 (2008) 3793.
4. W. L. Ma, P. K. Iyer, X. Gong, B. Liu, D. Moses, G. C. Bazan, A. J. Heeger, Adv. Mater. 17 (2005) 274.
5. C. H. W. Cheng, S. W. Boettcher, D. H. Johnston, M. C. Lonergan, J. Am. Chem. Soc. 126 (2004) 8666.
6. I. Haeldermans, I. Truijen, K. Vandewal, W. Moons, M. K. Van Bael, J. D'Haen, J. V. Manca, J. Mullens, Mater. Res. Soc. Symp. Proc. 1013 (2007) 05.
7. Q. Qiao, J. T. McLeskey, Appl. Phys. Lett. 86 (2005) 153501.
8. C. Y. Tan, M. R. Pinto, M. E. Kose, I. Ghiviriga, K. S. Schanze, Adv. Mater. 16 (2004) 1208.
9. A. Khan, S. Müller, S. Hecht, Chem. Commun. (2005) 584.
10. J. Yang, A. Garcia, T-Q. Nguyen, Appl. Phys. Lett. 90 (2007) 103514.
11. R. Søndergaard, M. Helgesen, M. Jørgensen, F. C. Krebs, Adv. Energy. Mater. 1 (2011) 68.
12. T. R. Andersen, T. T. Larsen-Olsen, B. Andreasen, A. P. L. Böttiger, J. E. Carlé, M. Helgesen, E. Bundgaard, K. Norrman, J. W. Andreasen, M. Jørgensen, F. C. Krebs, ACS NANO. 5 (2011) 4188.
13. G. Li, V. Shrotriya, J. Huang, Y. Yao, T. Moriarty, K. Emery, Y. Yang, Nat. Mater. 4 (2005) 864.
14. A. M. Peiró, P. Ravirajan, K.Govender, D. S. Boyle, P. O' Brien, D. D. C. Bradley, J. Nelson, J. R. Durrant, J. Mater. Chem. 16 (2006) 2088.
15. Q. Fan, B. McQuillin, D. D. C. Bradley, S. Whitelegg, A. B. Seddon, Chem. Phys. Lett. 347 (2001) 325.
16. W. Lee, R. S. Mane, S. K. Min, T. H. Yoon, S. H. Han, S. H. Lee, Appl. Phys. Lett. 90 (2007) 263503.
17. I. Haeldermans, I. Truijen, K. Vandewal, W. Moons, M. K. Van Bael, J. D'Haen, J. V. Manca, J. Mullens, Thin Solid Films. 516 (2008) 7245.
18. W. D. Oosterbaan, V. Vrindts, S. Berson, S. Guillerez, O. Douheret, B. Ruttens, J. D'Haen, P. Adriaensens, J. Manca, L. Lutsen, D. Vanderzande, J. Mater. Chem. 19 (2009) 5424.

19. W. D. Oosterbaan, J. C. Bolsée, A. Gadisa, V. Vrindts, S .Bertho, J. D'Haen, T.J. Cleij, L.Lutsen, C. R. McNeill, L.Thomsen, J. V. Manca, D. Vanderzande, Adv. Funct. Mater. 20 (2010) 792.
20. A. Gadisa, W. D. Oosterbaan, K. Vandewal, J. C. Bolsée, S. Bertho, J. D'Haen, L. Lutsen, D. Vanderzande, J. V. Manca, Adv. Funct. Mater. 19 (2009) 3300.
21. Y. D. Park, D. H. Kim, Y. Jang, J. H. Cho, M. Hwang, H. S. Lee, J. A. Lim, K. Cho, Org. Electron. 7 (2006) 514.
22. A. Garcia, T-Q. Nguyen, J. Phys. Chem. C. 112 (2008) 7054.
23. Z.Bao, A. J. Lovinger, Chem. Mater. 11 (1999) 2607.
24. K.M. Coakley, M. D. McGehee, Chem. Mater. 16 (2004) 4533.
25. A. C. Arango, L. R. Johnson, V. N. Bliznyuk, Z. Schlesinger, S. A. Carter, H. H. Horhold, Adv. Mater. 12 (2000) 1689.
26. M. Lira-Cantu, A. Chafiq, J. Faissat, I. Gonzalez-Valls, Y. Yu, Sol. Energy Mater Sol. Cells. 95 (2011) 1362.
27. B. V. D. Zandena, A. Goossens, J. Appl. Phys. 94 (2003) 6959.
28. H. Al-Dmour, D. M. Taylor, Appl. Phys. Lett. 94 (2009) 223309.
29. A. Watanabe, A. Kasuya, Thin Solid Films. 483 (2005) 358.
30. H. J. Lee, C. L. Henry, S. Haque, T. Torres, M. Grätzel, M.K. Nazeeruddin, J. Pow. Sour. 196 (2011) 596.
31. H. J. Lee, H. C. Leventis, S.-J. Moon, P. Chen, S. Ito, S. A. Haque, T. Torres, F. Nüesch, T. Geiger, S. M. Zakeeruddin, M. Grätzel, M. K. Nazeeruddin, Adv. Funct. Mater. 19 (2009) 2735.
32. P. Ravirajan, S. A. Haque, J. R. Durrant, D. D. C. Bradley, J. Nelson, Adv. Funct. Mater.15 (2005) 609.
33. B. O. Aduda, P. Ravirajan, K. L. Choy, J. Nelson, Int. J. Photoenergy 6 (2004) 141.
34. J. E. Kroeze, N. Hirata, L. Schmidt Mende, C. Orizu, S. D. Ogier, K. Carr, M. Grätzel, J. R. Durrant, Adv. Funct. Mater.16 (2006)1832.
35. N. Espinosa, R. García-Valverde, F. C. Krebs, Energy Environ. Sci. 4 (2011) 1547.
36. N. Espinosa, R. García-Valverde, A. Urbina, F. C. Krebs, Sol. Energy Mater. Sol. Cells. 95 (2011) 1293.

Chapter 6: Conclusions and Outlook

6.1 Conclusions

The sunlight reaching the earth has an enormous potential for the energy production. The photovoltaic industry is one of the best options for the production of electric energy. Inspite of reducing the production costs, alternative new solar cells have to maintain the stability and efficiency as of silicon based solar cells. To realize this, it is necessary to understand and improve the current limiting factors of the polymer based organic:inorganic hybrid solar cells. The preparation and characterization of novel and eco-friendly hybrid solar cells is considered as a key issue and therefore the primary goal of this thesis.

The performance of the hybrid solar cells is still low, when compared to the complete organic BHJ solar cells as reported in chapter 1. However, steady progress in device performances has been thoroughly growing by understanding the limitations. In particular chapter 3, P3HT based HSC devices are prepared with and wihtout dyes. The highest efficiency of 1.3% under AM1.5 radiation obtained with C101 dye treated device. With the help of different opto-electrical charterization technqiues like FTPS, CELIV, TPC and TPV the charge seperation and charge transport properties are measured. From these characterizations the limiting factors of the HSC device performances are understood.

The assembly of CuPc based hybrid solar cells are demonstrated in chapter 4. The CuPc layer is vacuum sublimated above without and with dye sensitized TiO_2 layers. With the help of wide variety of opto-electrical characterizations the charge transport and separation properties are well explained. These experiments confirm that the CuPc acts as a hole transporting material in this type of HSCs.

In the preparation of eco-friendly hybrid solar cells (chapter 5), opto-electrical properties of different water soluble P3P*m*Ts have been presented and discussed. Using P3P6T polymer as a hole transporting layer the power conversion efficiency obtained for eco-friendly HSCs is 0.7%. This promising result opens a new path way and stands as a proof-of-principle for making eco-friendly HSCs by replacing dye and liquid electrolyte.

6.2 Outlook

During the preparation of HSCs it was difficult to obtain the complete infiltration of semiconducting polymers (P3HT, CuPc and water soluble P3P*m*Ts) into the mesoporous layers. Poly(isothianaphthene) (PITN) offers a new route for complete pore filling metal-oxide layer by polymer. PITN is an oligomer precursor. As a proof-of-concept this is shortly briefed under this section.

The discovery of Poly(isothianaphthene) (PITN) in 1984 by Heeger et al.[1] has received great attention due to its low band gap (1 -1.4 eV)[2-5] and high conductivity[6]. The PITN oligomer (orange colour) has a poor stability but, after polymerization (blue black colour) it is stable for longer time.[7] PITN with different side chains also received great interest in solar cell applications as p-type material.[8-14] The bulk heterojunction device prepared from PITN/C_{60} showed very low device performance.[15] Electron paramagnetic resonance studies of PITN are also reported in order to understand the charge transfer properties.[16]

PITN oligomer was synthesized and supplied from the organic chemistry department (UHasselt)[7] and the chemical structure is shown in **Figure 6.1**.

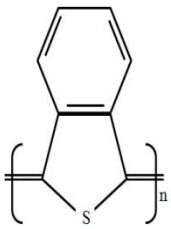

Figure 6.1: Chemical structure of PITN.

The absorption spectra of in-situ polymerization heating/cooling process between the glass discs are shown in **Figure 6.2**. The PITN oligomer polymerizes forming a blue-black layer in the between 110 ^{0}C to 170 ^{0}C. The sample was cooled down from 170 ^{0}C to 40 ^{0}C and an absorption spectrum was recorded at 40 ^{0}C. The PITN polymer has a band gap of 1.1 eV from the absorption window onset with an absorption peak value at 655 nm. The temperature needed for the PITN polymerization was 160 ^{0}C.

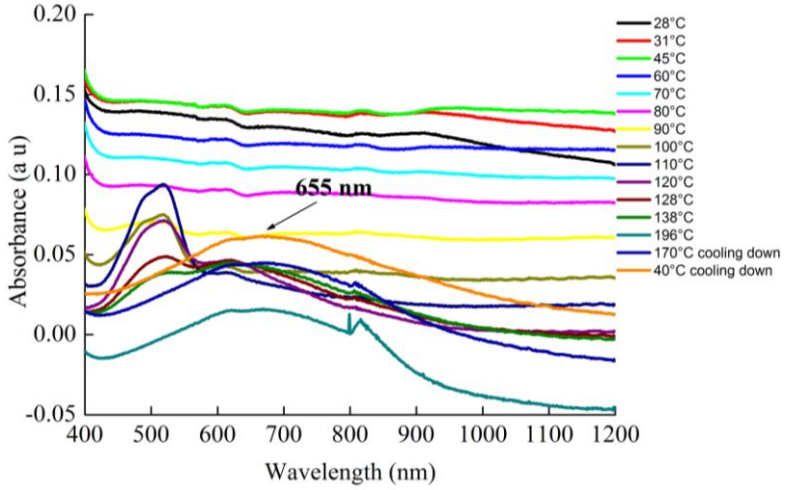

Figure 6.2: Absorption spectra recorded during in-situ polymerization of PITN between two glass discs.

Electrochemical measurements were performed to estimate the HOMO and LUMO levels of polymerized PITN as discussed in chapter 2.3.4. PITN was drop casted and polymerized at 170 ^{0}C on ITO electrodes in ambient conditions. The cyclic voltammogram of a PITN thin film displayed oxidation and reduction processes as depicted in **Figure 6.3**. The corresponding energy levels of PITN polymer are shown in **Table 6.1**. Energetically PITN polymer can be incorporated with ZnO or TiO_2 mesoporous layers.

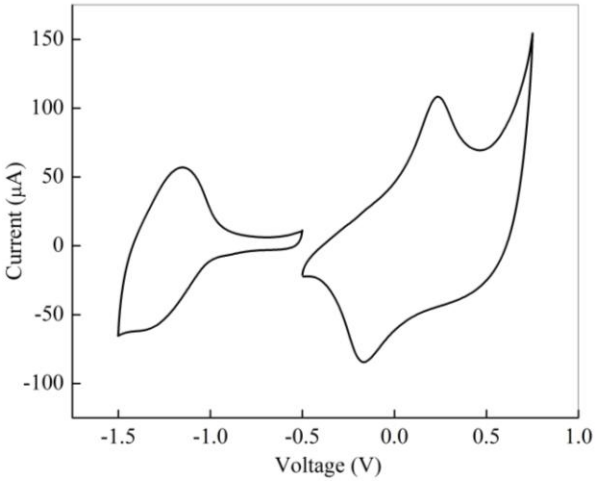

Figure 6.3: Cyclic voltammogram of PITN.

Table 6.1: Electrochemical band gap HOMO and LUMO levels of PITN.

Material	E^{OX}_{onset} (V)	E^{RED}_{onset} (V)	HOMO (eV)	LUMO (eV)	E^{EC}_{g} (eV) (film)	E^{OP}_{g} (eV) (film)
PITN	-0.01	-1.06	-4.92	-3.87	1.05	1.07

A chemical bath deposition technique for the polymerization of a PITN layer[7] into 300 nm ZnO nanorods was successfully performed. The ZnO nanorods were grown on glass substrates at the inorganic chemistry department (UHasselt).[17] The SEM was used as a tool to investigate the quantity of polymerization of PITN in the ZnO nanorods. The SEM images are shown in **Figures 6.3 a** and **b**. With this technique a clear observation can be made for infiltration of PITN polymer into the nanorods. From **Figure 6.3a**, a composition of PITN with ZnO nanorods can be observed. The broken ZnO nanorods were formed during the SEM sample preparation as observed through the SEM. From the topographic image of **Figures 6.3b**, PITN polymerized layer was shown to be homogeneous in the nanorods.

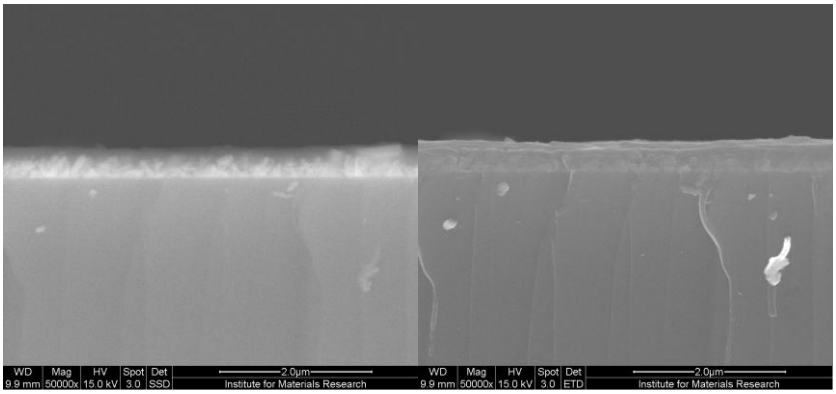

a b

Figure 6.3: SEM images of PITN with ZnO nanorods; (a) composition and (b) topography.

The absorption spectra of polymerized PITN above glass and ZnO nanorods are shown in **Figures 6.4**. From these spectra the PITN on glass and nanorods showed a peak value at 660 nm with a broad absorption window. This is comparable with the absorption results obtained during in-situ polymerization.

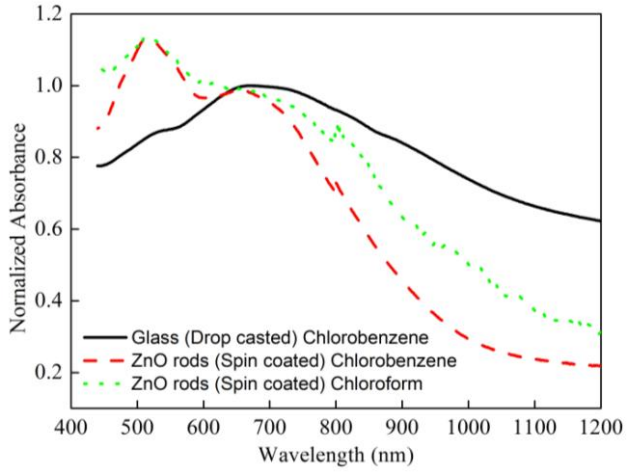

Figure 6.4: The absorption spectra of PITN above glass and 300 nm ZnO nanorods.

The PITN polymerizes in the mesoporous TiO_2 layers. From the top and cross sectional views of SEM images, it can be observed that the layers were filled with PITN as shown in **Figures 6.5 a** and **b**. The top view of SEM image shows the PITN polymer forms a thin layer and cross-sectional view shows the PITN is segregated into the mesoporous layer.

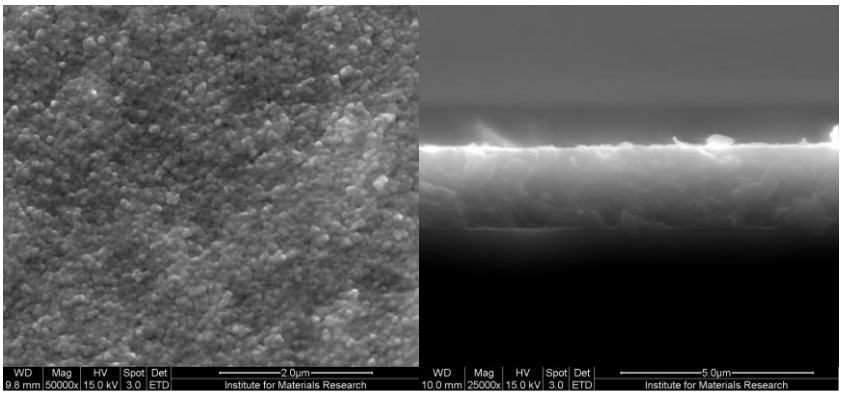

a b

Figure 6.5: SEM images of PITN/1.8 µm mesoporous TiO_2 thick layer using tetrahydrofuran as a solvent for PITN (a) top view and (b) cross sectional view.

This opens a new way for preparation and development of hybrid solar cells by PITN polymerization in the mesoporous layers.

6.3 References

1 F. Wudl, M. Kobayashi, A. J. Heeger, J. Org. Chem. 49 (1984) 3382.
2 I. Hoogmartens, P. Adriaensens, D. Vanderzande, J. Gelan, C. Quattrocchi, R. Lazzaroni, J. L. Brédas, Macromolecules 25 (1992) 7347.
3 I. Hoogmartens, P. Adriaensens, R. Carleer, D. Vanderzande, J. Gelan, H. Matrens, Synth. Met. 51 (1992) 219.
4 R. Kiebooms, I. Hoogmartens, P. Adriaensens, D. Vanderzande, J. Gelan, Macromolecules 28 (1995) 4961.
5 G. Zerbi, M. C. Magnoni, I. Hoogmartens, R. Kiebooms, R. Carleer, D. Vanderzande, J. Gelan, Adv. Mater. 7 (1995) 1027.
6 N. Colaneri, M. Kobayashi, A. J. Heeger, F. Wudl, J. Chem. Phys. 82 (1985) 5717.
7 R. Van Asselt, D. Vanderzande, J. Gelan, P. E. Froehling, O. Aagaard, Synth. Met. 1 (2000) 25.
8 R. Kisselev, M. Thelakkat, Macromolecules. 37 (2004) 8951.
9 H. Paulussen, D. Vanderzande, J. Gelan, Synth. Met. 84 (1997) 415.
10 I. Polec, L. Goris, A. Henckens, M. Nicolas, M. Loi, L. Lutsen, J. Manca, D. Vanderzande, N. S. Sariciftci, J Polym Sci Part A: Polym Chem 41 (2003), 1034.
11 L. Goris, M. Loi, A. Cravino, H. Neugebauer, N. S. Sariciftci, L. Lutsen, J. Manca, L. De Scheppers, D. Vanderzande, Synth. Met. 138 (2003), 249.
12 M. Lapkowski, R. Kiebooms, J. Gelan, D. Vanderzande, A. Pron, T. P. Nguyen, G. Louarn, S. Lefrantm, J. Mater. Chem., 7 (1997) 873.
13 H. Meng, F. Wudl, Macromolecules 34 (2001) 1810.
14 C-Y. Lee, M. H-C. Jin, Proc. of SPIE Vol. 6656 (2007) 66560Y-1.
15 K. Tada, S. Morita, T. Kawai, M. Onoda, K. Yoshino, A. A. Zakhidov, Synth. Met. 70 (1995), 1347.
16 W-T. Chen, G. A. Bowmaker, R. P. Cooney, Phys. Chem. Chem. Phys. 4 (2002) 4218.
17 L. Baeten, B. Conings, H-G. Boyen, J. D'Haen, A. Hardy, M. D'Olieslaeger, J. V. Manca, M. K. Van Bael, Adv. Mater. 23 (2011) 2802.

PUBLICATIONS

1. **Gopala Krishna T.V.V**, Jean-Christophe Bolsée, Abay Gadisa, Mikhail Parchine, Tine Boonen, Jan D'Haen, Ayse E. Boyukbayram, Joke Vandenbergh, Thomas J. Cleij, Laurence Lutsen, Dirk Vanderzande, and Jean V. Manca. Opto-electrical and morphological characterization of water soluble conjugated polymers for eco-friendly hybrid solar cells, *Solar Energy Materials & Solar Cells 95 (2011) 3262–3268*.

2. **Gopala Krishna T.V.V**, John N. Clifford, Donato Spoltore, Fortunato Piersimoni, Emilio Palomares and Jean V. Manca. Optoelectrical and photophysical properties of solid-state dye sensitized solar cells using evaporated CuPc layers as hole transporting material, *Submitted*.

3. Vandenbergh. J, Dergent. J, Conings. B, **Gopala Krishna T.V.V**, Maes. W, Cleij, T. J, Lutsen. L, Manca. J and Vanderzande. D. J. M. Synthesis and characterization of water soluble poly(p-phenylene vinylene) derivatives via the dithiocarbamate precursor route. *European Polymer Journal 47 (2011) 1827–1835*.

4. **Gopala Krishna T.V.V**, John N. Clifford, Fortunato Piersimoni, Donato Spoltore, Emilio Palomares and Jean. V. Manca. Photocurrent response and transient current extraction investigations on three-dimensional organic/inorganic hybrid solar cells, *to be Submitted 2012*.

5. **Gopala Krishna** and Jean-Christophe Bolsée, VIEW FROM… 2010 MRS SPRING MEETING, *Nature Photonics, **4**, 351, 2010. Work Summary*.

CONFERENCES & MEETINGS

1 **Gopala Krishna T.V.V**, John N. Clifford, Donato Spoltore, Fortunato Piersimoni, Emilio Palomares and Jean V. Manca, 'Investigation of Interface Properties in Hybrid Solar Cells', Dutch Solar Energy R&D Seminar (Joint Solar Panel –Utrecht, Netherlands), 2011. **Poster**

2 **Gopala Krishna T.V.V**, John N. Clifford, Donato Spoltore, Fortunato Piersimoni, Emilio Palomares and Jean V. Manca, 'Opto-Electrical Properties of Copper Phthalocyanine (CuPc) Based Solid-State Grätzel Solar Cells' Belgian Physical Society (BPS, Namur), 2011. **Oral Talk**

3 **Gopala Krishna T.V.V**, John N. Clifford, Donato Spoltore, Fortunato Piersimoni, Emilio Palomares and Jean V. Manca, 'Investigation of Interface Properties of Copper Phthalocyanine/Dye/Titania Hybrid Solar Cells', EMRS spring Meeting (Nice, France), 2011. **Poster**

4 John N Clifford, **Gopala Krishna T.V.V**, Margherita Bolognesi, Jean Manca and Emilio Palomares, 'Modification of the TiO_2/polymer interface in nanocrystalline TiO_2/P3HT hybrid solar cells with thiophene containing molecular species: improved exciton splitting and cell efficiency', Advanced Materials and Nanotechnology (AMN-5, Newzealand), 2011. **Poster**

5 **Gopala Krishna T.V.V,** Jean-Christophe Bolsée, Abay Gadisa, Mikhail Parchine, Tine Boonen, Jan D'Haen, Ayse E. Boyukbayram, Joke Vandenbergh, Thomas J. Cleij, Laurence Lutsen, Dirk Vanderzande, and Jean V. Manca, 'Hybrid solar cells based on water soluble polymers: electro-optical properties and photovoltaic characterization', Dutch Solar Energy R&D Seminar (Joint Solar Panel –Utrecht, Netherlands), 2010. **Poster**

6 **Gopala Krishna**, Jean-Christophe Bolsée, Abay Gadisa, Mikhail Parchine, Jan D'Haen, Bert Conings and Jean V. Manca, ''Green' solid-state Grätzel solar cells: charge transport and photovoltaic properties', MRS Spring Meeting (San Francisco, USA), 2010. **Oral Talk**